Stress localization and size dependent toughening effects in SiC composites

A DISSERTATION
SUBMITTED TO THE FACULTY OF THE GRADUATE SCHOOL
OF THE UNIVERSITY OF MINNESOTA
BY

Aaron Ross Beaber

IN PARTIAL FULFILLMENT OF THE REQUIREMENTS
FOR THE DEGREE OF
DOCTOR OF PHILOSOPHY

William W. Gerberich, Steven L. Girshick

August 2010

© Aaron Ross Beaber 2010

Acknowledgments

First, I would like to thank my advisors, William Gerberich and Steven Girshick, for their guidance and support during my graduate career. Prof. Gerberich and Girshick formed an excellent coadvising team that helped shape my research project in ways that would not have been possible under the sole guidance of either. The funding for my project came from the National Science Foundation (CTS-0506748) and Air Force Office of Scientific Research (AOARD-08-4134) and thankfully coincided perfectly with my tenure as a graduate student.

I would also like to acknowledge a number of key research collaborators. These include: Dr. Bill Mook, currently at the Swiss Laboratories for Mechanics of Materials and Nanostructures (EMPA, Thun) for providing Si nanotower samples (batch A), hosting me for a brief visit to EMPA's labs in Aug 2009, and his collaborative efforts with the SEM *in situ* indentation experiments; Dr. Johann Michler, who is the head of research group at EMPA (Thun), for his insights and recommendation that I pursue confocal Raman measurements with the SiC-Si composite towers; Dr. Mikhael Bechalany (EMPA, Thun) for providing Au patterned Si substrates for the investigation of VLS grown Si using HPPD; Dr. Julia Deneen (Hysitron Inc.), for her expertise with TEM and collaborative efforts with the *in situ* indentation experiments. Julia was also a great liaison between Hysitron and UMN, helping to facilitate collaborations between the two groups; Dr. Ozan Ugurlu (Characterization Facility, UMN), for his expertise with TEM and collaborative efforts with the *in situ* indentation experiments; Dr. Albert Davydov and Dr. Sergei Krylyuk (NIST Metallurgy, Gaithersburg, MD) for providing Si nanotower samples (batch B).

A third group of important contributors is the UMN support staff, including ME machinists Robin Russell, Pat Nelson, Dave Hultman, Bob Nelson (who has since retired), and Peter Zimmermann and CEMS administrative assistants Julie Prince and Teresa Bredahl.

Finally, I would like to thank the graduate students in Prof. Gerberich and Girshick's research groups, particularly Doug Stauffer, Lejun Qi, and Adam Boies. Additionally, I would like to acknowledge alumni from these groups who were very helpful in my early graduate career. These include Dr. Bill Mook, Dr. Megan Cordill, Dr. Jami Hafiz, and Dr. Rajesh Mukherjee. Last, but not least, I would like to thank my friends and family for support and encouragement.

Dedication

I would like to dedicate this dissertation to my parents, Lawrence and Patricia Beaber, whose foremost commitment to education has been a constant inspiration.

Abstract

Coatings with high wear resistance have generated a great deal of interest due to a diverse range of applications, including cutting tools, turbine blades, and biomedical joint replacements. Ceramic nanocomposites offer a potential combination of high strength and toughness that is ideal for such environments. In the current dissertation research, silicon and silicon carbide based films and nanostructures were deposited using a hybrid of chemical vapor deposition and nanoparticle ballistic impaction known as hypersonic plasma particle deposition (HPPD). This included SiC/Ti-based multilayers and Si-SiC core-shell composite nanotowers. Using a combination of nanoindentation and confocal Raman microscopy, the role of plasticity and phase transformations was studied during fracture events at small length scales. In a parallel study, HPPD synthesized Si nanospheres and vapor-liquid-solid (VLS) Si nanotowers were compressed uniaxially inside the TEM. These experiments confirmed inverse length scale dependent relationships for strength and toughness in Si based on dislocation pile-up and crack tip shielding mechanisms, respectively. A transition was also identified in the deformation of Si under anisotropic loading below a critical size and used as the basis for a new toughening mechanism in Si-SiC composites. Overall, these results demonstrate the importance of nanoscale confinement and localized stress in the design of mechanically robust nanocomposites.

Table of Contents

Acknowledgments i

Dedication ii

Abstract iii

Table of Contents iv

List of Tables vii

List of Figures viii

Chapter 1 – Introduction and motivation **1**

1.1 Overview 1

1.2 Motivation 2

1.3 Materials development 4

Chapter 2 – Experimental **10**

2.1 Overview 10

2.2 Hypersonic plasma particle deposition (HPPD) . . . 10

2.3 SiC film deposition and growth mechanism 15

2.4 Post-deposition processing 24

2.5 Mechanical characterization 26

2.5.1 Indentation mechanics 27

2.5.2 Nanoindentation sample preparation . . . 32

2.5.2.1 Mechanical polishing 32

2.5.2.2 Focus ion beam milling 34

2.5.2.3 Nanoparticle deposition for *in situ* indentation . 36

2.5.3 *Ex situ* indentation 38

2.5.4 SEM *in situ* indentation 39
2.5.5 TEM *in situ* indentation 41
2.5.6 Confocal Raman microscopy 43

Chapter 3 – SiC thin film composites **48**

3.1 Overview 48
3.2 SiC-TiX multilayer composites 49
3.2.1 Structure and composition 50
3.2.2 Elastic-plastic response 54
3.2.3 Fracture response 57
3.2.4 Wear resistance 62
3.3 SiC thin films 67
3.3.1 Elastic-plastic response 68
3.3.2 Fracture response 69
3.4 Summary 77

Chapter 4 – Si-SiC core-shell composites **79**

4.1 Overview 79
4.2 Thermal residual stresses 79
4.3 Si nanotower growth and processing 82
4.4 Deposition of SiC coatings on Si nanotowers with Au caps (batch A) 83
4.5 Indentation of batch A composite towers 91
4.5.1 Elastic-plastic response of FIB milled towers . . 92
4.5.2 Fracture and phase transformation of FIB milled towers . 95
4.5.3 *In situ* indentation of as-deposited towers . . . 108
4.6 Confocal Raman microscopy of batch A composite towers . 116
4.7 Deposition of SiC coatings on Si nanotowers without Au caps (batch B) 120
4.8 Residual stress analysis of batch B composite towers . . 125
4.9 Summary 133

Chapter 5 – Uniaxial compression of Si nanospheres and towers 135

5.1 Overview 135

5.2 Strength 135

5.3 Toughness 146

5.4 Phase transformations 152

5.5 Summary 156

Chapter 6 – Conclusions and future direction 158

6.1 Summary 158

6.2 Future work 163

References 170

List of Tables

Table 1.1 Sources of variability associated with *in situ* mechanical testing 9
Table 3.1 Mechanical properties for materials relevant to SiC thin films 48
Table 3.2 SiC film hardness and modulus on Si(100), Mo, and Al_2O_3 substrates 68
Table 4.1 Elastic CTE stresses for Si in Si-SiC concentric cylinders . 81
Table 4.2 Elastic CTE stresses for Si in Si-SiC concentric spheres . 81

List of Figures

Figure 1.1 Examples of hip replacement joints 3
Figure 1.2 Qualitative relationship between strength and toughness . 5
Figure 2.1 Hypersonic plasma particle deposition (HPPD) schematic . 11
Figure 2.2 HPPD experimental setup 12
Figure 2.3 Optical images of SiC films 15
Figure 2.4 Particle size distribution for SiC nanoparticle production . 18
Figure 2.5 SiC growth morphology at various radial locations . . 20
Figure 2.6 SiC XPS depth profile and XRD spectrum . . . 21
Figure 2.7 Spatially resolved XRD and texture coefficient for SiC . 23
Figure 2.8 Spatially resolved hardness and elastic modulus for SiC . 24
Figure 2.9 Rapid thermal annealing (RTA) instrument schematic . 25
Figure 2.10 RTA temperature-time profiles 26
Figure 2.11 Indentation load-displacement schematic . . . 29
Figure 2.12 Cross sectional and diagonal polishing . . . 34
Figure 2.13 FIB milling for *ex situ* indentation 35
Figure 2.14 FIB milling for *in situ* indentation 36
Figure 2.15 Nanoparticle deposition for *in situ* indentation . . 37
Figure 2.16 Experimental setup for SEM *in situ* indentation . . 41
Figure 2.17 TEM *in situ* indentation holder and tip . . . 43
Figure 2.18 Experimental setup for confocal Raman microscopy . 46
Figure 2.19 Raman shift as a function of laser power . . . 47
Figure 3.1 Cross sectional SEM and EDS of SiC-TiX multilayers . 50
Figure 3.2 Spatially resolved height images for SiC-TiX multilayers . 52
Figure 3.3 XPS profiles for SiC-TiX multilayers . . . 53
Figure 3.4 Layer-by-layer hardness and modulus for SiC-TiX multilayers 55
Figure 3.5 Ductile phase crack pinning in SiC-TiX multilayers . 57

Figure 3.6	SiC-TiX response for indentation through multiple interfaces	59
Figure 3.7	SiC-TiX response for indentation of a single interface .	61
Figure 3.8	Wear resistance ratio H^3/E^{*2} for SiC-TiX multilayers .	64
Figure 3.9	Wear tracks from scratch testing on SiC-TiX multilayers .	66
Figure 3.10	XRD spectrum for SiC film on Mo	67
Figure 3.11	Fracture toughness as a function of RTA temperature for SiC films	70
Figure 3.12	Fracture toughness as a function of RTA for SiC on Si(100)	71
Figure 3.13	Indentation impressions for bare Si(100) and SiC on Si(100)	72
Figure 3.14	Cross sectional image of an indentation into a SiC film on Si(100)	73
Figure 3.15	Indentation impressions for SiC films on Mo as a function of RTA temperature	74
Figure 3.16	Indentation impressions for SiC films on Mo as a function of maximum displacement	76
Figure 4.1	Vapor-liquid-solid (VLS) Si nanotowers . . .	83
Figure 4.2	Deleterious effects of HF, KI/I_2 etching on VLS Si nanotowers	84
Figure 4.3	SiC coated Si nanotower (batch A)	85
Figure 4.4	FIB milled Si-SiC composite tower surface . . .	86
Figure 4.5	Cross sectional SEM and EDS of Si-SiC composite tower (batch A)	87
Figure 4.6	Cross sectional SEM imaging of Si-SiC composite tower (batch A) as a function of RTA temperature . .	88
Figure 4.7	Cross sectional AFM imaging of Si-SiC composite tower (batch A) as a function of RTA temperature . .	89
Figure 4.8	Si-SiC composite tower (batch A) hardness as a function of tower diameter and ratio of plastic zone diameter to tower diameter on cross sectioned surface	93

Figure 4.9 Si-SiC composite tower (batch A) modulus as a function of tower diameter and contact stress on cross sectioned surface 95
Figure 4.10 Load-displacement and post indentation SEM imaging on Si-SiC composite tower cross sections (batch A) for displacements from 50-175 nm maximum displacements . . . 97
Figure 4.11 AFM height data for 75 nm indent into Si-SiC composite tower cross section (batch A) 99
Figure 4.12 Fracture toughness of Si-SiC composite tower as a function of tower diameter (batch A) 101
Figure 4.13 Load-displacement data with power law fit to the unloading curve 102
Figure 4.14 Characteristic load-displacement curves from Gerbig et al. 104
Figure 4.15 Load-displacement data replotted from Ge et al. with power law fittings to unloading curve 106
Figure 4.16 Transition pressure on unloading for the Si II→I phase transformation as a function of critical dimension for Si-SiC composite towers (batch A), Si wedges, and bulk Si(111) . 107
Figure 4.17 Tip-sample misalignment problems during SEM *in situ* indentation of Si-SiC composite towers (batch A) . . 109
Figure 4.18 Unstable crack growth during SEM *in situ* indentation of Si-SiC composite towers (batch A) 111
Figure 4.19 Stable crack growth during SEM *in situ* indentation of Si-SiC composite towers (batch A) 113
Figure 4.20 SEM *in situ* indentation of Si-SiC FIB milled composite towers (batch A) 115
Figure 4.21 SEM *in situ* indentation of Si-SiC FIB milled composite towers after 1200°C RTA treatment (batch A) . . . 116
Figure 4.22 Biaxial stress as a function of RTA treatment temperature for Si-SiC composite towers (batch A) 117

Figure 4.23	Raman spectra for Si-SiC composite towers (batch A) .	119
Figure 4.24	Si nanotowers before and after SiC coating (batch B) .	121
Figure 4.25	Cross sectional SEM imaging of Si-SiC composite tower (batch B) as a function of RTA temperature . . .	122
Figure 4.26	Cross sectional AFM imaging of Si-SiC composite tower (batch B) as a function of RTA temperature . . .	122
Figure 4.27	Si core height after RTA as a function of treatment temperature (batch B)	123
Figure 4.28	Strain rate as a function of applied stress for Si-SiC composite towers (batch B)	125
Figure 4.29	Raman spectra for Si-SiC composite towers as a function of RTA treatment temperature (batch B) . . .	127
Figure 4.30	Raman spectra for Si-SiC composite towers at different focal heights (batch B)	127
Figure 4.31	Raman shifts for Si-SiC composite towers (batch B), SiC films, and bare Si(111) as a function of RTA treatment temperature	129
Figure 4.32	Biaxial stress as a function of RTA treatment temperature for Si-SiC composite towers (batch B)	129
Figure 4.33	Raman spectra for 1200°C RTA treated Si-SiC composite (batch B)	131
Figure 4.34	DF TEM strain contrast in Si-SiC composites (batch B) .	133
Figure 5.1	TEM *in situ* indentation of a Si nanosphere on a Si(100) substrate	137
Figure 5.2	Si nanosphere post indentation imaging after five consecutive TEM *in situ* indentations	139
Figure 5.3	Si nanosphere load-displacement data after five consecutive TEM *in situ* indentations	140
Figure 5.4	Average flow stress as a function of Si nanosphere and nanotower diameter	142
Figure 5.5	TEM *in situ* indentation of a Si nanotower . . .	143

Figure 5.6 Video frame captures during TEM *in situ* indentation of a Si nanotower 145
Figure 5.7 Fracture of a Si nanosphere during TEM *in situ* indentation 147
Figure 5.8 Work per unit fracture area schematic for spheres and towers 148
Figure 5.9 Fracture toughness as a function of Si nanosphere and nanotower diameter 150
Figure 5.10 TEM *in situ* indentation of a Si nanosphere showing a phase transformation 153
Figure 5.11 Transition pressure on unloading for the Si II→I phase transformation as a function of critical dimension for Si-SiC composite towers (batch A), Si wedges, bulk Si(111), and Si nanospheres 153
Figure 6.1 Schematic representation of a proposed toughening mechanism for Si embedded SiC 163
Figure 6.2 Schematic of the proposed experiment to test the phase transformation toughening mechanism . . . 164
Figure 6.3 Si-SiC composite growth from Au patterned Si(111) substrates 166
Figure 6.4 Codeposition of two independent reactant species using a dual nozzle design 167
Figure 6.5 Nanowire growth during the codeposition process . . 165

Chapter 1: Introduction and motivation

1.1 Overview

This dissertation considers the development of materials with both high toughness and strength for applications involving excessive wear. This involved three major thrusts, the first being the deposition of nanocrystalline SiC films using hypersonic plasma particle deposition. Chapter 2 discusses improvements made to the film structure through an understanding of a hybrid growth mechanism. In addition, non-standard mechanical characterization techniques are reviewed, including *in situ* indentation and stress analysis using confocal Raman microscopy. The second thrust was the deposition and mechanical testing of SiC based composites as multilayers and core-shell nanotowers, as discussed in Chapters 3 and 4, respectively. In both cases, the role of thermal residual stress was analyzed as it impacts fracture processes. The last thrust was with TEM *in situ* indentation experiments on Si nanospheres and nanotowers and is presented in Chapter 5. Dislocation pile-up and shielding mechanisms are used to explain increases in strength and toughness, respectively, with decreasing diameter. In addition, a fundamental change in the deformation mechanism of Si at dimensions less than ~100 nm is proposed for anisotropic loading. Finally, Chapter 6 summarizes the overall findings and suggests future directions of the research. In addition, a new toughening mechanism is proposed for ceramic nanocomposites based on the results of Chapters 4 and 5.

1.2 Motivation

Wear is a fundamental problem in many engineering systems where two or more contacting surfaces are in relative motion. This can lead to the deformation and ultimately the failure of a device. The economic impact of wear in the US, from sources including early part replacement, production downtime, and energy losses, has been estimated by Oak Ridge National Labs to be in excess of $100 billion annually [1]. In addition, there is an environmental concern, since applications that include high wear rates often depend on hazardous coolants and lubricants. Wear-resistant coatings play an important role in minimizing these costs by improving a device's efficiency and lifetime. Industrially, these types of coatings have a wide range of applications, including automotive, aircraft, electronics, manufacturing, and biomedical [2]. In the processing of steel, TiC coatings on tools used for punching holes can increase the tool lifetime by 200 times [3] while TiN coatings on cutting blades can increase lifetimes by 10 times [4]. Wear-resistant coatings can also provide energy savings, as in the case of automotive piston rings, where TiN coatings reduce wear rates by up to 70% and help the engine run more efficiently [5].

One application with an increasing demand for wear resistant materials is in synthetic joint replacements. Total joint arthroplasty (or replacement) procedures are generally used to treat cases of excessive wear in knee and hip joints. In the case of a hip replacement, synthetic materials are needed for both the ball and socket joint that can withstand many years of wear *in vivo* (see Fig. 1.1). The most common materials used in these replacements include polyethylene (PE), cobalt chromium alloys (CoCr),

and alumina (Al_2O_3). Of these, the ball-socket combination of CoCr-PE currently account for greater than 50% of the hip replacements in the US despite wear-related problems with both materials [6-8]. In the case of PE, high wear rates lead to a build up of wear debris in the joint. This can cause inflammation of the joint and osteolysis (degradation of bone). The use of CoCr is also problematic, as metal ions are released into the blood stream from the wear process. Al_2O_3-Al_2O_3 combinations practically eliminate both of these problems due to a much lower wear rate [9, 10]. However, ceramic implants are much more prone to fracture due to low fracture toughnesses and a propensity to fail catastrophically. When ceramic joints fail *in vivo*, the consequences can be fatal. Over the last three decades, manufacturers of Al_2O_3 components have decreased the fracture rate from 0.026% to 0.004% (with more than 1.5 million tested) due to a combination of decreasing the average grain size (7.2 to 1.8 μm), increasing the density (3.94 to 3.98 g/m^3), and increasing the Vickers hardness (1800 to 2000) [10].

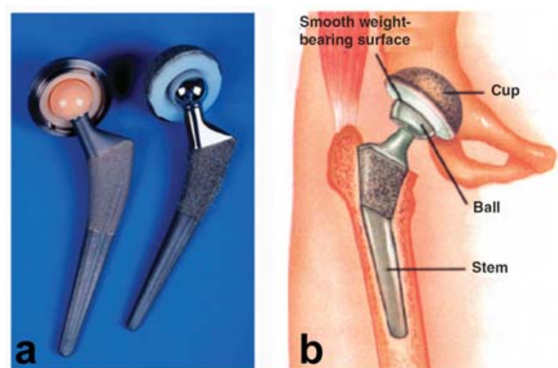

Figure 1.1 Examples of hip replacement joints, with a) an Al_2O_3-Al_2O_3 ball-socket (left side) and CoCr-PE ball-socket (right side) and b) a hip joint *in vivo*. Adapted from Rahaman et al. [11].

Despite these improvements in reliability, there is an increasing demand for improved implant performance. In the US alone, there were in excess of 500,000 joint (knee and hip) replacement surgeries in 2002 [12]. This number is projected to increase rapidly in the next 20 years due to demographic changes, including increases in the average age (and susceptibility to arthritis), average body mass index (more overweight or obese), and level of education (leading to a greater role in healthcare decisions) [12]. In addition, the majority of patients needing joint replacement surgery will be under 65 years of age by 2011, which will require implants that can withstand longer and more active lifestyles [6]. Thus, to prevent *in vivo* fracture, revisionary operations, and limitations on lifestyles, new materials are needed to replace the existing technology.

1.3 Materials development

Material wear is a complex interaction that is dependent on elastic, plastic, and fracture properties. Tribology based models have typically been of the form

$$W^{-1} = H^{x} E^{y} K_{Ic}^{z} \tag{1.1}$$

where W^{-1} is the resistance to wear, H is the hardness, E is the elastic modulus, and K_{Ic} is the fracture toughness. Many empirical combinations of (x, y, z) have been proposed, with values ranging from -2 to +3 [13-17], but are generally limited to a very narrow set of materials or types of wear. Figure 1.2 shows qualitatively how these design variables are related in most structural materials in terms of their toughness (K_{Ic}) and strength (or resistance to both elastic (E) and plastic (H) deformation). The tradeoff between toughness and strength in currently available materials is difficult to reconcile in wear

environments, since materials should ideally have both a high strength and toughness [16, 18]. Research in hard coatings has tried to address this problem by developing superhard materials, i.e. materials that have hardnesses greater than 40 GPa [19-21]. Veprek et al. [19] attributes superhardness to either the intrinsic nature of the material, such as diamond like carbon (DLC) or cubic boron nitride (c-BN) or a film's nanostructure, such as heterostructures or nanocomposites. Superhard nanocomposites are formed by combining two hard phases, such as TiN/BN (*H*=69 GPa) [22], or by surrounding a hard phase with a thin amorphous layer, such as TiC/a-C (*H*=32 GPa) [23]. While these materials are significantly harder than their monolithic counterparts, they show little improvement in their fracture response and continue to fail in a brittle manner.

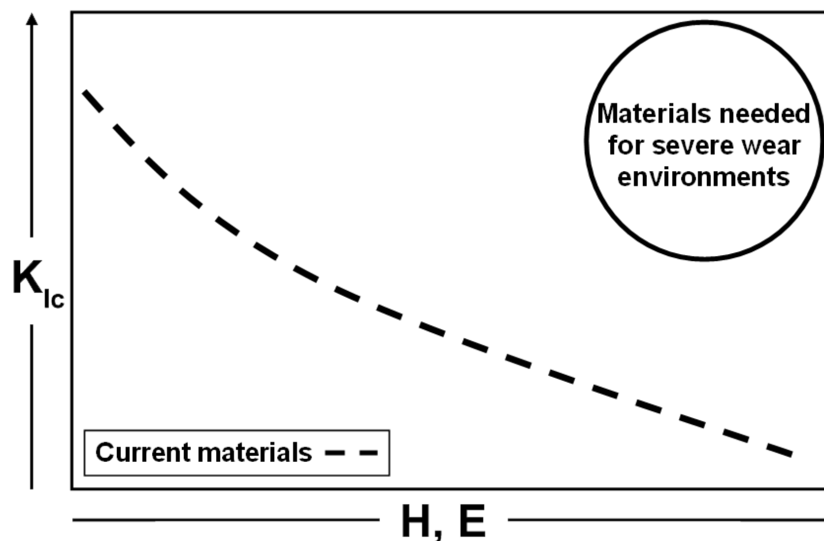

Figure 1.2 Qualitative relationship between fracture toughness (K_{Ic}), hardness (*H*), and elastic modulus (*E*). Adapted from Zum Gahr, et al. [13].

This problem has also been studied, with some success, by the fracture mechanics community in the toughening of bulk ceramics [24-27]. The toughening strategies applied to ceramic materials involve either minimizing the number of flaws in a material during processing (particularly for small structures) or controlling the micro(nano)structure to increase its flaw tolerance. One of the most successful examples of the latter is in the transformation toughening of partially stabilized zirconia (PSZ) [28, 29]. Under atmospheric pressure and room temperature, the monoclinic phase of ZrO_2 is the most thermodynamically favorable. However, a tetragonal phase can be stabilized at these conditions by adding second phase particles, such as MgO, CaO, or Y_2O_3, or kinetically trapping the tetragonal phase during processing. During crack growth in the PSZ, the stress field destabilizes the surrounding matrix and provides the energy needed to overcome the nucleation barrier for the transformation from tetragonal to monoclinic. This involves an expansion of the transformed material and puts the transformed zone into compression, thus absorbing fracture energy and inhibiting further crack growth. This can increase the fracture toughness by a factor of four to ten (up to K_{Ic}~20 MPa*m$^{1/2}$) depending on the stabilizer and processing conditions [28].

Recently, Zhan et al. has applied second phase reinforcement at a much smaller scale in the development alumina composites with dispersed single-wall carbon nanotubes (SWNT) [30]. These composites are spark-plasma sintered alumina powder with SWNTs to form a 200 nm grain alumina matrix with embedded SWNTs of ~2 nm in diameter and lengths of 0.2-1 μm. When these composites contain 10 vol% SWNTs,

they show a fracture toughness (9.7 MPa*$m^{1/2}$) and hardness (9.3 GPa) that more than doubles what was reported in earlier work by Niihara et al. [31] for microcrystalline Al_2O_3 with 5 vol% embedded SiC nanoparticles (diameter ~ 80 nm). The authors attribute this increase in toughness to crack deflection at the SWNT inclusions. However, these improvements are still quite modest compared to monolithic Al_2O_3 (K_{Ic}=2.5 MPa*$m^{1/2}$, H=18 GPa [32]), suggesting that processing flaws continue to limit the development of truly ductile ceramics.

A fourth group (with the previous three being tribology, hard coatings, and fracture mechanics) that has recently become interested in this problem is the nanoindentation research community. Following the pioneering work of Uchic et al. [33], *in situ* (including TEM, SEM, Raman, XRD) uniaxial compression experiments on two dimensional structures have looked at the extrinsic size effects on mechanical deformation. This work has been focused mainly on dislocation dynamics in body centered cubic (Mo [34]) and face centered cubic (Ni [33], Au [35], Cu [36]) metals and has been the subject of extensive reviews [37-39]. A much smaller amount of work has looked at classically brittle materials, including semiconductors [40-45] and metallic glasses [46-48]. As with the studies on metals, compression of Si nanospheres and nanotowers show an increase in yield strength with decreasing sample size [40, 44, 45]. In addition, though, a critical transition size in the deformation mode from brittle fracture to ductile yielding has recently been observed in Si [41] and Zr-based metallic glasses [47]. In Si, similar transitions to ductile failure and increased toughness have been observed in other geometries and modes of failure, including cantilevers in

bending [49, 50] and nanowires in tension [51]. While these results are limited and need further investigation, the discovery of a transition from brittle to ductile failure based on a critical length scale suggests that ductile ceramics may become a reality.

However, it is also important to recognize the challenges associated with measurements at this length scale. The majority of the metal towers indented *in situ* are fabricated using focused ion beam milling of a bulk single crystal material. For milling with Ga^{+} at 30 keV on Cu, this can leave ions implanted 50 nm into the tower and cause precipitation hardening in the GPa range [52]. Even for samples that are grown to small dimensions rather than milled, such as VLS grown Si [53], there are additional artifacts that can overshadow any true size effect. For instance, consider two studies using *in situ* tensile testing of Si nanowires with diameters of 10-100 nm to determine the role of nanowire diameter on the failure mode. Han et al. [51] found a high strains (decrease in diameter of up to 600%) before ductile failure in 20 nm diameter wires while another group led by Zhu et al. [54] found brittle failure for all diameters down to 10 nm. While it is unclear the exact reason for this difference, Table 1.1 suggests three possible sources of discrepancies associated with the experimental conditions and sample preparation that could affect the failure mechanism of the nanowires. This illustrates the importance of both the sample and testing conditions when mechanically testing small volumes. Thus, with the proper precautions, *in situ* indentation can be a powerful tool for the development of ductile ceramics.

Table 1.1 Sources of variability associated with *in situ* mechanical testing

source	Han et al. [51]	Zhu et al. [54]	effect
electron beam	TEM at 200 kV	SEM	enhanced dislocation motion in the TEM due to higher power densities [55]
surface oxide thickness	3-4 nm	none	compressive stress on the Si core due to the oxide [56]
wire growth direction	[110]	[111]	[111] Si nanowires have been shown to be more brittle than [110] nanowires [57]

The present dissertation research approaches the development of ductile ceramic nanocomposites using concepts from each of the research areas outlined above. First, nanocrystalline SiC coatings were deposited using an aerosol based deposition technique. This avoids the problems associated with large volume ceramic processing techniques by depositing a dense thin film with a decreased probability of containing a critical flaw (thin film vs bulk). In addition, the process generates a coating that approaches superhardness. Fracture mechanics concepts including ductile phase pinning and phase transformation toughening were then applied to multilayer and core-shell nanotower structures to enhance the fracture toughness. Finally, *in situ* indentation of Si nanospheres and nanotowers was then used to identify size dependent deformation mechanisms in Si. Based on the results from each of these sets of experiments, a new toughening mechanism for Si-SiC nanocomposites is proposed with the potential of achieving high strength and ductility.

Chapter 2: Experimental

2.1 Overview

This chapter reviews the sample deposition process and key characterization methods used in the current research project. The first two sections discuss the deposition of SiC thin films using hypersonic plasma particle deposition and the structural characterization of these films. The following section reviews rapid thermal annealing (RTA) treatments that were used in post deposition processing. The final section reviews the methods used for mechanical characterization of the samples, namely nanoindentation and confocal Raman microscopy (CRM). This includes a discussion of indentation mechanics, sample preparation techniques, and *in situ* indentation methods.

2.2 Hypersonic plasma particle deposition (HPPD)

The hypersonic plasma particle deposition (HPPD) system was developed in the mid 1990s by Girshick et al. as a high rate deposition (2-20 μm/min over a ~1 cm diameter substrate) process for nanostructured films [58, 59]. The process is based on the gas phase nucleation of nanoparticles in a thermal plasma and subsequent impaction to rapidly form particulate films. Figure 2.1 shows a schematic diagram of the system. Reactants are fed through a converging nozzle into a low pressure chamber. This leads

to both an acceleration and supersaturation of the reactants. The resulting nanoparticles are then impacted on a substrate at high velocities (up to ~2 km/s).

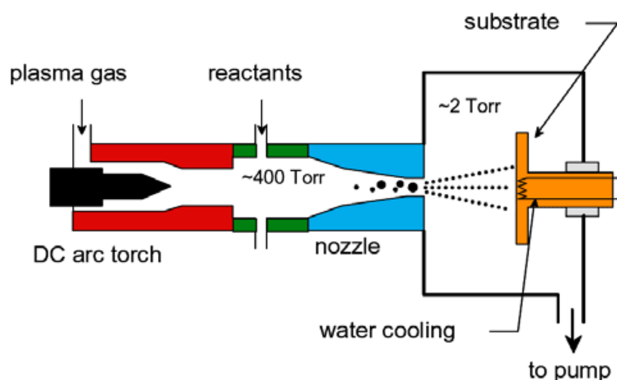

Figure 2.1 Hypersonic plasma particle deposition (HPPD) schematic. Image reproduced with permission from J. Hafiz's Ph.D. thesis [60].

The main components of the HPPD system are the reactant delivery system, plasma torch, gas injection holder, injection nozzle, vacuum system, and cooling water system. Figure 2.2 shows the inside of the deposition chamber and highlights some of these components. Gases are fed directly to the nozzle while liquid precursors are pressurized in a bubbler setup that uses argon as both a diluent and carrier gas. Reactant flow rates from the bubbler are controlled by regulating the temperature, pressure, and carrier gas flow rates and calculating the reactant vapor pressure. The plasma torch is a Miller SG-1B gun consisting of a copper anode and cathode machined by Thermach Inc. The cathode tip and inside wall of the anode are coated with tungsten to prevent melting and erosion. The gas injection holder has evenly spaced slits along the wall to stabilize the plasma gas flow. The injection nozzle is made of boron nitride and has been designed to nucleate nanoparticles. Further details about the nozzle design are

discussed in the following paragraph. The vacuum system consists of three pumps in series, with a liquid-ring pump followed by a rotary vane backing pump and a roots booster pump. The liquid ring pump removes water-soluble waste products, in particular HCl. The deposition chamber, torch, and nozzle are cooled with high pressure (~120 psi) deionized water.

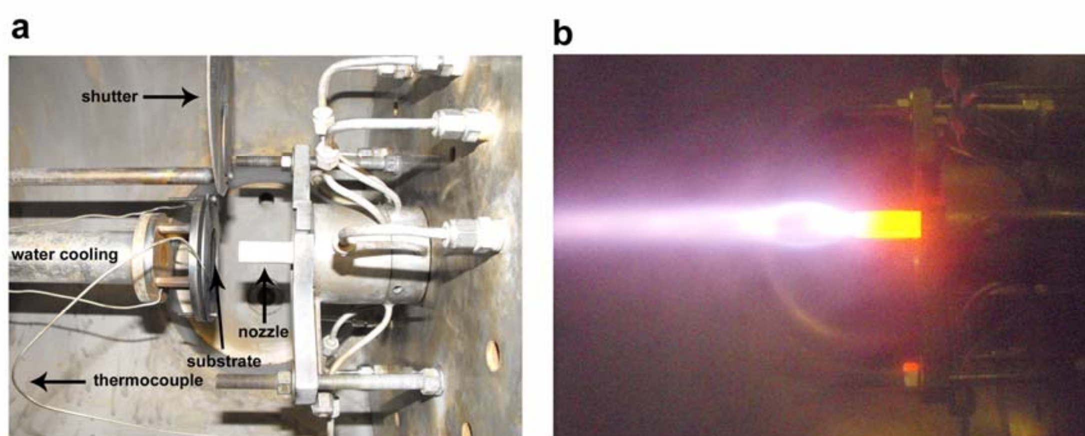

Figure 2.2 HPPD chamber, showing the key components from the torch and substrate (a), along with the an image of the torch running at ~9 kW and 30 slm Ar (b). Note that in (b) there is no substrate holder present, so a Mach disk is observed rather than a bow shock.

The original subsonic system was based on a nucleation nozzle designed by Wei [61] and a reactor design fabricated by Hatch [62]. Wei's nozzle design included a converging inlet for rapid quenching and a straight region for uniform particle growth. The effectiveness of the design was shown both by experimental measurements of particle sizes [63, 64] and numerical nucleation simulations [64]. Rao et al. [58, 59, 65] introduced a hypersonic expansion to the system that helped minimize particle

agglomeration in-flight. The supersonic flow generates smaller particles due to a shorter in-flight residence time and faster cooling rate. The supersonic flow also improved particle collection efficiency by shifting from deposition on a cold-walled chamber by thermophoresis in the subsonic system to inertial impaction in the supersonic system. The most recent change to the system was the modification of Wei's nozzle design by Gidwani to minimize the production of large (tens of microns) particles [66]. The previous design suffered from fluid recirculation at the nozzle inlet, which was eliminated by matching the torch exit diameter to the nozzle inlet.

All of the films discussed in this thesis were deposited at an axial distance of 2 cm downstream of the nozzle exit (see Fig. 2.2) due to the presence of a bow shock in the gas flow. The location of the bow shock was verified through experimental measurements [67] and modeling [66], which show the bow shock to occur around 2.5 mm upstream of the substrate for the operating conditions in the current study. At this point, the gas moves radially outward and a stagnation region is formed between the bow shock and the substrate. As discussed in Chapter 3, this leads to a strong variation in the film structure depending on radial location on the substrate. Initial work involved SiC single layer films and SiC-TiX multilayers (Section 2.3 and 3.2, respectively) that were deposited on 20 mm diameter Mo substrates centered with respect to the plasma jet ($r = 0$). Subsequent SiC films (Section 3.3) and SiC coated Si nanotowers (Chapter 4) were deposited at radial positions of $r = 19$ mm. This location was found to have the most homogeneous film growth, showing minimal evidence of pores or agglomerated structures. Figure 2.3 shows representative optical images of representative films at $r =$

0 mm (a) and r = 19 mm (b). The films at r = 0 mm use a substrate holder that is made for Mo substrates that are machined to include an outer lip for clamping to the holder (see Hafiz's thesis for details [60]). For the films at r = 19 mm, a new substrate holder was designed to deposit films at larger radial distances than the previous design and to hold substrates that could not be machined (most notably, the Si nanotower samples used to deposit the core-shell structures in Chapter 4). The holder consists of a base and cover that are bolted together (see Fig. 2.3c). The base has four pockets (diameter ~3.2 mm) to hold substrates with thicknesses less than 0.5 mm. The cover has four holes that have slightly smaller diameters (~2 mm) and are lined up over the pockets. This secures any substrate that has a longest dimension between 2 to 3.2 mm. Figure 2.3b shows an example of a deposition on Si, where the area that the coating covers shows multi-colored Newton rings and the areas that are blocked by the cover are bare.

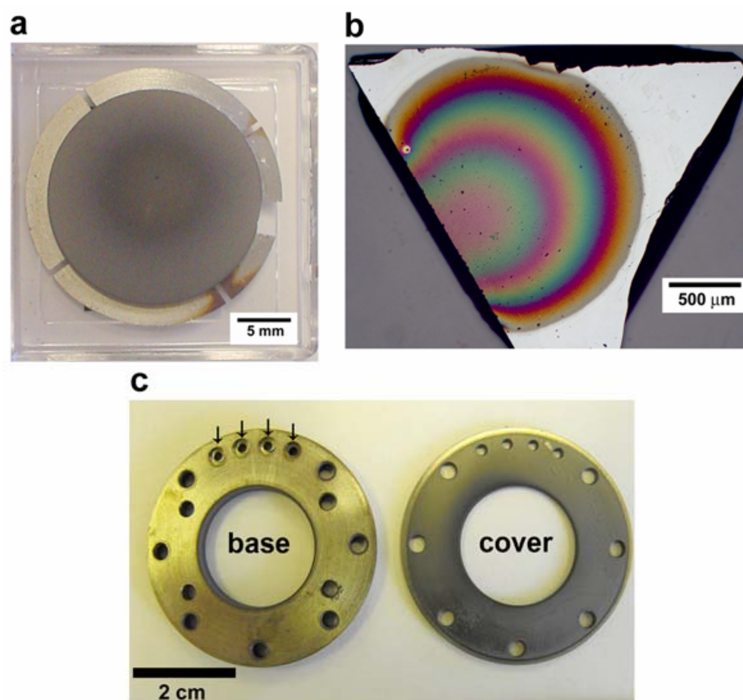

Figure 2.3 Optical images of the SiC films deposited on Mo at r = 0 mm (a), SiC films deposited on Si at r = 19 mm (b), and the holder used for the substrates at r = 19 mm (c). The arrows in (c) show the locations for the simultaneous deposition on four substrates.

2.3 SiC film deposition and growth mechanism

This section describes the growth mechanism of HPPD SiC and is adapted from a 2007 publication in Surf. Coat. Technol. [68]. In general, the growth rate of uniform thin films by chemical vapor deposition is limited by the concentration of reactants fed. At high degrees of supersaturation, particles nucleate in the gas phase and will deposit as clusters on the surface. This type of reaction typically leads to a disordering of the film and undesirable film characteristics. In the HPPD system, this limitation is used as a pathway to nucleate nanoparticles. In previous results from this system, the substrate

temperature was kept relatively low, typically in the range of 750 to 850°C [69]. These films showed poor adherence to the substrate and a high degree of porosity, most likely due to a combination of slow surface reactions and the rapid arrival of reactants. In the current series of experiments, it is proposed that the increase in substrate temperature has shifted the film growth from a surface reaction limited regime to a vapor-to-surface diffusion limited regime. Due to the decline in the concentration of particles deposited on the surface away from the center of the deposit, as shown previously in simulation results [66], there exists a radial gradient in the concentration of particles in the film. This hypothesis of a varying particle to CVD matrix is verified through observations of radial changes in the film morphology, crystallinity, and mechanical response.

Reactant flowrates for SiC films are typically in a 6:1 ratio of carbon to silicon, with silicon tetrachloride injected at 40 sccm and methane at 240 sccm. The torch is operated at approximately 200 A and between 8 to 10 kW. The plasma gas is a 10:1 mixture of argon and hydrogen with a total flow of 33 slm. Deposition temperatures ranged from 550 to 1250°C for between 4 to 10 minutes. Reported temperature readings are thermocouple measurements from the back of substrate (2.4 mm behind the surface) and are reported without a heat loss correction. Assuming a 1-D temperature distribution in the substrate, a constant thermal conductivity in the substrate, all the energy of the plasma (based on enthalpy measurements from the cooling water) goes toward heating the substrate, and only conductive resistance, the substrate surface temperature is approximately 80°C hotter than the measured temperature. The

background pressure in the chamber is ~0.1 torr, with a typical operating pressure of 2-3 torr during depositions.

In situ measurements of the particle size distributions were taken (with the help of L. Qi) at the substrate location at the same conditions that films were deposited using measurement techniques developed by Wang et al. [70]. Briefly, the aerosol jet is sampled using an ejector at the nozzle exit with an axial position that is the same as the substrate location during film deposition (2 cm downstream). The ejector works on the Venturi principle by forcing high pressure N_2 (450 kPa) through a restricting orifice to reduce the pressure at the ejector inlet to below that of the aerosol jet. The aerosol then passes through a bipolar charger (^{210}P), where the particles are ionized based on their size. The charged aerosol is then sent to a scanning mobility particle sizer (SMPS), which size selects certain particle sizes based on their electrical mobility and optically detects the number of particles in the aerosol stream. During $SiCl_4/CH_4$ injection, the particle size distribution showed that the concentration increases more than three orders of magnitude compared to the plasma gases alone, suggesting particle formation in the nozzle. Figure 2.4 gives a representative distribution, showing no obvious peak within the size range measured ($d_p \sim 4$ to 70 nm). This suggests that the peak particle diameter is no more than 4 nm and that most of the particles are less than 20 nm in diameter.

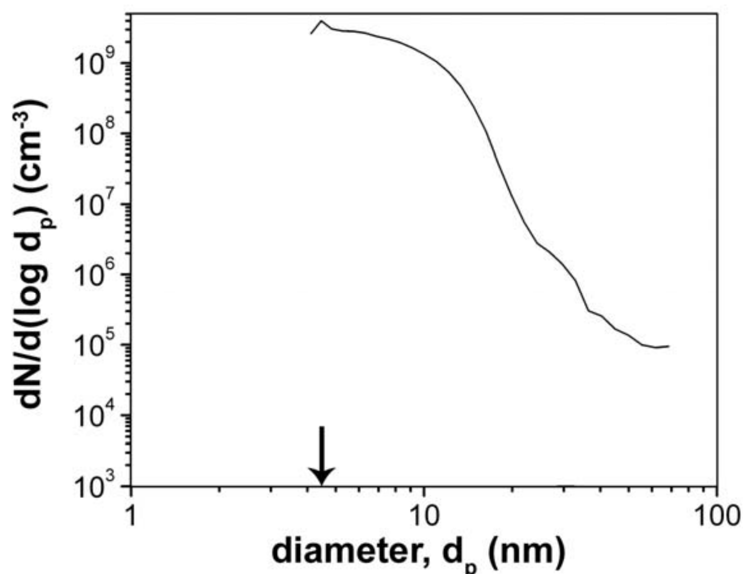

Figure 2.4 Representative particle size distribution for SiC nanoparticle synthesis at 40 sccm $SiCl_4$ and 240 sccm CH_4. The arrow indicates the position of the peak in the distribution.

While the particle size distribution results show that the nozzle is successfully nucleating particles, there is most likely also a significant amount of vapor produced that does not condense into nanoparticles. The deposition efficiency of the HPPD process, based on Si introduced into the system eventually being incorporated into the film, is approximately 1-2%. While this is partly due to a loss of particles below the impaction cut size ($d_p \sim 4$ nm), the low efficiency also suggests the presence of an excess of Si vapor that is not condensed to form nanoparticles. This excess vapor will form a stagnation layer above the substrate surface and produce relatively uniform CVD growth (in absence of particles). Separate experiments using the HPPD system have confirmed the potential for CVD growth, with results showing the growth of single crystal silicon nanowires on titanium catalyst particles through CVD growth [71].

However, prior results from high rate film depositions have shown a minimal presence of film growth by means other than particle impaction [72].

Figure 2.5 provides a qualitative overview of the film morphology as a function of radial position. Near the center of the film (Fig. 2.5a), the film structure appears to be composed ~100 nm particles in micron sized agglomerates. Moving radially outward, this cauliflower type structure becomes more regularly sized and there are fewer signs of porosity. A cross-sectional image of the film at this location (Fig. 2.5d) shows a columnar growth pattern and suggests an additional growth mechanism other than particle impaction. The average grain size at this location based on SEM image analysis of a polished surface is ~65 nm. At the furthest radial position (Fig. 2.5c), the film no longer shows the agglomerated features and the grain size is ~14 nm. These changes in morphology can be explained by decreasing contributions of particle impaction and increasing extent of CVD growth towards the outer edge. Particles larger than the cut-size diverge from their streamlines as they approach the substrate and impact the substrate ballistically while those smaller than the cut-size stay within the streamlines and flow around the substrate due to small inertial forces [66]. Since the radius at the nozzle exit is 2.5 mm, the largest particles will impact within a circular region close to this size. Moving radially outward, particles small enough to stay within the streamlines after exiting the nozzle but larger than the cut-size will impact at radial positions greater than 2.5 mm. This leads to a decreasing average size and concentration of impacted particles with increasing distance from the substrate center. Since there is a radially uniform stagnation layer for CVD growth, there is a relative increase in the

contributions of CVD growth at locations away from the center. Fig. 2.5 shows examples of columnar growth at r = 8 mm and then more equiaxed at r = 19 mm.

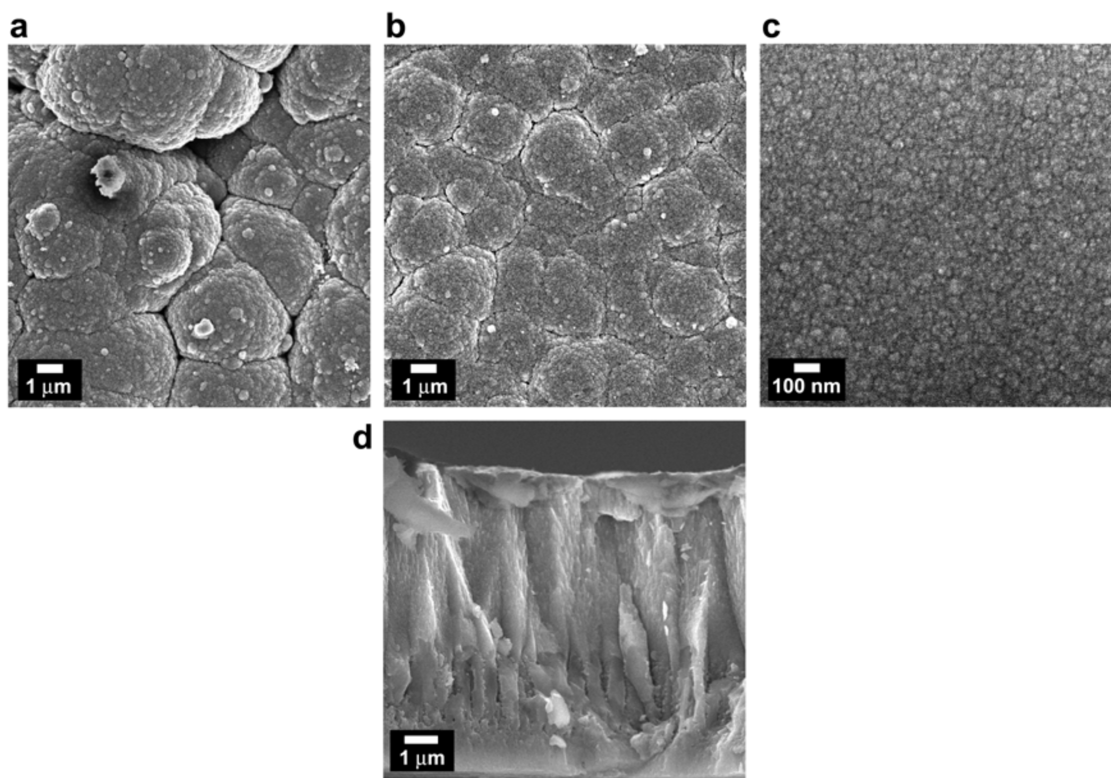

Figure 2.5 Growth morphology at various radial positions using SEM plan view (a-c) and cross-sectional images (d). Image (a) is near r = 0 mm, (b,d) are at r = 8 mm, and (c) is at r = 19 mm.

Figure 2.6a shows a XPS depth profile for a film deposited at 900°C after 50 minutes of sputtering, with XPS scans every ten minutes. While the sputter rate was not measured for the present samples, it is expected to be approximately 2 nm/min based on previous experiments with similar conditions [69]. As shown in the depth profile, the bulk of the film is approximately 44% silicon, 46% carbon, and 10% oxygen. Initially, there is a large drop in the oxygen concentration due to rapid sputtering of a thin oxide

layer formed from exposure to the atmosphere. However, the oxygen content in the bulk then stabilizes at approximately 10%. This is likely due to air leaks in the deposition chamber. Figure 2.6b shows a characteristic spectrum of a film deposited at 950°C. Crystalline peaks for Si and β-SiC are labeled. The presence of β-SiC is in agreement with previously published TEM analysis of particles scrapped from the top of HPPD deposited films that showed primarily β-SiC particles with some Si particles [69].

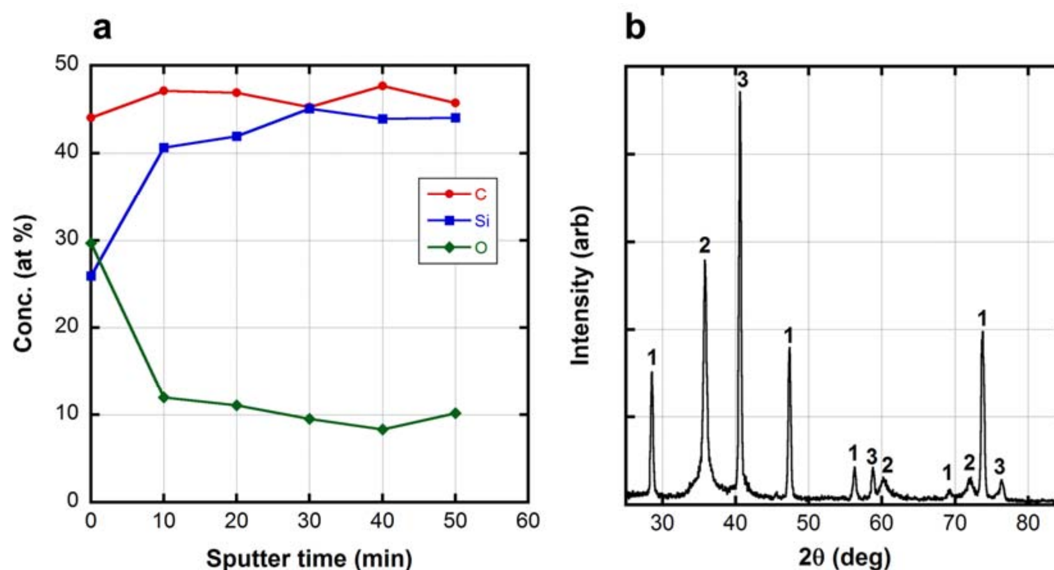

Figure 2.6 XPS depth profile (a) and XRD spectrum (b) for a representative SiC film deposited on Mo. The XPS profile shows the atomic conc. for carbon (red, circles), silicon (blue, squares), and oxygen (green, diamonds). The XRD spectrum has peaks labeled for Si (1), 3C-SiC (2), and Mo (3).

Silicon carbide grown by CVD has shown a preferred growth orientation that is dependent on the growth temperature [73], with the (111) plane being lower in energy up to approximately 1200°C and the (220) and (311) becoming increasing stable at

higher temperatures. The extent of preferred orientation can be quantified in a texture coefficient, which compares the intensities of characteristic peaks and is given by [73]:

$$TC_{(hkl)} = \frac{I_{(hkl)} / I_{0(hkl)}}{1/N\left[\sum\left(I_{(hkl)} / I_{0(hkl)}\right)\right]} \tag{3.1}$$

where $TC_{(hkl)}$ is the texture coefficient of the *(hkl)* peak, $I_{(hkl)}$ is the measured intensity, $I_{0(hkl)}$ is the standard intensity, and N is the number of preferred growth orientations. XRD spectra were also collected using a fine beam spot (100 μm) at varying radial distances from the substrate center of a film deposited at 950°C (see Figure 2.7a). The corresponding texture coefficients for the (111), (220), and (311) oriented grains are shown in Figure 2.7b. There is a distinct increase in the texture coefficient for (111) growth with increasing distance from the substrate center. This is in contrast to previously reported SiC films deposited at 850°C, where texture coefficients for both the (111) and (220) were approximately one, or randomly oriented [69]. This result further supports the idea of an increasing amount of CVD film growth relative to particle impaction in the outer portions of the substrate.

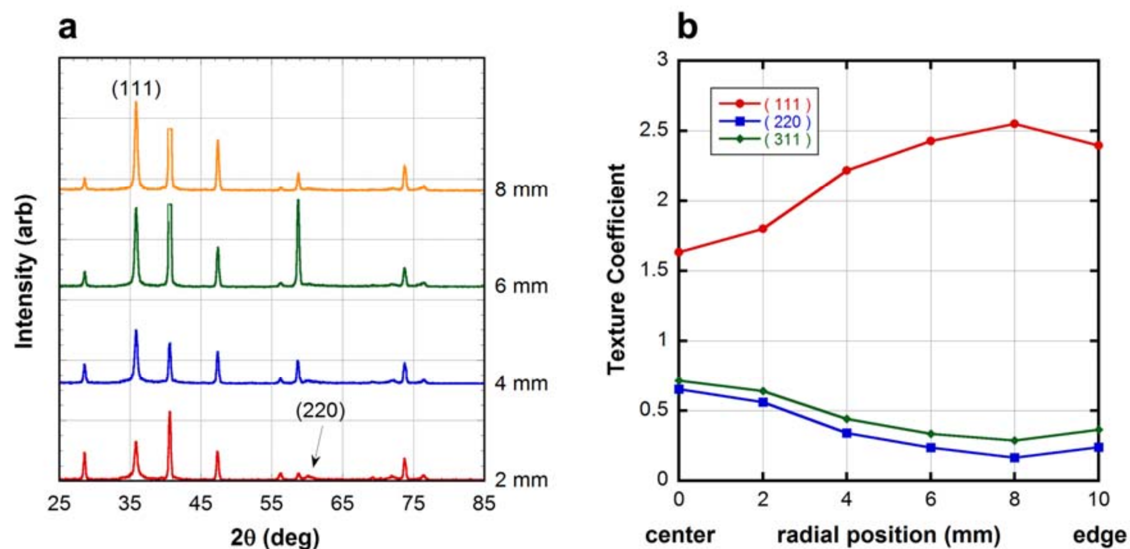

Figure 2.7 Spatially resolved XRD spectra in the radial (a) and the texture coefficient for the (111), (220), and (311) SiC growth (b).

One final piece of evidence for this proposed growth mechanism is from indentation results. Prior to indenting, the top surfaces of the films were mechanically polished (see Section 2.5.2.1). Dynamic indentations were run on the Nanoindenter XP® with a Berkovich tip (r_{tip} = 100 nm), with measurements averaged over 100 nm displacements. The average hardness of the films at r = 8 mm was 38.2 $\pm$ 2.6 GPa, with the corresponding modulus at these locations of 370.5 $\pm$ 19.0 GPa. Figure 2.8 shows how the hardness and modulus vary as a function of radial location. These trends agree with the changes observed in the morphology (Fig. 2.5), since there should be an increase in the hardness of the present films from both a refinement of the grain structure and decrease in porosity and increase in modulus due to decreasing porosity. While measurements of the fracture toughness showed less spatial variation, extensive porosity inside of r = 3 mm made measurements impossible. Based on 32 measurements

between r = 3-10 mm, the fracture toughness was found to be 6.03 $\pm$ 1.95 MPa*m$^{1/2}$, which is significantly larger than 3.3 MPa*m$^{1/2}$ reported for bulk SiC [32]. Explanations for this increase, including the role of a ductile secondary phase, are discussed in Chapter 3.

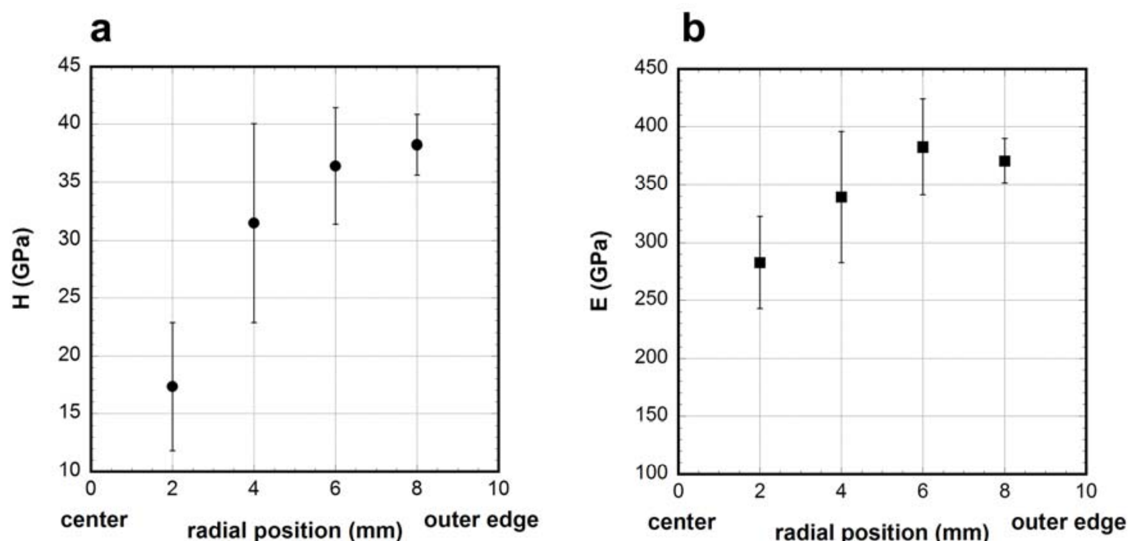

Figure 2.8 Spatially resolved hardness and modulus results from indentation.

2.4 Post-deposition processing

Rapid thermal annealing (RTA) is used throughout the studies presented in this thesis as a means to induce thermal residual stresses in adjoining materials with mismatched coefficients of thermal expansion (CTE). A Modular Process Rapid Thermal Processer was used at the University of Minnesota's Nanofabrication Center (see Fig. 2.9). This equipment is designed to treat 150 mm silicon wafers for use in the semiconductor industry, however is capable of treating smaller sized samples. Radiative heating is provided by a bank of tungsten-halogen lamps that surround a quartz containment tube. These provide heating rates of up to 200°C/s in the range of 250-

1300°C. A high pressure (<75 psi) water cooling jacket and inert gas flow through the chamber is used for rapid cooling. Temperatures are monitored using a thermocouple for low temperature operations (<800°C) and a pyrometer for higher temperatures.

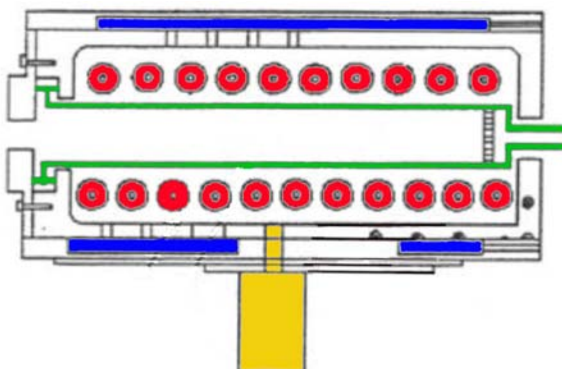

Figure 2.9 Schematic of the RTA instrument, showing the tungsten-halogen lamps (red), the water cooling (blue), the quartz isolation tube (green), and the pyrometer (yellow). This figure was adapted from the Modular Process Technology manual for the RTP-600S Rapid Thermal Processer.

Typical operating conditions involved purging the chamber with 8 slm Ar for 2 minutes, followed by heating at a rate of 50°C/s and a 20 sec hold at temperatures from 900-1200°C. Samples were cooled to less than 200°C before removing from the Ar environment. Figure 2.10 shows the temperature-time profiles for the typical operating conditions. Temperature readings are cut off below 400°C, as this is the lower limit of the pyrometer. Note that while the feedback control is able to maintain the prescribed heating rate (50°C/s), the cooling process has no feedback involved and is much slower (~1.5°C/s). It is also important to note that the measured temperatures are based on a pyrometer reading of the backside of a Si wafer that the samples sit on. Approximating the heat transfer as 1-D conduction through the Si wafer and sample and forced

convection at the free surface from the cooling gas, the sample reaches a homogeneous steady state temperature in less than 1 sec, even assuming a thick Mo substrate (~4.4 mm) and thick film (10 μm).

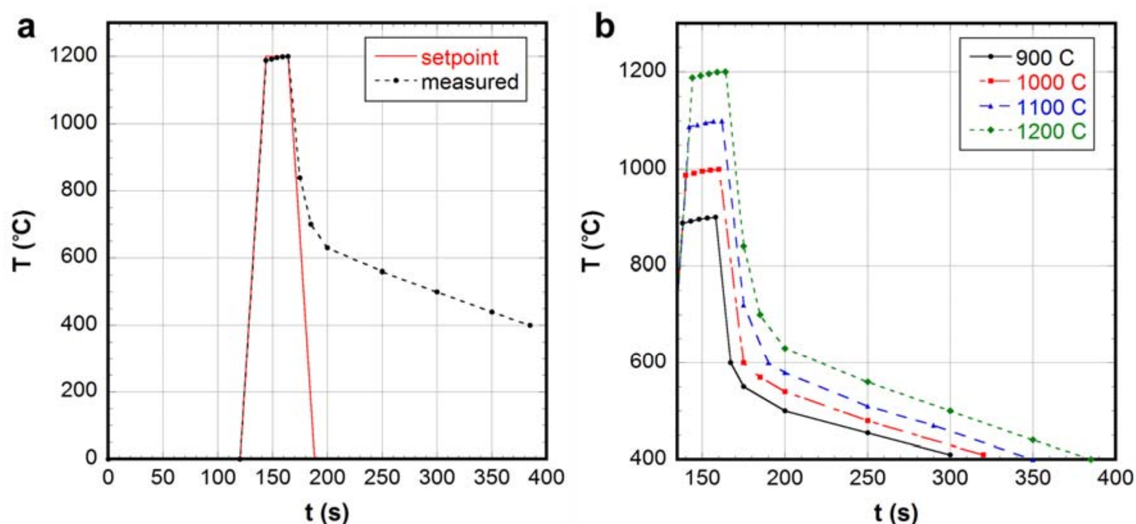

Figure 2.10 Rapid thermal annealing (RTA) temperature-time profiles, comparing the setpoint and measured response in (a) and showing the cooling profiles for each of the annealing conditions in (b). Temperature readings are cut off below 400°C, as this is the lower limit of the pyrometer.

2.5 Mechanical characterization

Most of the characterization techniques used in this work are standard tools in materials science research. These include electron microscopy (SEM, TEM), x-ray diffraction (XRD), x-ray photoelectron spectroscopy (XPS), and scanning probe microscopy (AFM). In addition, two non-standard techniques were used to probe the mechanical properties of interest: electron microscopy (SEM, TEM) *in situ* indentation and confocal Raman microscopy (CRM). Both of these techniques are new, either in their existence (EM *in situ* indentation) or in their application to mechanical properties

measurement applications (CRM). Therefore, the fundamentals and capabilities of these techniques are briefly reviewed. In addition, indentation mechanics and *ex situ* indentation are reviewed due to their extensive application in this work.

2.5.1 Indentation mechanics

The contact mechanics used to evaluate nanoindentation results are derived from Hertzian theory of elastic contact [74]. Hertz considered the contact of two continuous and non-conforming surfaces with radii of curvature R_1 and R_2. The effective radius is then

$$\frac{1}{R} = \frac{1}{R_1} + \frac{1}{R_2} \tag{2.2}$$

and reduces to $R = R_1$ for an indenter of radius R_1 indenting a flat surface. The total displacement δ into the flat surface can then be expressed as a function of applied load P, reduced modulus E^*, and indenter radius R as

$$\delta = \left(\frac{9P^2}{16RE^{*2}} \right)^{1/3} \tag{2.3}$$

The reduced modulus relates the modulus of the indenter and the sample and is equal to

$$\frac{1}{E^*} = \frac{\left(1 - \nu_1^2\right)}{E_1} + \frac{\left(1 - \nu_2^2\right)}{E_2} \tag{2.4}$$

where ν is Poisson's ratio and the subscripts denote the indenter (1) and sample (2) properties. Eqn. 2.3 can be rearranged into a more useful form for interpreting indentation data:

$$P = \frac{4}{3} R^{1/2} E^{*} \delta^{3/2} \tag{2.5}$$

While Hertzian theory fully describes the initial elastic deformation of a material, it is inadequate for interpreting elastic-plastic deformation. Hertzian theory was initially applied to indentation when Sneddon [75] considered the indentation of an isotropic, homogeneous material with a flat punch. This was further expanded on by Doerner and Nix [76], who observed an initial linear unloading region during nanoindentation. By assuming purely elastic deformation during initial unloading and modeling the moduli as springs in series (from Eqn 2.4), Doerner and Nix theorized that the contact area initially remained constant during unloading and thus defined the contact stiffness as

$$S = \frac{dP}{d\delta} = \frac{2}{\sqrt{\pi}} E^{*} \sqrt{A_c} \tag{2.6}$$

where A_c is the contact area. Oliver and Pharr redefined the initial unloading region as a power law rather than linear [77], giving

$$P(\delta) = \alpha(\delta - \delta_r)^m \tag{2.7}$$

where α and m are material constants, and δ_r is the residual plastic deformation after complete unloading. Figure 2.11 shows a representative load-displacement curve fitted to Eqn. 2.7.

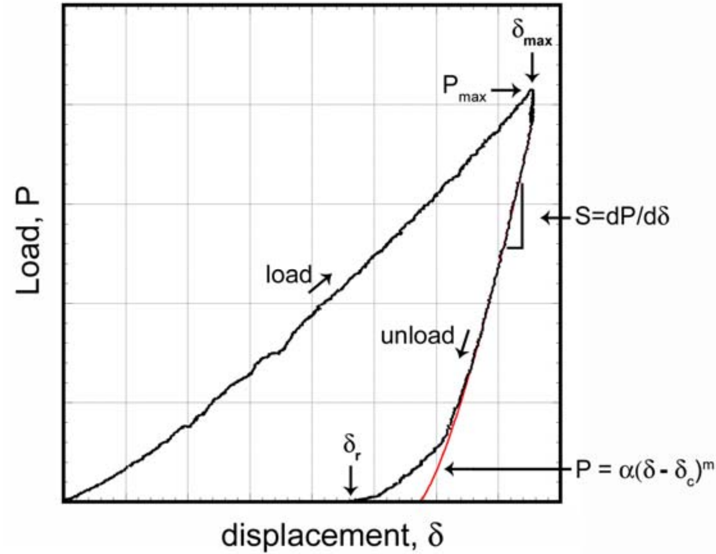

Figure 2.11 Representative load-displacement curve, showing the maximum load (P_{max}) and displacement (δ_{max}), stiffness (S), power law unloading function (red line), and the residual displacement (δ_r).

The contact area of the indenter is typically determined by the Oliver-Pharr method [77], in which a homogeneous, isotropic material with a known modulus is indented to a series of depths and Eqn. 2.6 is solved for the unknown area. Common calibration standards include fused quartz, polycarbonates, and single crystal aluminum. Indentation area as a function of depth can be fitted to a polynomial expansion of the form

$$A_c\left(\delta_c\right)^{O-P} = C_o\delta_c^2 + C_1\delta_c^1 + C_2\delta_c^{1/2} + C_3\delta_c^{1/4} + C_4\delta_c^{1/8} + \ldots + C_8\delta_c^{1/28} \qquad (2.8)$$

where A_c is the projected contact area, δ_c is the contact depth, $O\text{-}P$ signifies the Oliver and Pharr method, C_o is the ideal shape factor for indenter geometry, and $C_{1\text{-}8}$ are deviations from ideal geometry. The contact depth δ_c is given by

$$\delta_c = \delta_{\max} - \varepsilon \frac{P_{\max}}{S} \tag{2.9}$$

where ε is dependent on indenter geometry, δ_{max} is the maximum displacement, and P_{max} is the maximum load (see Figure 2.11). An alternative method for determining the contact area function was proposed by Thurn and Cook [78]. The approach uses the harmonic average of a spherical tip profile and a perfect cone profile and is given by

$$A_c(\delta_c)^{T-C} = \frac{\pi\delta_c^2}{\cot^2\alpha} + 4R\pi\delta_c + 4R^2\pi\cot^2\alpha \tag{2.10}$$

where α is the effective included half angle based on the tip geometry and R is the effective tip radius. The results in Chapters 3-5 involve both Berkovich (α =70.3°) and cube corner (α =42.28°) three-sided pyramid geometries. This method is attractive in its simplicity, in that it has only two adjustable parameters (effective tip radius and tip geometry), both of which are physically meaningful. Using either Eqn. 2.8 or 2.10, the hardness can be defined as

$$H = \frac{P_{\max}}{A_c} \quad . \tag{2.11}$$

while the elastic modulus can be determined from Eqn. 2.4 and 2.6.

Equations 2.8 and 2.10 are no longer valid for the indentation of three dimensional structures (rather than thin films) since the radius of curvature of the indenter is typically much larger than the critical dimension of the structure. For the compression of nanospheres, there are three approaches proposed by Mook et al. [45] that bound the contact area. Assuming the sphere is perfectly elastic and the radius of the indenter is large, a Hertzian solution gives

$$A_c^H = \frac{\pi \delta r_{eff}}{2} \tag{2.12}$$

where δ is the displacement, the factor of 1/2 accounts for deformation from one contact, and r_{eff} is the effective radius of curvature between the indenter and the sample calculated from Eqn. 2.2. A Hertzian contact area would be appropriate for very small displacements where minimal plasticity is assumed and represents a lower bound on the actual contact area. For larger displacements, a geometric contact can be used that assumes entirely plastic deformation and is given as

$$A_c^{geo} = \pi \left(\delta r - \frac{\delta^2}{4} \right) \quad . \tag{2.13}$$

The third approach proposed by Mook et al. [45] is for the largest displacements, where the sphere is severely deformed and becomes almost cylindrical. This assumes the load is being supported by the midplane of the sphere and uses conservation of volume to determine the cylindrical dimensions of the crushed sphere. This cylindrical contact area is

$$A_c^{cyl} = \frac{4\pi r^3}{3(2r-\delta)} \quad . \tag{2.14}$$

This represents an upper bound on the actual contact area. For the compression of nanotowers, the estimation of the contact area is more direct, as the tops of the towers are typically flat. Using either SEM or TEM *in situ* techniques, the contact area can be approximated based on the direct observations. However, both these techniques give two dimensional projections of the contact and thus include some error.

2.5.2 Nanoindentation sample preparation

Nanoindentation requires varying degrees of sample preparation depending on the specific technique being used. For standard *ex situ* nanoindentation, the most basic requirement is a relatively flat (minimal tilt) and smooth (low roughness) surface. While this is primarily important in accurately characterizing the indenter-surface contact area, a flat, smooth surface is also necessary for scanning probe type indenters (such as the Hysitron Triboindenter®) which use the diamond tip as a probe to map the surface topography. Two techniques that are discussed below are mechanical polishing and focused ion beam (FIB) milling. For electron microscopy *in situ* indentation, the sample needs to be 'visible' to the electron beam. This also requires FIB preparation to make the sample accessible to both the indenter and the e-beam.

2.5.2.1 Mechanical polishing

In the case of thin film specimens (as discussed earlier in this chapter and in Chapter 3), top-down (plan view) or cross-sectional mechanical polishing can be used to minimize the surface roughness and tilt. This involves a series of abrasive pads of decreasing grit (typically SiC) followed by colloidal solutions dispersed on felt pads (typically with Si particles, with the smallest diameter being 20 nm). Figure 2.12 shows two polishing strategies for a representative multilayer film (discussed in Chapter 3). The first example (Fig. 2.12a,c) shows standard cross-sectional polishing, where the polishing (and indentation) surface is normal to the growth direction. In the second example, the sample is tilted ~1-2° from top-down polishing, such that the polishing

and growth direction are slightly misaligned. The advantage with this type of polishing is that a much larger amount of surface is exposed for indentation. In the example shown in Fig. 2.12, the cross-sectional polishing (c) shows a film thickness of 1-2 μm while the diagonal polishing on the same sample exposes 100-120 μm. This type of polishing is particularly useful for layer-by-layer fracture analysis using indentation, since the layer thickness is often too small (and the indenter tip is too blunt) to contain an indent that generates enough stress to form cracks. Chapter 3 gives examples of indents from both types of polishing, where the cross-sectional polished surfaces were used for shallow (50-100 nm) indents probing the elastic-plastic properties and diagonal indents were used to measure fracture toughness.

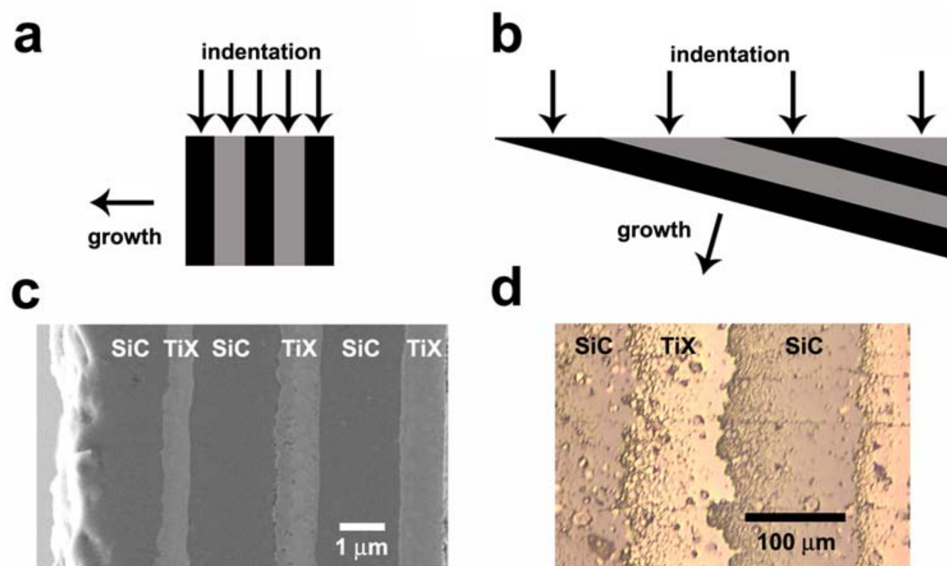

Figure 2.12 Examples of polishing strategies for multilayer films shown in schematics (a,b), SEM (c), and optical microscopy (d). Cross-sectional polishing is shown in (a,c) while diagonal polishing is shown in (b,d). Note that schematics in (a,b) show a cross-sectional view while the images in (c,d) are plan views of the indentation surface that was polished.

2.5.2.2 Focused ion beam milling

Focused ion beam (FIB) milling was used to prepare nanotower samples for both *ex situ* and *in situ* indentation. During the FIB milling, nanotower samples were tilted such that the long axis of the tower was normal to the ion beam and were milled at 30 kV and 1 nA. Figure 2.13 describes the sample preparation for *ex situ* indentation, with (a) showing a forest of towers prior to the cut and (b) showing the same region post cut. Figures 2.13c,d show the FIB milled surface at a tilt of 30° (with plan view being 0°) at two different magnifications. The region marked with a dotted line in (c) is magnified in (d), with the white arrows indicating the exposed tower core. After the

milling, the surface is relatively flat (asperities with heights <20 nm) and easily accessible by the scanning probe approach on the Triboindenter.

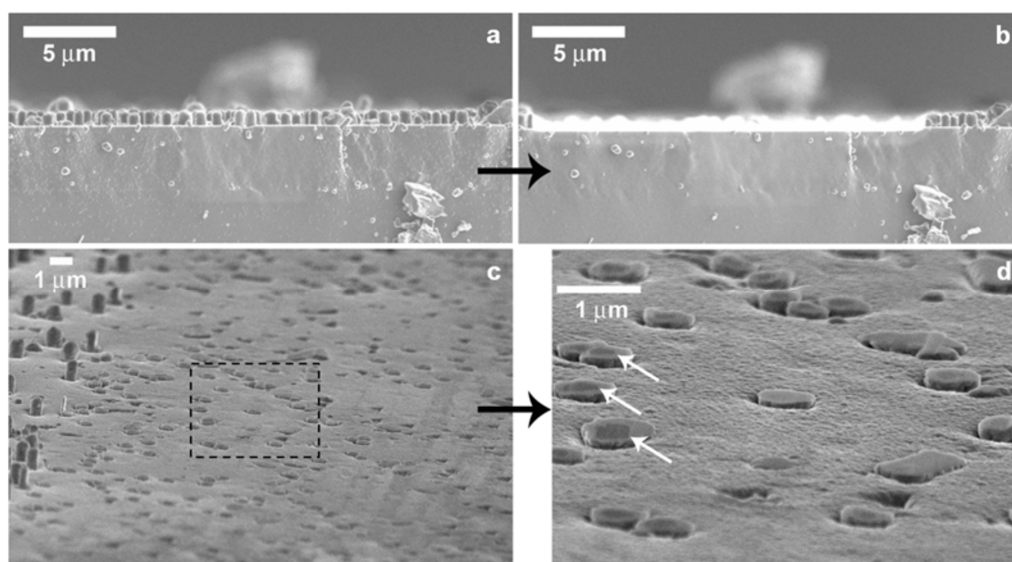

Figure 2.13 Example of FIB milling process for *ex situ* indentation. Images (a) and (b) show a cross-sectional view of the sample before (a) and after (b) milling. Images (c) and (d) show the region at 30° tilt at two different magnifications. The dotted line in (c) shows the region magnified in (d). The white arrows in (d) highlight the exposed tower cores for indentation (to be discussed in Chapter 4).

The FIB can be used in a similar way for *in situ* indentation sample preparation. This technique was used primarily with vapor-liquid-solid (VLS) grown Si nanotowers. VLS growth is discussed in more detail in Chapter 4. With these samples, instead of milling a channel flat for indentation, the FIB is used to create a single row of nanotowers with no obstructions on either side. Figure 2.14 shows an example of this, where the towers in the center (labeled with white arrows) were preserved for indentation and everything to the right and left of them was removed with the FIB. This

creates a path for the e-beam, in this case left to right across Fig. 2.14, to interact with a single tower and not be obstructed by other objects before reaching the detector. This is discussed in more detail in Section 2.5.5.

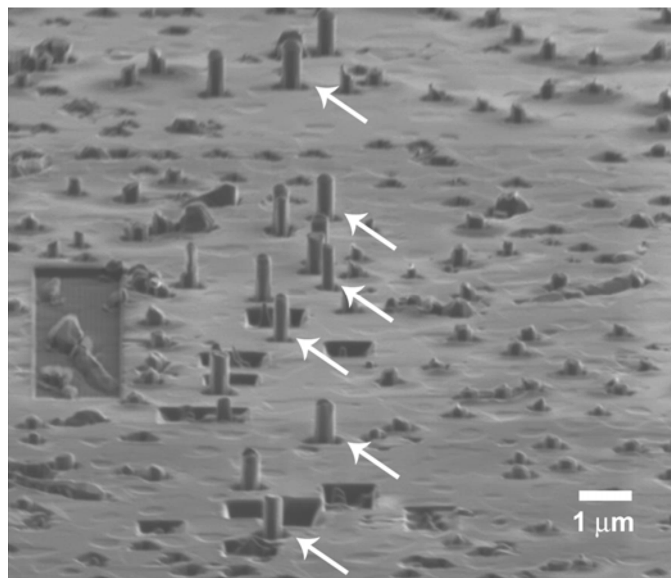

Figure 2.14 Example of FIB milling process for TEM in situ indentation. Towers were milled on the left and right side of the image, leaving stubs. Arrows indicate the row of towers in the center that have been preserved for indentation.

2.5.2.3 Nanoparticle deposition for *in situ* indentation

The Si nanoparticles used for *in situ* TEM indentation (discussed in Chapter 5) were synthesized using the HPPD system and collected with the help of L. Qi. Unlike the film growth process that occurs 2 cm downstream of the HPPD nozzle (see Section 2.3), nanoparticle samples for *in situ* indentation were collected 90 cm downstream of the nozzle using aerodynamic focusing [79]. Figure 2.15a shows an optical image of a line deposited by a focused beam of Si nanoparticles. The white line indicated with an

arrow is a thick (tens of μm's in height) deposition of particles. On either side of this line are triangular sapphire substrates (labeled with red arrows), spaced a few millimeters from the deposition line. By offsetting the substrates, the concentration of deposited nanoparticles is much lower, as schematically shown in a plan view image of the substrate with dispersed nanoparticles (colored red) in Fig. 2.15b. Figures 2.15b,c highlight how this is advantageous for *in situ* indentation. By rotating the substrate 90° into a cross-sectional view (Fig. 2.15c), the nanoparticle closest to the acute point of the triangle sits unobstructed from other particles either in front or behind it. This allows the particle to be imaged by the e-beam (traveling into the page in Fig. 2.15c) while also being accessible to the indenter (moving downward in Fig. 2.15c). TEM *in situ* indentation is discussed further in Section 2.5.5.

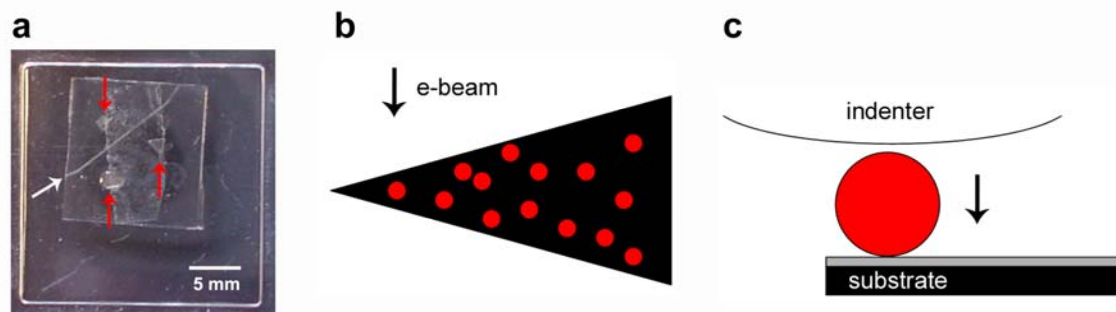

Figure 2.15 Nanoparticle deposition techniques for *in situ* indentation, showing triangular sapphire substrates (red arrows) on either side of a deposited line of nanoparticles (white arrow) in (a) and schematics of the nanoparticle (red) and substrate (black) orientation with respect to the e-beam and indenter (b,c).

2.5.3 *Ex situ* indentation

Nanoindentation was used extensively to determine the mechanical properties (modulus, hardness, fracture toughness) and deformation mechanisms in the thin film samples. The two *ex situ* indenters used were the Hysitron TriboIndenter® and MTS Nanoindenter XP®. Note that MTS sold their nanoindentation business to Agilent Technologies in June 2008.

The Hysitron TriboIndenter® consists of an optical microscope, a piezoelectric XYZ scanner, a translating stage, and a 2D transducer [80]. The TriboIndenter® uses top-down optics with a maximum resolution of 50 μm to locate areas of interest on the sample. The indentation location can be further refined using the TriboIndenter's scanner, which is controlled using piezoelectric ceramics and allows placement of indents within ± 20 nm. The scanner can also be used to image the surface topography, similar to an AFM. The resolution, however, is limited by the sharpness of the indenter tip. The indentation is performed using a high voltage, parallel plate transducer. The applied voltage is proportional to the force, with a theoretical resolution of 1 nN and 0.04 nm and a full-scale displacement of 20 μm with a maximum load of 30 mN. Indents are quasi-static and can be controlled by either a maximum load or a maximum displacement. Displacement controlled indents require tuning of the feedback control, since the displacement for a certain applied load must be compared to the setpoint and then corrected via the piezoelectric scanner.

The second type of indenter that was used is the MTS NanoIndenter XP®. The NanoIndenter XP® uses a slightly different transducer (magnetic coil) than the

TriboIndenter® and does not have an XYZ scanner. However, unlike the TriboIndenter®, the NanoIndenter XP® can perform both quasi-static and dynamic loading. In dynamic loading, a sinusoidal oscillation is superimposed on the applied load with a frequency that can be varied from 1 to 300 Hz. Dynamic loading, or continuous stiffness mode (CSM), performs a series of loading-unloading sequences and thus allows for a number of stiffness measurements from a single indent [77, 81]. This provides hardness and modulus measurements as a function of indentation depth. The NanoIndenter XP® has a theoretical resolution of 50 nN and 0.01 nm and a full-scale displacement of 500 μm with a maximum load of 500 mN.

2.5.4 SEM *in situ* indentation

The development of electron microscopy based indentation techniques is part of a trend to couple standard nanoindentation with complementary techniques to provide a better understanding of the mechanical deformation process. In addition to electron microscopy, indentation has also been combined with scanning probe microscopy (both using the diamond tip and cantilever as the probe), Raman microscopy [42], and electrical characterization [82, 83] to help understand complex deformation mechanisms that can include fracture, phase transformations, and plasticity. The advantage of electron microscopy is being able to access and image deformation events at small length scales (10 nm to 1 μm), particularly three-dimensional structures (towers, spheres, wedges, etc.). Scanning electron microscopy is well suited to probe the upper end of this range and can be used to identify both fracture and plasticity.

The experiments discussed in Chapter 4 were run using a Hysitron® SEM Picoindenter at EMPA Swiss Federal Laboratories for Material Testing and Research in collaboration with W. Mook and J. Michler. Figure 2.16 shows a series of images of the experimental setup. Samples are attached to aluminum stubs using crystal bond as an adhesive. For poorly conducting samples (including Si), edges away from the region of interest are painted with silver epoxy to provide a path for electron transfer from the sample to the grounded stub. In addition, the diamond tip is doped with boron to prevent problems caused by charging. The sample and tip are oriented such that the indentation direction is normal to the sample surface. The sample/tip unit is then tilted 75° with respect to the secondary electron detector. Typical operating conditions for the SEM are 3 kV and 7.4 mA.

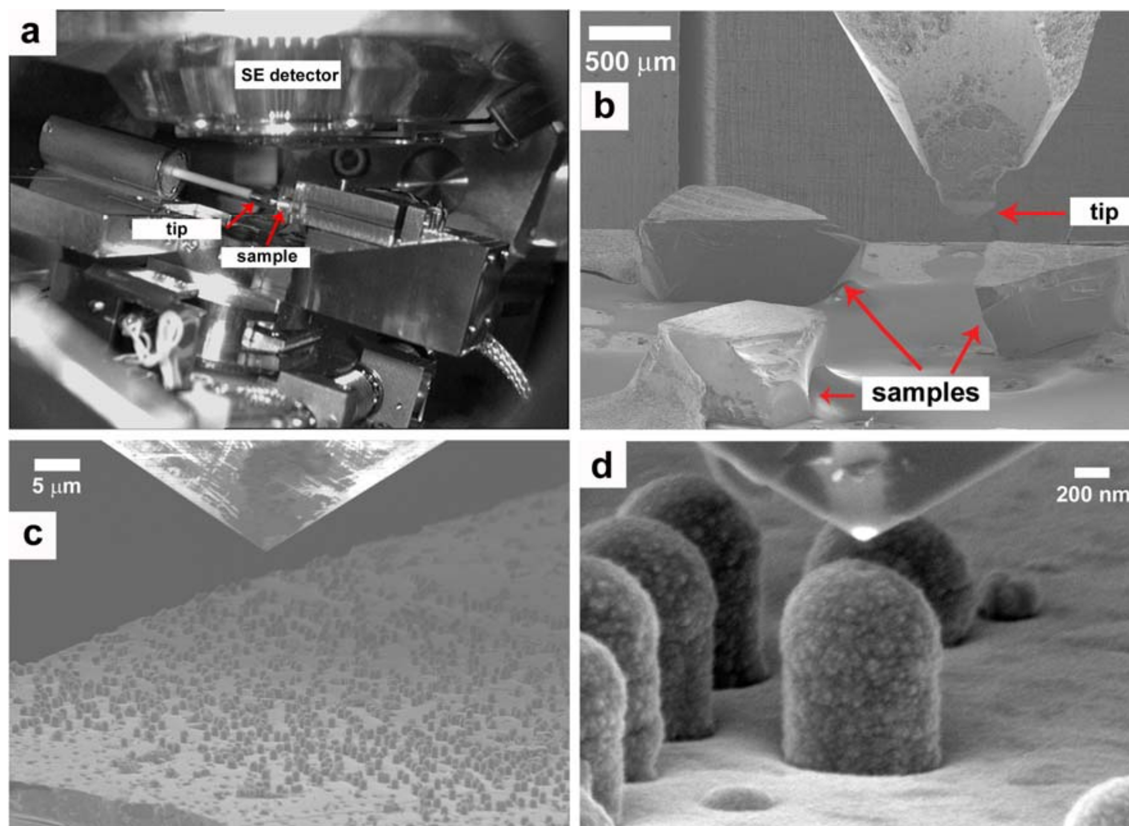

Figure 2.16 Overview of SEM *in situ* indentation showing a series of progressively more magnified images, from the a) IR camera view of the tip/sample orientation with respect to the secondary electron detector to (b-d) secondary electron images of the tip approach during an experiment.

2.5.5 TEM *in situ* indentation

TEM *in situ* nanoindentations were performed with a 120 kV FEI Tecnai T12 TEM and a Hysitron PI 95 TEM PicoIndenter®. Figure 2.17 shows the holder and the orientation of the tip-sample. The tip can be moved in three ways. First, for coarse adjustments, there are hand driven controls at the end of the holder to move the tip within 100 µm of the sample. The second are piezoceramic actuators, which enable fine adjustments of the tip in x, y, and z directions. Finally, for indentation, there is a MEMS

based transducer that drives the tip, with maximum loads of ~1.5 mN and ~5 μm of displacement. The substrates are oriented in the TEM with the top face parallel to the electron beam and the indentation direction normal to the electron beam. By sparsely depositing the Si nanoparticles near the tips of a triangular substrate (see Fig. 2.15), there is an unobstructed path for the electron beam while indenting a single nanoparticle. To minimize problems with sample charging in the TEM, sapphire substrates were typically thinned to less than 200 μm and coated with 10 nm of carbon prior to the deposition. As with the SEM indenter, the diamond tip is doped with boron to prevent charging. The nanoparticles are imaged before and after the indentation, along with 30 fps video recording during the indentation. Experiments were typically run under displacement control, with a 10 nm/s loading rate, 5 sec hold, and 10 nm/s unloading rate.

The PicoIndenter® used in this research was one of the first of its kind produced by Hysitron and thus has a number of issues that made experiments challenging. First, the MEMS design for the transducer is inseparable from the diamond tip. This makes cleaning the tip impossible, since typical procedures used for *ex situ* indentation, including sonication, would damage the MEMS transducer. Therefore, most of the material that was indented ended up sticking to the tip through van der Waals attractions after it came into contact with the tip (see edges of the indenter in Fig. 2.17). A second problem was the Berkovich tip geometry. While this is the standard geometry used in *ex situ* indentation, the displacements are much too small during *in situ* indentation to have a contact area beyond the tip rounding (in this case, r = 1.4 μm). This creates problems

with focusing (i.e., getting the tip and sample in the same plane) and accessing closely spaced structures. An ideal geometry would be flat-punch with a diameter similar to the structure of interest. A third problem was the stability of the tip during indentation due to inadequate feedback controls. This caused a sinosodial oscillation of the tip that was superimposed over the indentation loading. Examples of this problem are discussed in Chapter 5.

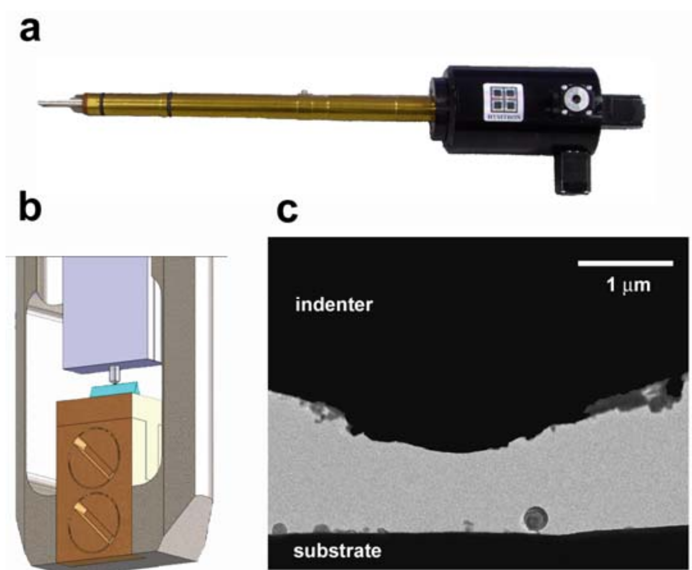

Figure 2.17 Hysitron TEM PicoIndenter holder (a), a schematic of the tip-sample orientation (b), and a TEM image of the indenter tip (r = 1.4 µm) approaching a Si nanoparticle (c). Images (a,b) were adapted from www.hysitron.com.

2.5.6 Confocal Raman microscopy

Confocal Raman microscopy (CRM) is a non-destructive technique that uses a laser to distort the electron distribution of a sample and measures the frequency of the emitted photons when the excited molecules return to a higher vibrational state. It is commonly used for compositional or crystallographic analysis [84], as the emitted

energy will be unique to the element and its local bonding. In addition, CRM is able to measure lattice strain [85] (and with elastic constants, stress), with a compressive stress causing an increase in the Raman frequency and a tensile stress causing a decrease in frequency. The relationship between peak position and strain is highly complex, but can be simplified considerably in the case of uniaxial or biaxial stress. In the current work, CRM is used to measure the CTE mismatch stress on SiC coated Si(111) nanotowers. Approximating this stress state as biaxial, the change in peak position with strain ($\Delta\omega$) in Si(111) is

$$\Delta\omega = \omega_o - \omega = 521 \cdot \varepsilon \tag{2.15}$$

where ω_o is the frequency of strain-free Si, ω is the frequency of interest, and ε is the biaxial strain [86]. The strain-free frequency for Si(111) is ~520-521 cm^{-1} and is dependent on the experimental setup (including the spectrometer calibration). The biaxial strain is related to stress through the symmetric biaxial modulus. For Si(111),

$$B_{111} = \frac{6C_{44}\left(C_{11} + 2C_{12}\right)}{C_{11} + 2C_{12} + 4C_{44}} \tag{2.16}$$

where B_{111} is the symmetric biaxial modulus and C_{ij} are the elastic stiffnesses [87]. These are given (in GPa) as C_{44} = 79.6, C_{11} = 165.7, and C_{12} = 63.9 [88]. Solving for B_{111}, the biaxial stress, σ_{xx+yy}, can be related to the change in frequency as

$$\sigma_{xx+yy} \approx 440 \cdot \Delta\omega \tag{2.17}$$

where σ_{xx+yy} [=] MPa and $\Delta\omega$ [=] cm^{-1}. In silicon, the resolution of this technique is ~0.6 cm^{-1}, or ~25 MPa [89].

The CRM measurements in the current work were run on two different experimental setups, with one at EMPA Swiss Federal Laboratories for Material Testing & Research in Thun, Switzerland (with the assistance of post doctoral researcher P. Brodard) and one at the University of Minnesota Characterization Facility. The operating conditions were similar for both, with the key differences being in the spectrometer (EMPA - Dilor XY 800, UofM – Witec UHTS300) and the magnifying objective (EMPA – Olympus 250x, UofM – Olympus 100x). In both cases, the laser beam (Ar^+ operating at 514.5 nm) was focused perpendicularly onto the (111) surface of the Si nanotowers (see Fig. 2.18b). By using a very high magnifying objective, the laser spot diameter was reduced to ~ 350 nm and positioned on individual Si nanotowers. While Fig. 2.18a is from SEM with a magnification of 5kx, it gives a sense of how the laser was positioned with the 250/100x optics. Since the penetration depth of the excitation light at 514.5 nm is 770 nm in Si [89], this effectively measures the Raman response of the Si core only, without any contribution from the underlying Si substrate. This isolation of the signal to the nanotower is shown in Chapter 4. Lattice strain in the nanotowers can be measured, as described above, by comparing the Raman peak of a nearby strain-free region on the sample with the signal from the nanotower. In both cases, the Ar laser was operated at less than 1 mW to prevent local heating (discussed below) with 2 min sampling times. Spectral data was background corrected and fit to Lorentzian functions for analysis purposes.

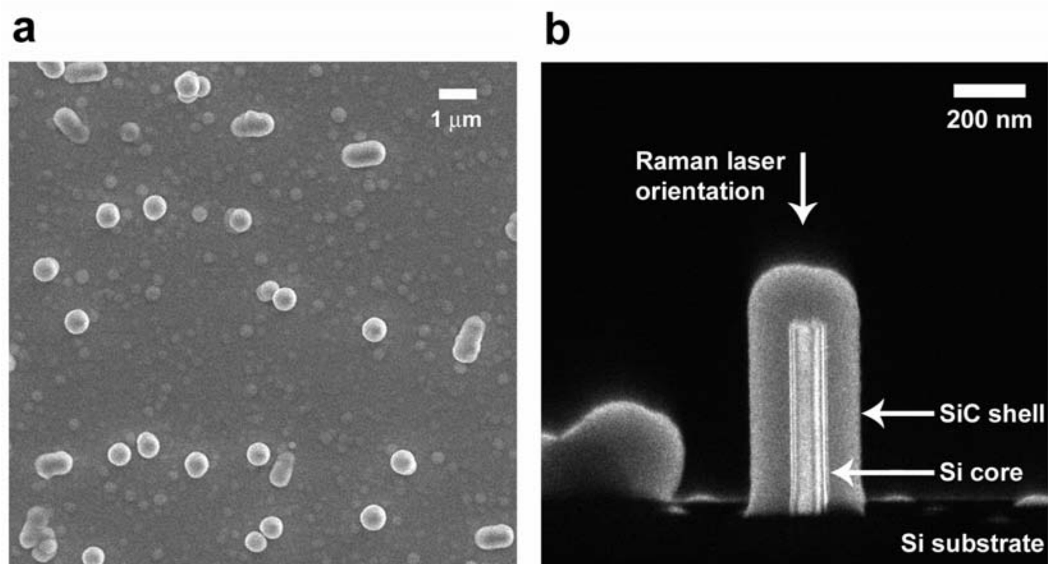

Figure 2.18 Experimental setup for the CRM measurements. (a) SEM plan view of the SiC coated Si nanotowers, where the standing (vertical) towers appear as circles. (b) dark field (DF) TEM cross-sectional view of the composite tower showing the orientation of the Raman laser.

In the current work, there are a number of complications associated with the CRM strain measurements due to the sample size. In addition to strain, local heating from the laser can cause a large shift in the peak position. While this is not an issue in bulk samples (such as wafers), laser heating in small volumes can completely overshadow any strain measurements due to high power densities and poor heat transfer [90, 91]. Figure 2.19 demonstrates this effect on the SiC coated Si nanotowers, which are the samples that are discussed in Chapter 4. Measurements were taken at 1 mW intervals starting with low power, increasing to 10 mW, and then returning to 0.5 mW. For measurements on bulk Si, the Raman shift shows no power dependence and is constant at ~520 cm^{-1}. While this verifies that the laser is focused on the Si nanotower

and not the surrounding substrate, it highlights the importance of low power levels. Thus, for the strain measurements in Chapter 4, the laser was operated at ~0.7 mW. An additional contribution to the Raman shift can be from phase transformations. This has been used extensively in characterizing phase transformed Si following indentation experiments [92, 93]. In nanowires, Si IV (wurtzite structure) has been shown to be stable for certain diameter wires, showing a characteristic peak well below Si I (~508 cm^{-1}) [94, 95]. Thus, the Raman shifts for small volumes of Si should be interpreted with caution.

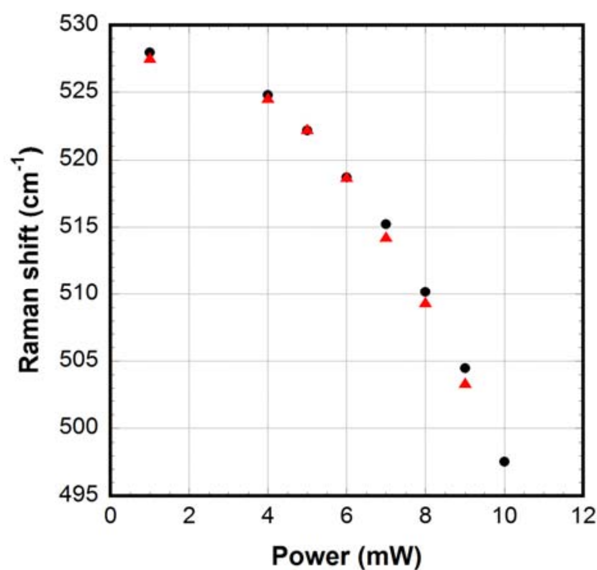

Figure 2.19 Raman shift as a function of laser power in ~120 nm (diameter) Si nanotowers coated with SiC. Black circles show increasing power while red triangles show decreasing power. See Chapter 4 for details on the sample and experimental application of the technique.

Chapter 3: SiC thin film composites

3.1 Overview

This chapter discusses the role of thermally induced residual stresses in SiC thin film systems. The first example is SiC-TiX (X includes oxide, carbide and elemental forms) multilayer composites and is adapted from a 2008 publication in Surf. Coat. Technol. [96]. These multilayers were designed to improve the wear resistance compared to SiC single layer films through mismatches in the coefficient of thermal expansion (CTE) between the layers and toughening from the more ductile TiX phase. The second example considers thin films of SiC on a variety of substrates whose CTE range from 2 – 8x10^{-6} °C^{-1}, such that the CTE mismatch between the substrate and film resulted in the film being in tension (Si), compression (Al_2O_3), or relatively neutral (Mo). This work is adapted from a presentation at the 2009 International Symposium on Plasma Chemistry (Bochum, Germany) [97]. Table 3.1 summarizes literature values for relevant materials that will be discussed in this chapter.

Table 3.1 Mechanical properties for relevant materials

property	**3C-SiC**	**Si(100)**	**SiO_2**	**Mo**	**Al_2O_3**	**Ti**	**TiC**	**TiO_2**
α (°C^{-1}) 10^{-6}	4.3-4.8	2.5	0.4	4.9	7.2-8.8	8.6	8.4	8.5
E (GPa)	395	160	72	320	380-406	116	410	170-260
H (GPa)	24-32	9	10	2.3	18-24	0.5	25	8-17
K_{Ic} (MPa·m$^{1/2}$)	3.3	0.7	0.8	8-22	2.5	103	1.7	2.8
Reference	[32, 98]	[32, 99]	[3, 6, 7]	[100, 101]	[32, 98]	[101, 102]	[98, 103]	[98, 104]

3.2 SiC-TiX multilayer composites

Multilayer films consisting of SiC and TiX alternating layers were deposited onto circular molybdenum substrates (r = 10 mm), where X is used to signify a combination of TiO_2, TiC, elemental Ti, and TiO. The deposition conditions were the same as described in Chapter 2. $SiCl_4$ and CH_4 precursors were used for the deposition of silicon carbide while $TiCl_4$ was used in the titanium deposition. Sources of oxygen and carbon in the titanium deposition are discussed in the following section. The vapor flow rates for $SiCl_4$ and $TiCl_4$ were both 40 sccm while the CH_4 flow rate was 240 sccm. Reactants for each chemical system (SiC or TiX) were injected separately for 1-4 minutes, followed by a 2-3 minute period where no reactants were introduced and the film was shuttered from exposure to the plasma flow (see Fig. 2.2). The substrate temperature was monitored throughout the deposition from a thermocouple measurement on the back of the substrate. The film growth temperature is roughly 80°C higher than the measured temperature based on a first order approximation. The measured temperature during deposition is around 1050°C for the initial layers and decreases to 880°C by the final layer due to clogging of the nucleation nozzle. While shuttered, the temperature drops to 500-600°C. Film growth rates varied from approximately 2 μm/min for the SiC system to 0.5 μm/min for the TiX system. The two representative films that are discussed consisted of six and nine alternating layers and will be referred to subsequently as F1 (six layers) and F2 (nine layers). F1 began with a TiX layer while F2 began with SiC. Layer thickness varied from 1 to 3 μm while total film thickness was approximately 8 μm for F1 and 14 μm for F2.

3.2.1 Structure and composition

As discussed in Chapter 2, films grown using the HPPD process incorporate both impacted nanoparticles and CVD growth. Evidence of both silicon and titanium nanoparticle formation has been shown using aerosol sampling measurements [70] and TEM analysis of aerodynamically focused particles [105]. Figure 3.1a shows a SEM cross sectional image from film F1. The SiC layers show distinct columnar growth, as was observed in SiC single layer films (see Fig. 2.5). This type of growth is absent in the TiX layers, which appear much more porous. Figure 3.1b shows a polished cross section of the interface between the SiC and TiX layers. The contrast in this image is due to elemental differences, as shown in corresponding EDS scans for Si and Ti in Fig. 3.1c. Given the high substrate temperatures during the deposition, interlayer diffusion between the SiC and TiX layers is to be expected.

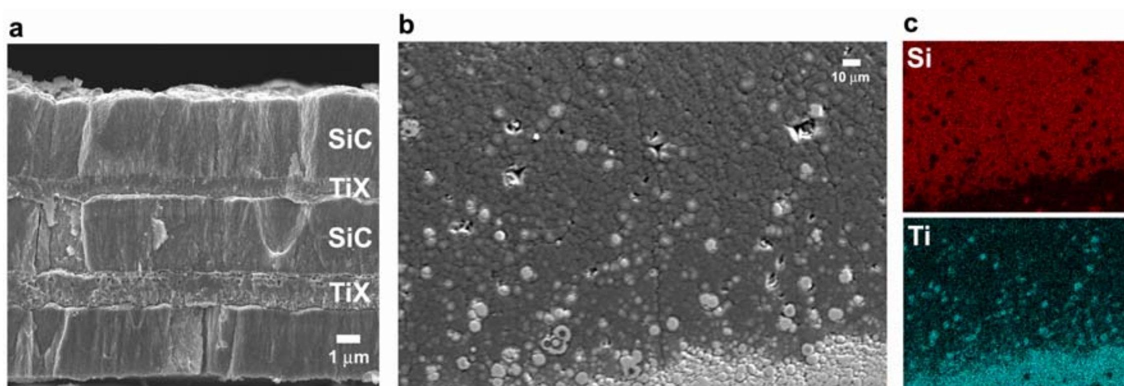

Figure 3.1 Cross sectional SEM on film F1 showing (a) columnar growth in the SiC layers, (b) higher magnification of a SiC/TiX interface, and (c) EDS data for the image in (b) showing the distribution of Ti into the SiC layer.

Scanning probe measurements were taken along a mechanically polished cross section of film F2 to illustrate changes in the growth morphology. See Chapter 2 for details on the sample preparation. Figure 3.2 shows representative images at four radial distances from the center of the substrate. The contrast is due to a height difference between the two layers, since the TiX layers will wear faster than the SiC layers during mechanical polishing. The measured layer-to-layer step height is 38.1 ± 3.8 nm as measured by tapping mode AFM. Near the center of the film (r = 1.0 mm), there is little semblance of a layered structure and large void formations (see Fig. 3.2d). Moving outward, layers become thinner and increasingly parallel to each other and the substrate. At the edge of the film (r = 8.8 mm), all nine layers of the film are visible and are relatively uniform. This radial dependence on the growth structure supports a transition in the growth process, from particle dominated growth in the center of the deposit to CVD dominated growth near the edge. This is in agreement with the HPPD film growth mechanism discussed in Section 2.3, which describes a combined particle impaction and CVD growth process that is increasingly dominated by CVD at more distant radial positions.

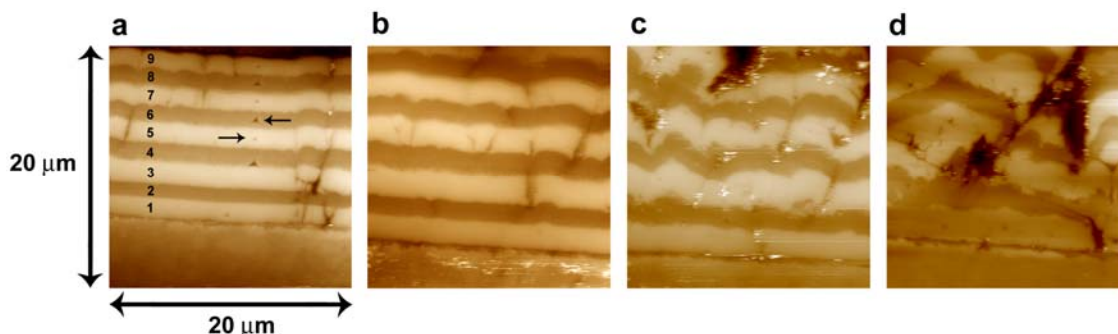

Figure 3.2 Four 20x20 μm height images of film F2 (odd layers are SiC, even are TiX) from scanning with an indenter on a Hysitron Triboindenter. The contrast range is 270 nm, with lighter regions representing higher levels. The four images are representative growth morphologies at different radial locations, with (a) being at the outer edge (*r* =8.8 mm) and (d) being the center (*r* = 1.0). The arrows in (a) show the indentation impressions.

Figure 3.3 shows high resolution XPS of the Ti 2p and Si 2p peaks from cross-sectional samples of film F2. Prior to the XPS measurements, sample cross sections were mechanically polished and then sputtered with Ar for 30 min under UHV conditions. While the specific sputter rates for SiC and TiX are unknown, the sputter rate for silicon has been measured at 2 nm/min. Titanium shows chemical shifts due to TiO_2 (37.4 at.%), TiC (29.5 at.%), elemental Ti (17.1 at.%), and TiO (15.9 at.%) while the silicon shows SiC (48.6 at.%) and SiO_2 (51.4 at.%) peaks. The formation of oxides and carbides in the titanium can be attributed to leaks in the deposition chamber vacuum and carbon diffusion from residual carbon in the chamber, respectively. In the case of silicon, the oxide is more difficult to rationalize given that the measured hardness and modulus are much closer to values expected for SiC (to be discussed in the following section). Some of the oxide (<10 at%, as measured in the SiC single layers) will be due

to leaks into the deposition chamber. The additional oxide is likely due to a shadowing effect in the SiC layers and high sensitivity of XPS to surface roughness. While the average roughness of each layer is only 3.9 $\pm$ 1.2 nm, the SiC layers will be elevated compared to neighboring TiX layers by 38.1 $\pm$ 3.8 nm after polishing. Since the position of the Ar source is fixed during sputtering, this layer-to-layer step will leave regions of the SiC sidewall shadowed and untouched by the Ar. The native oxide remaining on these surfaces would thus contribute to the high percentage of oxide present in the silicon results.

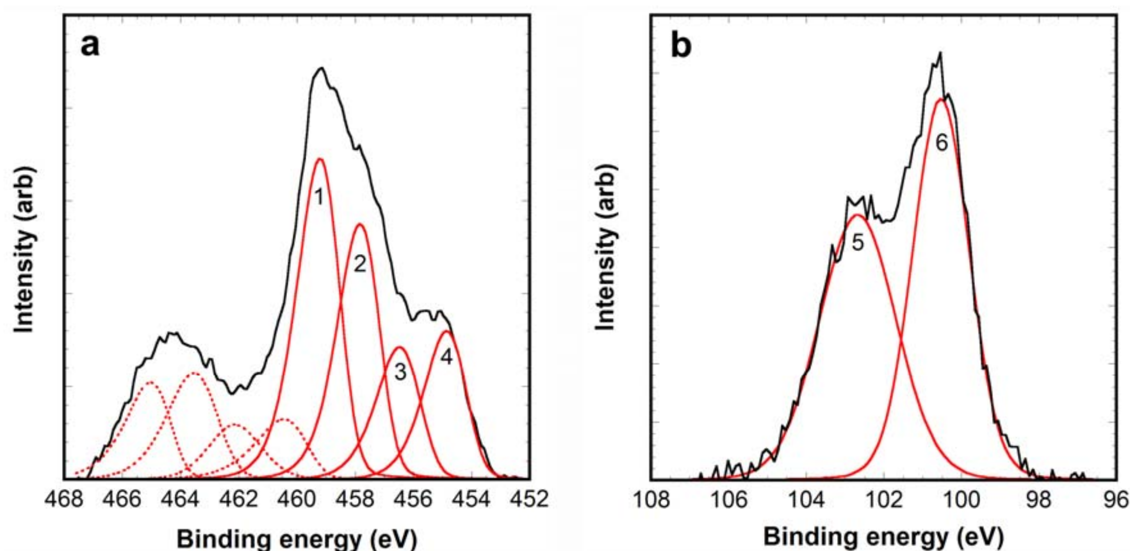

Figure 3.3 High resolution XPS scans of the Ti 2p (a) and Si 2p (b) peaks from F2. Raw data is shown in solid black lines while Gaussian curve fitting is shown in red. In the Ti spectrum (a), spin doublets are drawn with dashed lines. Peak numbers correspond to (1) TiO_2, (2) TiC, (3) TiO, (4) Ti (elemental), (5) SiO_2, and (6) SiC. Prior to measurements, surfaces were sputtered with Ar under UHV conditions to remove surface contaminants.

3.2.2 Elastic-plastic response

The indentation experiments for the multilayer films were run on the MTS NanoIndenter XP®. While the resolution (both depth and load) is not as good as for the Hysitron Triboindenter®, the NanoIndenter XP® was chosen for this work since it has a greater load capacity and uses dynamic indentation methods to measure properties as a function of depth. The films were diagonally polished to expose all of the layers and allow for indentation into each layer separately. The RMS roughness of each layer was 3.9 $\pm$ 1.2 nm as measured by tapping mode AFM. Indentations were run in open loop (no feedback control), with the maximum penetration depth, δ, limited to 20% of the layer thickness. This corresponded to depths of ~115-200 nm. Results were averaged from continuous stiffness measurements from 50 nm to the maximum depth of penetration to avoid irregularities in the tip area function at small depths. Figure 3.4 shows the modulus and hardness as a function of film layer in film F2 using both Berkovich and cube corner indenter geometries. The most striking result from these plots is the bimodal and consistent response in each set of layers (SiC, TiX). This is due to the containment of the elastic-plastic zone within each layer at the given penetration depths. Based on the Berkovich results, the average modulus and hardness for the SiC layers are 380.3 $\pm$ 17.2 GPa and 37.4 $\pm$ 3.0 GPa, respectively. For the TiX layers, the modulus and hardness are 283.6 $\pm$ 10.0 GPa and 19.4 $\pm$ 1.5 GPa, respectively. While there are a number of sources that could explain the observed increase in hardness over bulk values, the modulus should remain independent of the microstructure. The SiC layers most likely contain a small amount (much less than the 51.6% predicted by XPS)

of free Si in the form of SiO_2 since the modulus of SiO_2 is ~20% of SiC (see Table 3.1). In the case of the TiX layers, the measured concentrations are consistent with the measured modulus, assuming a simple rule of mixtures.

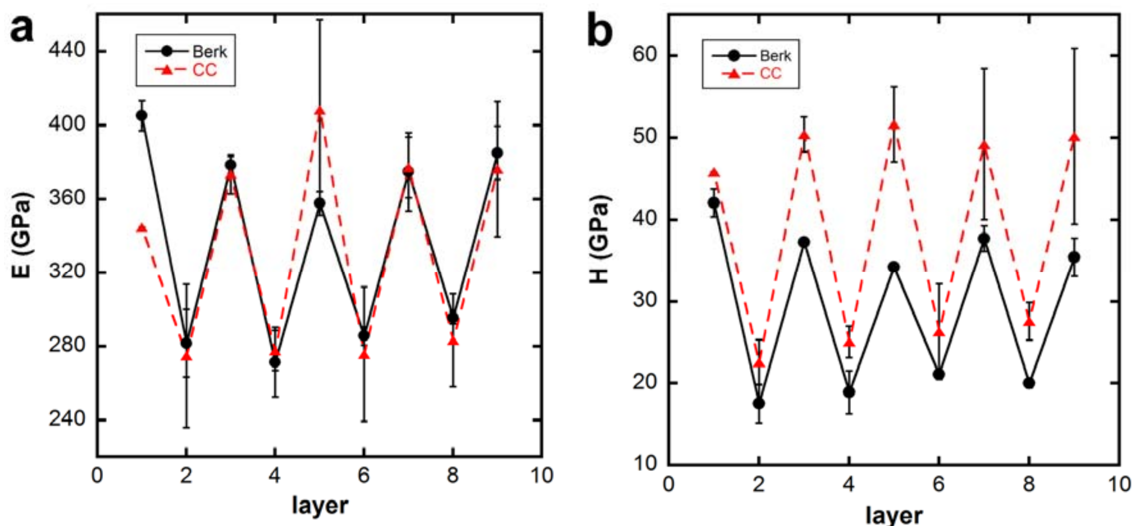

Figure 3.4 Modulus (a) and hardness (b) measured as a function of film layer on F2 (odd layers are SiC, even are TiX) using both Berkovich (Berk) and cube corner (CC) indenter geometries. Note that the film was polished at an angle, such that each layer could be indented separately.

Another important feature of Figure 3.4 is the effect of tip geometry on the measured elastic and plastic properties. With the exception of layers one and five, modulus results are consistent from both the Berkovich and cube corner tips. However, measured hardnesses with the cube corner are 5-10 GPa higher than with the Berkovich for the TiX layers and 10-15 GPa higher for the SiC layers. Chudoba et al. [106] has considered the effect of tip geometry on the measured modulus and hardness for different classes of materials. For a ceramic (Si_3N_4), they found a decrease in both

hardness and modulus when using the cube corner indenter. The cube corner indenter will generate much larger stresses than the Berkovich at the same depth due to the smaller included angle of the tip (see Chapter 2). Thus, the ceramic will fracture at more shallow depths and shows a decrease in the measured hardness and modulus. Using the same set of experimental conditions, a cemented carbide (WC-Co) showed a minimal change in the measured modulus when comparing the Berkovich to the cube corner. The measured hardness, though, increased by 20-50% for the cube corner, without explanation from the authors as to the physical origins of the increase. This increase in hardness for the WC-Co [106] and multilayer films of the current work is likely due to higher shear stresses and enhanced plasticity in the ductile phase during deformation under a cube corner indenter. This may lead to plastic pile-up around the indenter, causing an underestimate of the contact area (A_c) between the tip and sample and an overestimate of the hardness (since $H \propto A_c^{-1}$). However, there is not a significant change in the measured modulus, which should also be affected (though less so) by the contact area ($E \propto A_c^{-1/2}$).

Alternatively, the embedded TiX (see Fig. 3.1b) may be acting as a bridging interface [26], similar to Co in WC-Co [107, 108], and thus would help to inhibit crack propagation in the multilayer. Figure 3.5 shows two examples of indents into the diagonal surface of the multilayer placed near the layer interfaces. The circular contrast in the film corresponds to the TiX inclusions that were identified with EDS. In both examples, the cracks (indicated with arrows) tend towards and eventually are pinned in the TiX inclusions. This is consistent with a CTE mismatch between the TiX and SiC

leading to a hoop tension in the SiC matrix. These results suggest that the presence of the TiX inclusions enhances the ductile response of the SiC layers without significantly decreasing the hardness. However, as will be discussed in the following section, this does not translate into toughening of the multilayer film as a whole.

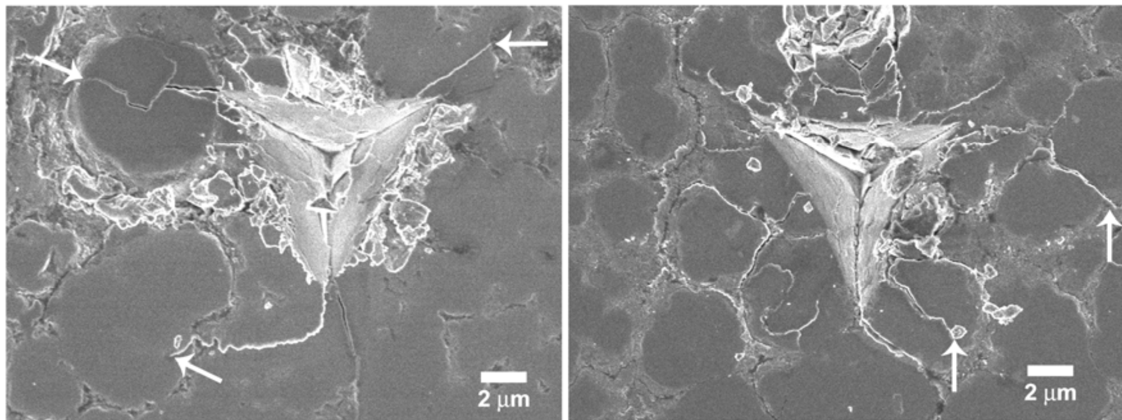

Figure 3.5 Two examples of indentations near the layer interfaces on a multilayer diagonally polished surface. Arrows indicate the end of the cracks, which arrest in the TiX inclusions (darker contrast).

3.2.3 Fracture response

Interlayer adhesion and the residual stress profile of the multilayer can be evaluated through the presence of discontinuities in the load-displacement response. Open-loop indentations were run on diagonally polished cross sections to depths that either penetrated a single or multiple layer interfaces. Figure 3.6 shows representative load-displacement (c,d) and residual impressions (a,b) for indents beginning on a SiC (a,c) or TiX (b,d) surface and penetrating multiple interfaces. The interfaces are also labeled with vertical arrows to show the relative position of the indenter with respect to

the load-displacement events. For the indents beginning with a SiC layer, only gradual decreases in the load-displacement slope are observed with decreasing depth. This is due to a relative softening as the plastic zone grows and begins to extend into the TiX layer below. In the case of the indent initiating in the TiX layer, however, displacement excursions (δ_{exc}) occur just beyond the TiX-SiC interface. A similar response was found in nine out of twelve indents beginning with TiX layers. In addition, there are also significant differences in the residual impressions (Fig. 3.6a,b). First, the size of the residual impression for the indent initiated in the SiC layer is much smaller than the indent in TiX despite similar depths of penetration. This can be accounted for in the difference in hardness of the two layers, with the SiC having nearly twice the hardness of TiX and thus able to support a larger load before yielding plastically. More interesting though, is the area surrounding the indents. For the indent that initiates in the TiX layer, there are three raised regions (labeled with white arrows in Fig. 3.6b) next to each of the faces of the indenter.

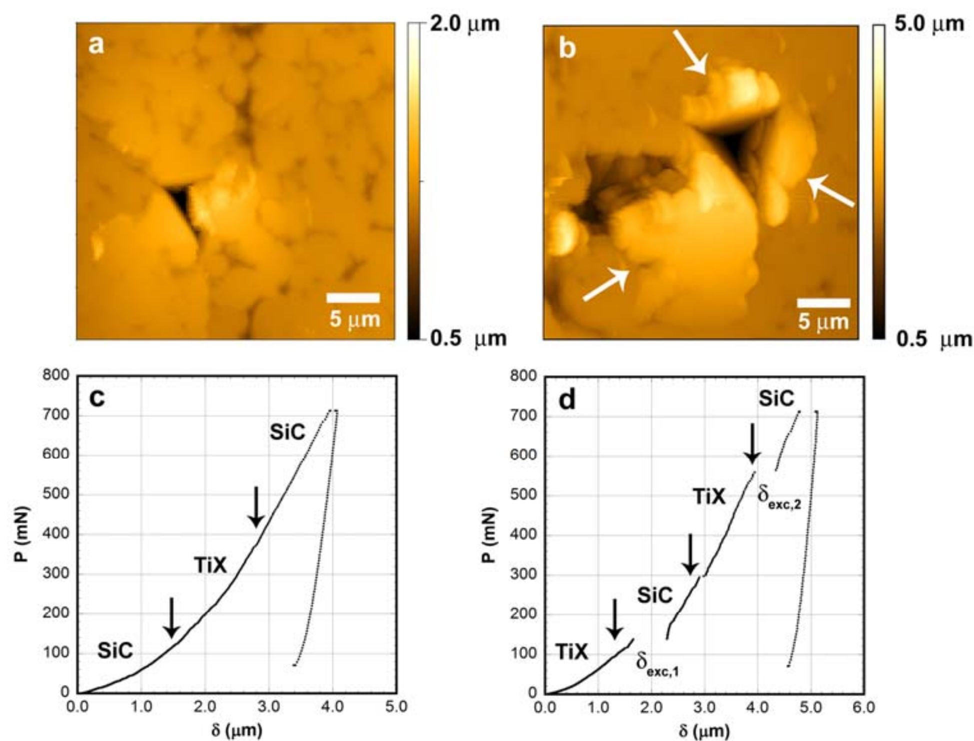

Figure 3.6 Representative load-displacement responses comparing the responses for indents initiated in (a) SiC and (b) TiX layers in F2. Vertical arrows in the load-displacement data indicate the layer interfaces. Displacement excursions are labeled as δ_{exc}. Arrows in (b) indicate the raised areas surrounding the indent impression. Note that the height scaling in (b) is three times larger than in (a).

To determine whether these height variations were the result of plastic pile-up or interlayer delamination, another series of indents was run on the surfaces beginning with the TiX layer to depths such that the indenter only crossed the first TiX-SiC interface. An example of one of these indents is shown in Figure 3.7. This indent again shows the raised region adjacent to the indenter face (a,c) and an excursion event just beyond the TiX-SiC interface (b). A FIB cross-sectional cut was made into the bottom vertex (parallel to the top face of the indenter impression), revealing the subsurface

structure of the film (Fig. 3.7d). The individual layers are labeled, along with a large horizontal crack separating the first TiX layer and the SiC layer below it. This crack is below the raised features labeled in (a,c) and shows that previously observed events (displacement excursions in the load-displacement data and raised regions in the residual impression) are primarily the result of the interlayer delamination between the TiX and SiC layers. There is also likely a contribution from plastic deformation, which would account for the difference between the size of the crack opening (Fig. 3.7d) and raised region (Fig. 3.7a). In addition to the delamination at the TiX-SiC layer, a vertical crack initiates in the SiC layer and extends into the TiX layer below (labeled with a black arrow in Fig. 3.7d). These two events can be explained through the presence of interfacial residual stresses.

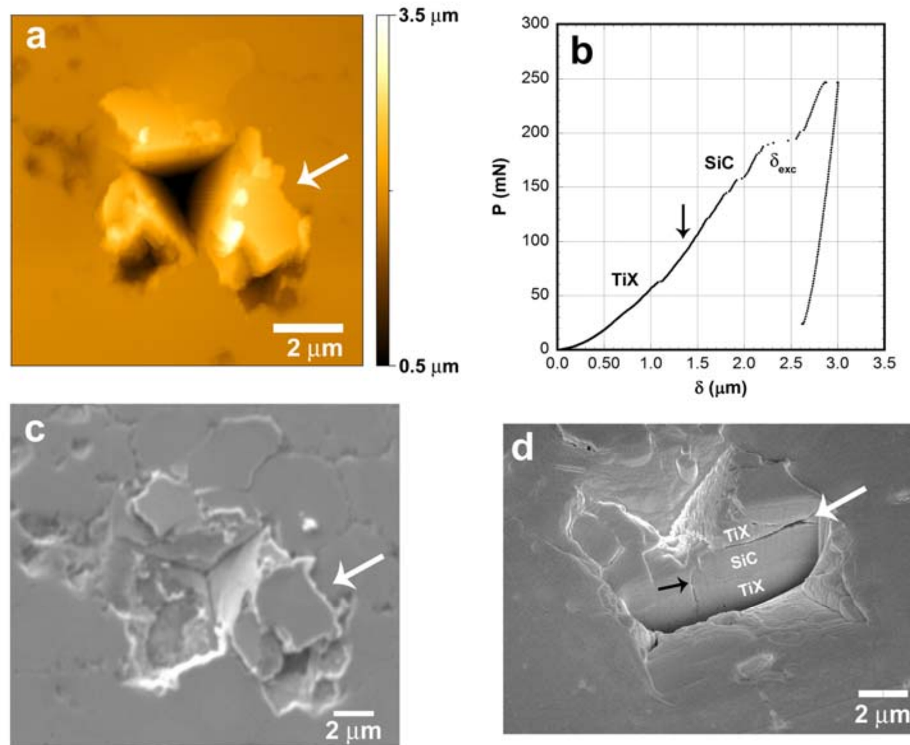

Figure 3.7 Example of a relatively shallow indentation penetrating a single interface with the first layer being TiX. The images show (a) an AFM scan of the indentation impression, (b) the load-displacement data, (c) a SEM scan of the impression, and (d) a FIB cross-section of the impression tilted to 40°. The white arrows in (a,c) point to the same raised region while the white arrow in (d) shows the presence of a horizontal crack beneath the raised region. The black arrow in (d) shows a vertical crack extending downward.

At each interface, there are stresses due to contributions from the elastic mismatch and CTE mismatch between the neighboring materials. The elastic mismatch α between layers is given as

$$\alpha = \frac{E_1 - E_2}{E_1 + E_2} \tag{3.1}$$

where E is the elastic modulus in two given layers. The residual stress due to differences in thermal expansion coefficients for thick multilayer films, σ_{th}, is

$$\sigma_{th} = E_f \left(\alpha_s - \alpha_f\right)\left(T_s - T_a\right) \tag{3.2}$$

where E_f is the modulus of the film, α_i are coefficients of thermal expansion, T_s is the substrate temperature during deposition, and T_a is the ambient temperature during testing [109]. From the indentation results in Section 3.2.2, Eqn. 3.1 gives $\alpha \sim 0.15$, suggesting that the crack motion at the interface will be controlled by the direction and magnitude of the residual stresses rather than the elastic mismatch. From Eqn. 3.2, the stress is compressive (-1.26 $\pm$ 0.01 GPa) for the SiC layers lying on top of TiX layers and tensile (0.98 $\pm$ 0.01 GPa) for the TiX on the SiC layers. Hutchinson et al. compared the fracture energies and energy release rates for two dissimilar materials that are layered to predict whether an approaching crack will penetrate the interface or run along the interface [110]. A crack approaching an interface in residual tension will become unstable and lead to debonding. However, for a compressive residual stress, the crack will penetrate the interface given a high enough residual stress and follow a stable extension. This agrees with the observed cracking at the TiX to SiC interface (tension) and the vertical crack at the SiC to TiX interface (compression) penetrating into the TiX layer below it (see Fig. 3.7d).

3.2.4 Wear resistance

The overlying goal of this work is to develop an understanding of wear at small scales and its dependency on hardness, modulus, and fracture toughness. Thus, it is

useful to consider how the properties measured with indentation translate to wear performance. One representation of wear resistance (discussed in Chapter 1) is given by Tsui et al. [15]. This uses a contact mechanics solution for a Hertzian contact (from Johnson [111]) to show that minimizing the plastic deformation (and by analogy, wear) is represented more closely by the ratio H^3/E^{*2} than hardness alone. Note the modulus here, E^*, is the reduced modulus. In the present multilayer study, this parameter was determined from the Berkovich indents. Figure 3.8 shows this ratio for the SiC (solid circles) and TiX (solid triangles) layers for the F2 film. Two quadratic trendlines are given as guides to the eye for the multilayer data (red line) and other wear resistant coatings [20] (dotted black line). While the H^3/E^{*2} ratio is much greater in the SiC layers compared with the TiX, all of the layers lie to the left of the other referenced materials included in the plot. This shift can be explained by the presence of TiX inclusions in the SiC and its toughening effects as a ductile phase. In all of the referenced nanocomposites, there are two or more phases with high hardnesses ($H > 20$ GPa), including TiB_2, TiC, TiN, and BN. All of these materials are inherently brittle and offer no additional toughening benefit when combined with a similar material as a composite. Thus, for films with an equivalent hardness, the ratio of H^3/E^{*2} suggests that the SiC layers with TiX inclusions have a much higher wear resistance than other ternary nanocomposites.

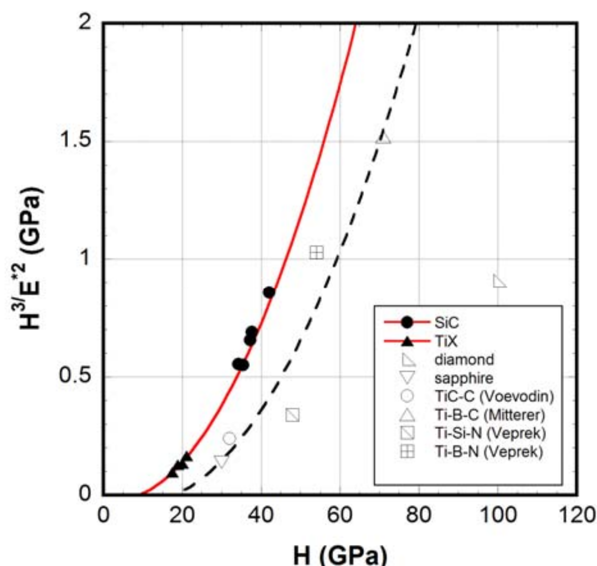

Figure 3.8 H^3/E^{*2} (where E^* is the reduced modulus) as a function of H for SiC (solid circles) and TiX (solid triangles) layers for F2 and the corresponding single layer film results. Also included are the properties of diamond, sapphire, and composite structures from Voevodin et al. [23], Mitterer et al. [112], and Veprek et al. [25, 26]. Note that the choice of these materials for a comparison was motivated by a similar plot presented by Musil et al. [20].

A more direct measure of the wear resistance of the film can be taken from scratch testing. Using the NanoIndenter XP® with a 90°, 1 μm conical diamond tip, constant-load scratch tests of 30 mN and 60 mN were run on the diagonally polished multilayer surface. Figure 3.9 shows representative wear tracks for the two loads on both the SiC (a,c) and TiX (b,d) surfaces. Note that the preferential wearing on one side of the track is due to a chip in one of the indenter faces. Comparing first the tracks for SiC to TiX at each load, the SiC shows a much more shallow depth of penetration and less wear debris along the edges. This is consistent with both the measured hardness

(H_{SiC} > H_{TiX}) and estimated wear resistance ($H^3/E^{*2}_{SiC} > H^3/E^{*2}_{TiX}$). Comparing the two applied loads, there is an increase in depth of penetration with increasing load, as expected. Finally, it is worthwhile to compare these results to similar wear testing on SiC. Bhushan et al. ran 30 mN constant load scratch tests with a 60°, 1 μm conical tip on reaction bonded SiC [113]. While the residual depth of penetration was not reported, the width of the wear track was ~2.5 μm. For the SiC wear tracks in Fig. 3.9a,c, the width of the track was ~0.8 μm for the 30 mN scratch and ~1.1 μm for the 60 mN scratch. Since the residual depth of penetration is less than 100 nm for the 60 mN scratch, the tip-surface contact is in the conical portion of the tip. This makes the difference in the tip angle (60° versus 90°) compared with Bhushan et al., inconsequential and allows for direct comparison of the track widths. The wear track in the multilayer SiC is ~1/3 of Bhushan's SiC at 30 mN and less than 1/2 the width at twice the load. Thus, the SiC multilayer (with TiX inclusions) shows improved wear resistance compared to monolithic SiC.

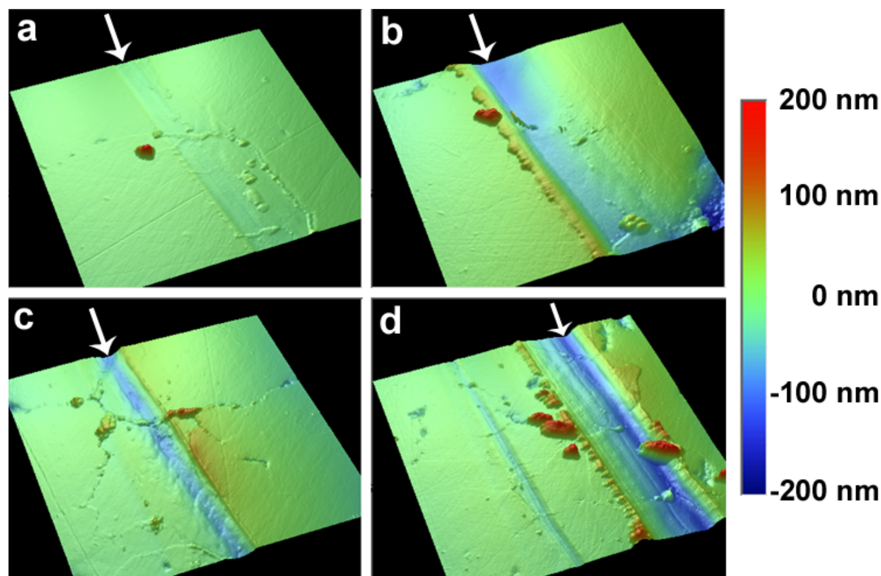

Figure 3.9 10x10 μm contact mode AFM scans of the wear tracks on SiC (a,c) and TiX (b,d) surfaces with a normal load of 30 mN (a,b) and 60 mN (c,d). Note that the images are rendered in 3D and tilted to highlight the wear tracks.

3.3 SiC thin films

To further understand the role of residual stress at a film interface, single layer SiC films were deposited onto substrates ranging in CTE from 2 – 8x10^{-6} °C^{-1}. These films were then rapid thermally annealed from 900-1200°C, resulting in the SiC film being in tension (on Si), compression (on Al_2O_3), or relatively neutral (on Mo) due to CTE mismatches with the respective substrate. Details of the RTA treatment process are given in Section 2.4. Film thicknesses were between 300-400 nm (cross sectional SEM) and found to be nominally independent of substrate. This is a much slower growth rate (30 nm/min) than reported in previously grown SiC films using HPPD (0.5-2 μm/min) (from Chapter 2) and can be explained by the radial dependence of the growth mechanism. At a radial position of 19 mm, the substrate is more than twice as far from

the center of the deposition spray as the higher rate depositions. At this position, there is equal exposure to the vapor rich boundary layer, but less of a contribution to the film structure from particle impaction due to the gas dynamics. An advantage of this radial location is a much smoother film (RMS roughness <10 nm as deposited). The grain size was measured by image processing of 500+ grains over a 1 μm^2 SEM micrograph and found to be 14.4 $\pm$ 5.1 nm. This result is confirmed qualitatively by the broadening observed in the 3C-SiC peaks (labeled 2) of a representative x-ray diffraction pattern for the SiC film on Mo (see Fig. 3.10). In addition to the 3C-SiC peaks and substrate peaks (labeled 3), there are also distinct peaks for Si. This is consistent with film depositions at locations closer to the center (see Section 2.3 and 3.2) and is most likely due to incomplete carburization of Si.

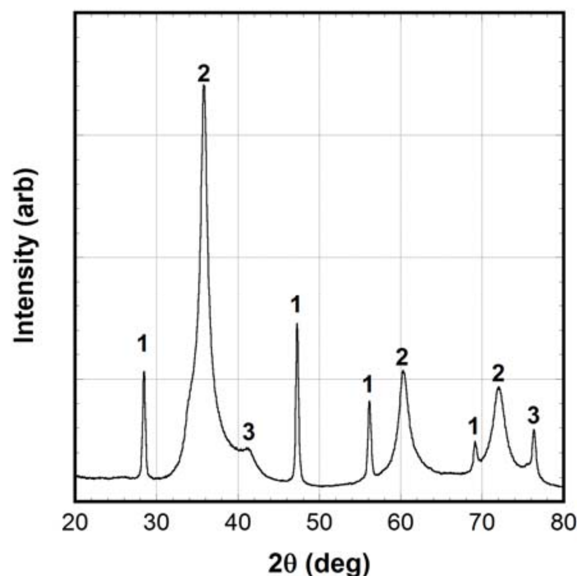

Figure 3.10 XRD pattern for a SiC film on a Mo substrate. Peaks are labeled for Si (1), 3C-SiC (2), and Mo (3).

3.3.1 Elastic-plastic response

The indentation experiments for the SiC films were run on the MTS NanoIndenter XP®. Table 3.2 summarizes the elastic modulus (*E*) and hardness (*H*) measurements for each of the substrates. These measurements were taken with a cube corner diamond indenter using open loop dynamic indentation from displacements of 50-100 nm. In the case of measured hardness, there is little variation in the result across the three substrates. The plastic zone size can be approximated by Johnson's contact mechanics modeling of indentation [111] as

$$c = \left(\frac{3P}{2\pi\sigma_{ys}} \right)^{1/2} \tag{3.3}$$

where c is the plastic zone radius, P is the applied load, and σ_{ys} is the yield strength. In this case, the yield strength is approximated as one third of the hardness [114]. Using the applied loads at 100 nm displacements, the plastic zone is 260 $\pm$ 11 nm. Thus, for 50-100 nm displacements in the 300-400 nm film, the plastic zone is contained within the film and does not reach the substrate. However, the elastic interaction zone is much larger, as evidenced by the measured modulus results tracking much more closely with the substrate modulus (given in Table 3.1).

Table 3.2 SiC film hardness (*H*) and elastic modulus (*E*) on each substrate

substrate	*H* (GPa)	*E* (GPa)
Si(100)	45.8 $\pm$ 5.0	272.5 $\pm$ 35.1
Mo	48.2 $\pm$ 3.9	340.7 $\pm$ 35.3
Al_2O_3	44.9 $\pm$ 6.2	379.1 $\pm$ 47.9

3.3.2 Fracture response

The evaluation of fracture behavior in these samples presents a number of challenges with respect to crack initiation and confinement within the film. In order to initiate cracking, there is a minimum stress that must be reached. However, even with a low angle indenter geometry such as a cube corner and a small radius of curvature, the threshold stress for cracking may be at large enough displacements that the substrate begins to influence the measured response. In addition, the crack dimensions must be sufficiently large to be accessible experimentally (SEM, AFM, etc.). Based on this second limitation, indentation depths of 200 and 400 nm were used to determine the fracture toughness. Lawn, Evans, and Marshall [115] developed a fracture toughness relationship for indentation based on elastic-plastic fracture mechanics and given as

$$K_{Ic} = \alpha \left(\frac{E}{H} \right)^{1/2} \left(\frac{P}{c^{3/2}} \right) \tag{3.4}$$

where K_{Ic} is the fracture toughness, α is an empirical term for the indenter geometry, E is the elastic modulus, H is the hardness, P is the maximum load, and c is the crack length from the center of the indenter impression. For a cube corner indenter, $\alpha = 0.04$ [116]. Due to the large depth of penetration compared to the film thickness, measured toughnesses were considered a composite property of the film-substrate system, with cracks likely extending into the substrate. The results for films treated at RTA temperatures from 900-1200° are summarized in Figure 3.11.

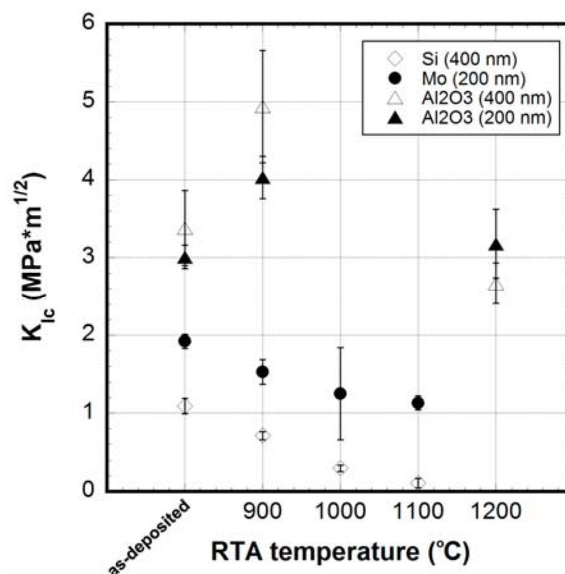

Figure 3.11 Fracture toughness for the SiC films on each substrate as a function of RTA temperature. Diamonds represent films on Si, circles for Mo, and triangles for Al_2O_3. Solid symbols are for 200 nm while open symbols are for 400 nm displacements.

While the modulus and hardness results can be explained in terms of the respective interaction zones, the fracture toughness results are less straightforward. Considering the Si substrate first, the measured toughness for SiC films decreases with increasing annealing temperature. This trend is most likely due to the CTE mismatch between the SiC film and the Si(100) substrate. From Eqn 3.2, the SiC film will be in tension after cooling. As the annealing temperature increases, the magnitude of the tensile residual stress increases and helps drive the indentation induced cracking, thus decreasing the measured toughness. Fig. 3.12 shows the SiC fracture toughness data replotted alone along with optical images of the indents at each of the RTA treatment temperatures. From the optical images in (b), the decrease in toughness is clearly demonstrated by the increasing crack length with higher RTA treatment temperatures.

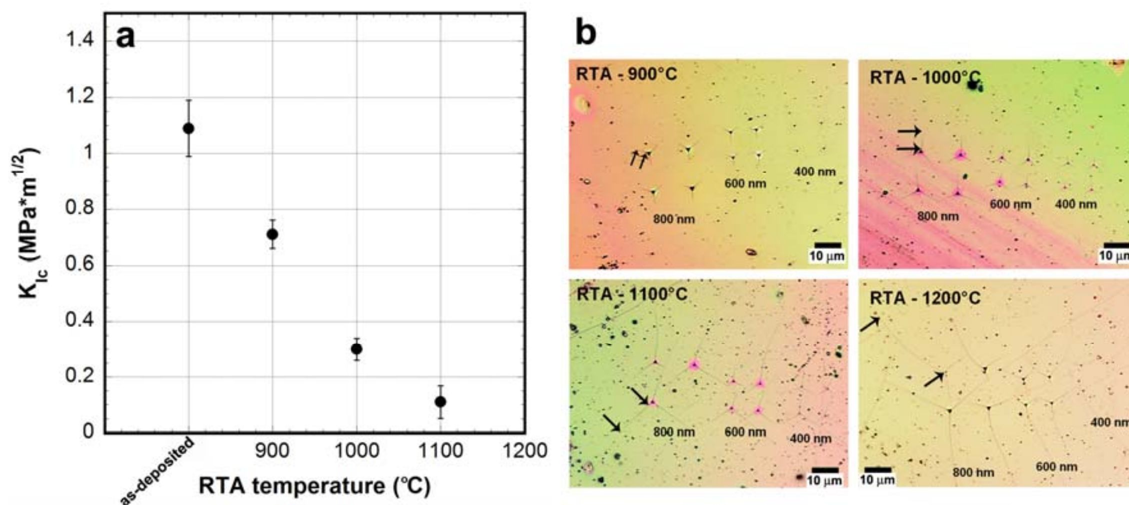

Figure 3.12 Fracture toughness as a function of RTA treatment temperature (a) along with optical images of indentations from 400-800 nm depths for SiC films on Si(100) substrates. Arrows highlight a representative crack length for a 800 nm indent for each of the RTA conditions.

Figure 3.13 shows representative images of 200 nm and 400 nm indentations into bare Si(100) and a SiC film deposited on Si. Both samples were not RTA treated. Comparing the bare Si impressions (a, c) with the SiC film (b, d), there is a distinct difference between the crack paths. The cracks in the SiC films follow a much more jagged path than those in the bare Si, due to the fine grain structure and intergranular fracture. However, the impression sizes and crack lengths are roughly the same at both indentation depths, suggesting (from Eqn 1) no improvement in toughness for the SiC film. Figure 3.14 shows a 400 nm indent into SiC on Si(100) that was FIB cross sectioned normal to one of the crack paths. Note that the top surface and cross sectional profile show the effects of ion beam damage, giving it a much smoother appearance.

Following the crack path down the film cross section, the crack clearly passes from the film (lighter layer) to the substrate (darker layer), confirming that the measured toughness is a response of the film-substrate system as a whole rather than the film alone. This explains why the toughness measurements, even without the added tensile stress from RTA treatments, never reach values measured in Chapter 2 for thicker SiC films.

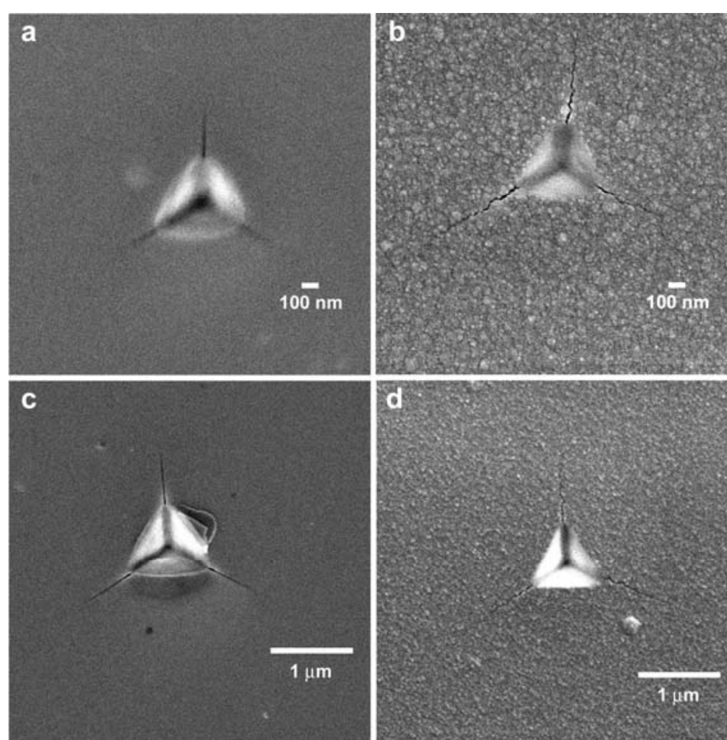

Figure 3.13 Comparison of indentation impressions in bare Si(100) (a, c) and SiC films on Si(100) (b, d) at two displacements (200 nm: a,b; 400 nm: c, d). No RTA treatment was used.

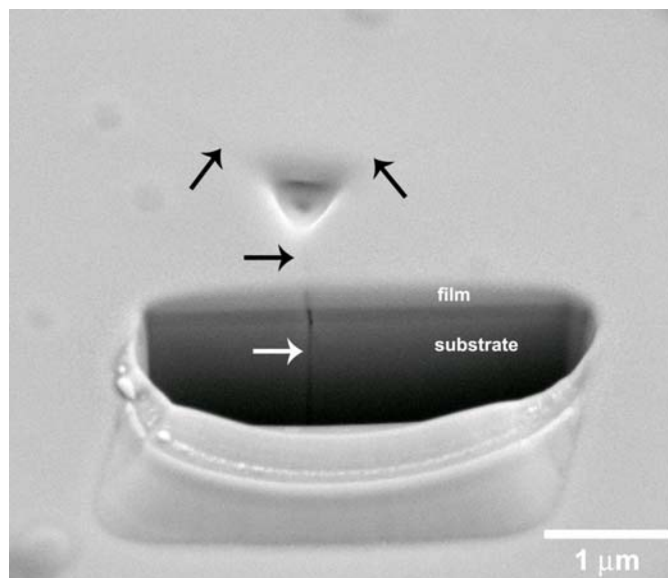

Figure 3.14 Focused ion beam milled cross section (30° tilt) of a 400 nm indent in SiC on Si(100). The black arrows show the cracks visible on the film surface while the white arrow shows a crack extending into the substrate.

For the SiC films deposited on Mo, the toughness again follows a downward trend with increasing annealing temperature. This is unexpected, since the film should be relatively neutral due to a close match of the thermal expansion coefficients (see Table 3.1). Figure 3.15 shows representative indentation impressions for an as-deposited film and films annealed at 900, 1000, and 1100°C. In addition to an increase in the crack length, there is also a substantial increase in the grain size, with the most pronounced example at 1100°C (Fig. 3.15d). While the RTA should minimize grain growth compared to conventional annealing, it is unclear why only the films on Mo showed this type of abnormal grain growth.

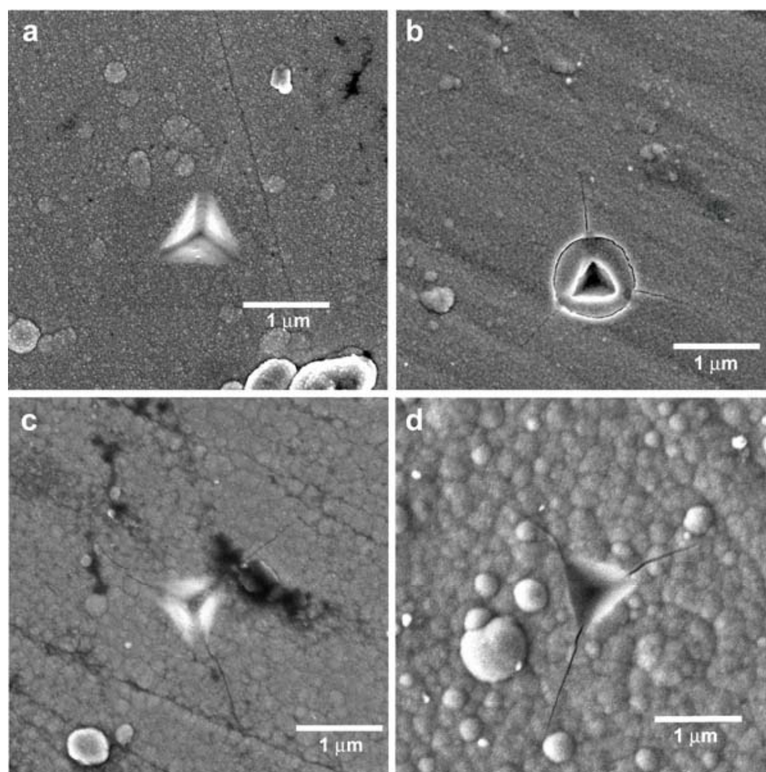

Figure 3.15 Representative indentation impressions for 400 nm displacements into SiC films deposited on Mo, showing the as-deposited film (a) and films rapidly thermally annealed to 900°C (b), 1000°C (c), and 1100°C (d).

Of additional interest with the SiC films deposited on Mo is the ring cracking observed in Fig. 3.15b. This feature was consistently observed at combinations of high loads (and depths) and low annealing temperatures. Figure 3.16 shows films annealed to 900°C and indented to depths ranging from 200 to 800 nm (a-d). In each of these cases, there is a ring that surrounds the indenter impression. One explanation of this phenomenon could be the formation of a molybdenum carbide or silicide at the substrate-film interface due to carbon diffusion from the SiC to the Mo. Diffusion of silicon and carbon in Mo has been shown to be greatly enhanced at temperatures

approaching 1200°C, with Mo acting as a gettering agent for carbon at SiC-Mo interfaces [31, 32]. Since Mo_2C is much harder (H ~ 15 GPa) than Mo (H ~ 5 GPa) [117], the film is evenly supported and deforms uniformly under the indenter load when Mo_2C is present. However, at high loads and/or low annealing temperatures, the round indenter tip (due to finite sharpness) can push the hard film into the soft substrate without initially causing crack formation. Once the indenter reaches a depth where the cube corner geometry comes in contact with the film, cracks propagate outward from the point where the sharp vertices contact the film. This leaves a circular trench from where the Mo was deformed. This explanation also agrees with the downward trend in toughness with annealing temperature (shown in Fig. 3.11), as the Mo_2C is more brittle than Mo and will increase crack growth from the film. Thus, it is the substrate hardness and carbide interlayer which dominate how the SiC on Mo responds.

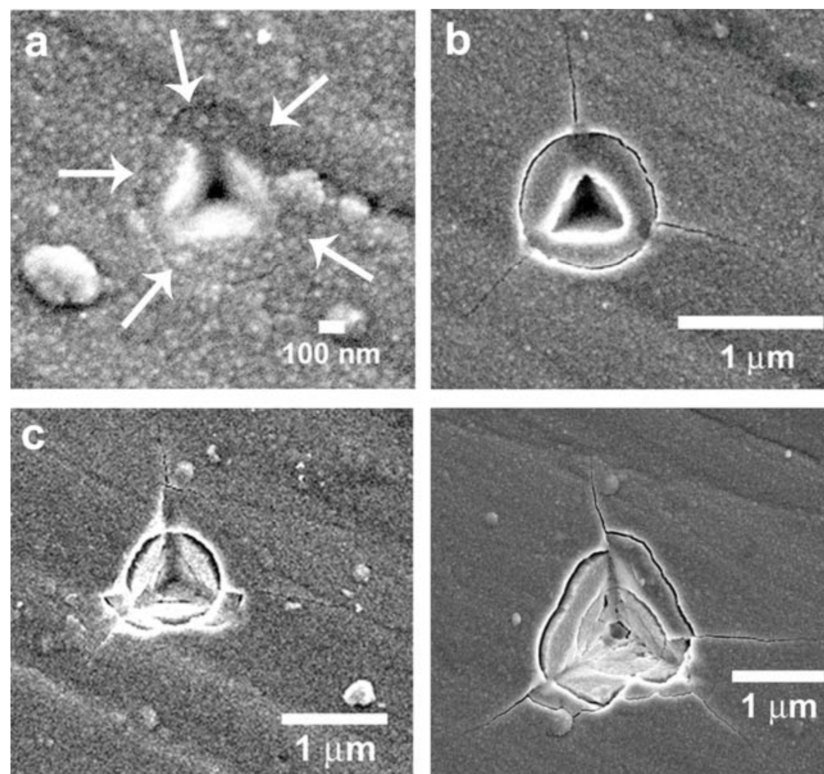

Figure 3.16 Representative indents for 900°C RTA treated SiC films on Mo at varying maximum displacements, with (a) 200 nm, (b) 400 nm, (c) 600 nm, and (d) 800 nm.

In the case of the SiC on the Al_2O_3 substrates, there is a sharp increase in toughness at an annealing temperature of 900°C followed by a decrease at 1200°C. The increase can be attributed to the thermal mismatch, as the SiC film will be in compression after deposition. At 1200°C, one possible explanation for the decrease in toughness is from creep relaxation. Assuming the film is under increasing residual compression with increasing RTA treatment temperature, creep mechanism maps assembled by Ashby et al. show that both the SiC film and Al_2O_3 substrate are in the power law creep regime for the present stress-temperature conditions [118, 119]. This

would lead to enhanced vacancy diffusion and dislocation climb, which would relieve the compressive stress in the SiC. A second explanation for the toughness decrease is unstable growth of cracks due to the thermal shock during RTA treatment. This type of abrupt drop in fracture strength has been observed in Al_2O_3 rods subjected to high thermal stresses [120, 121].

3.4 Summary

The presence of residual stresses at the TiX-SiC multilayer interfaces were shown to induce interlayer delamination at the TiX-SiC interface and layer penetration in the SiC-TiX interfaces. Both of these suggest that this structure as a whole has significant limitations as a multilayer film. Within the SiC layer, though, there is evidence from the response to cube corner indentation and crack pinning in TiX inclusions that suggests toughening in the SiC layer due to ductile phase reinforcement (similar to cemented carbides). This was shown to translate to increased wear resistance in both the ratio H^3/E^{*2} when compared to ternary ceramic nanocomposites and more directly in scratch testing when compared to monolithic SiC. In the second half of the chapter, the role of CTE mismatches was explored in a less complex system, where the substrate was varied for a SiC film such that the film was left in tension (Si), compression (Al_2O_3), or relatively neutral (Mo) after RTA heat treatments. While additional contributions from carbon diffusion (Mo) and creep (Al_2O_3) generally dominated the indentation response of the SiC film, the results for SiC on Si showed a linear decrease in toughness with

increasing RTA treatment temperature as expected for a CTE mismatch. Chapter 4 continues to explore the role of CTE mismatch stresses and how the localization of these stresses can be used to improve composite fracture toughness.

Chapter 4: Si-SiC core-shell composites

4.1 Overview

As demonstrated in Chapter 3, the presence of residual stress in the SiC thin films led to interlayer delamination (SiC-TiX multilayers) and decreased fracture toughness (SiC thin films). In each case, the coefficient of thermal expansion (CTE) mismatches generated tensile stresses that extended over the entire film surface and enhanced crack propagation. Green et al. [122] identified a variety of strategies to engineer the residual stress profiles for improved toughness, including thermal tempering, ion bombardment, surface phase transformation, chemical reactions, surface crystallization, compositional gradients, hybrid lamination, and functionally graded or layered coatings. In this chapter, the concept of layered coatings is extended to two dimensions through core-shell SiC-Si nanotowers.

4.2 Thermal residual stresses in core-shell composites due to CTE mismatch

The stresses in a Si-SiC composite structure due to elastic deformation from the CTE mismatch can be described in terms of a shrink fit pressure for a concentric cylinder [87]. Defining the Si core as having radius *b* and the SiC shell having radius *c*, the change in the interface between the two materials due to a change in temperature can be written as

$$\delta = b\left(\alpha_{SiC} - \alpha_{Si}\right)\Delta T \qquad (4.1)$$

where α are the coefficients of thermal expansion and ΔT is the temperature change from annealing. The expansion/contraction of the materials can also be written as

$$\delta = \frac{bp}{E_{SiC}}\left(\frac{b^2+c^2}{c^2-b^2}+\nu_{SiC}\right)+\frac{bp}{E_{Si}}\left(1-\nu_{Si}\right) \tag{4.2}$$

where p is the shrink fit pressure, E is the elastic modulus, and ν is Poisson's ratio. Equating (4.1) and (4.2) and solving for the shrink fit pressure,

$$p = \frac{\left(\alpha_{SiC}-\alpha_{Si}\right)\Delta T}{\frac{1}{E_{SiC}}\left(\frac{b^2+c^2}{c^2-b^2}+\nu_{SiC}\right)+\frac{1}{E_{Si}}\left(1+\nu_{Si}\right)} \tag{4.3}$$

The radial stress σ_{radial} and hoop stress σ_{hoop} are defined for the inner cylinder (Si) as

$$\begin{aligned}\sigma_{radial} &= \frac{-pc^2}{c^2-b^2}\left(1-\frac{b^2}{r^2}\right)\\ \sigma_{hoop} &= \frac{-pc^2}{c^2-b^2}\left(1+\frac{b^2}{r^2}\right)\end{aligned} \tag{4.4}$$

while the maximum shear stress is

$$\tau_{\max} = \frac{\sigma_{hoop}-\sigma_{radial}}{2} \tag{4.5}$$

Due to the singularity that arises at $r = 0$, the maximum stress in the Si core is constant and equal to $-p$, giving

$$\sigma_{radial} = \sigma_{hoop} = -p \tag{4.6}$$

The maximum radial stress in the Si tower for the deposition temperature and two annealing temperatures is given in Table 4.2, assuming a 200 nm radius Si core and 450 nm SiC shell.

Table 4.1. Maximum elastic stresses in the Si core for Si-SiC concentric cylinders

condition	temp (°C)	σ_{radial} (MPa)
as-deposited	630	-147
RTA	900	-212
	1200	-285

The results in Table 4.1 neglect contributions from the point of attachment on the substrate and from the SiC cap (see Figures 4.3 and 4.24) at the opposite end that encases the Si tower. An upper bound on the Si core stress can be established by considering a Si sphere with a SiC spherical coating. An exact solution for thermally stressed concentric spheres is given by Ferrari et al. [123]. Assuming each layer is isotropic and a homogeneous temperature variation, the radial stress in the Si tower for the deposition temperature and two annealing temperatures is given at Table 4.2, for a 200 nm radius Si core and 450 nm SiC shell.

Table 4.2. Maximum elastic stresses in the Si core for Si-SiC concentric spheres

condition	temp (°C)	σ_{radial} (MPa)
as-deposited	630	-257
RTA	900	-372
	1200	-499

4.3 Si nanotower growth and processing

Silicon nanotowers were obtained through collaborations with V. Sivakov (Max Planck Institute of Microstructure Physics, Halle, Germany) and A.V. Davydov and S. Krylyuk (NIST Metallurgy, Gaithersburg, MD). Note that in the case of V. Sivakov, while the nanotowers were grown by them, the collaboration was primarily facilitated through interactions with W.M. Mook and J. Michler (Laboratory of Mechanics of Materials and Nanostructures, EMPA Swiss Federal Laboratories for Material Testing & Research, Thun, Switzerland). Both groups used a vapor-liquid-solid (VLS) growth method, with Au catalyst particles acting as seeds for the growth of Si nanotowers on Si(111) substrates. VLS growth of whiskers and nanowires has been studied extensively, dating back to the 1960's [124]. Briefly, Au catalyst particles are first deposited on Si(111). This is most easily achieved by depositing a thin film of Au and annealing it to form Au droplets via coalescence. The substrate is then heated above the Au-Si eutectic temperature (373°C) [125] and exposed to a Si vapor source. Silicon then supersaturates the Au-Si liquid droplets, leading to precipitation of the Si at the liquid-solid interface and the anisotropic growth of Si structures. The VLS growth method can be applied to a number of standard deposition techniques. In the present case, Sivakov et al. used electron beam evaporation (EBE) [53] while Davydov et al. used chemical vapor deposition (CVD) [126]. The Si nanowires produced from these sources will subsequently be referred to as batch A (Sivakov et al.) and batch B (Davydov et al.). Figure 4.1 shows examples of each of the sets of nanowires grown.

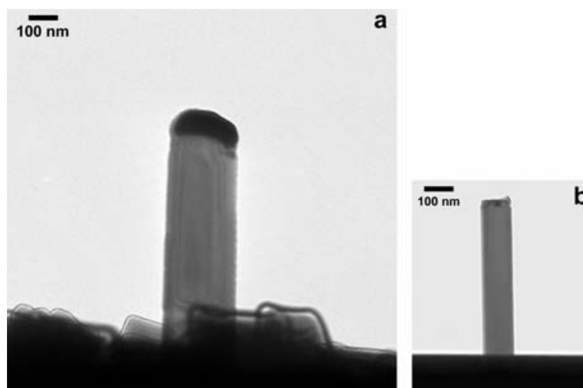

Figure 4.1 TEM micrographs of Si nanotowers grown on (111) Si substrates from a) batch A and b) batch B. Note that these nanotowers were imaged in their as-grown state, attached to the substrate.

One of the major limitations of VLS processing is contamination of the nanowires from the catalyst material. In the case of an Au catalyst in Si nanowire growth, residual Au can degrade the performance of nanowires in electronic devices [127]. This is most evident at the top of the nanowires, where catalyst particles remain as a cap. In Figure 4.1a, the Au catalyst is seen as the darker contrast material at the top of the tower. The caps can be removed through chemical etching, as shown in Figure 4.1b, where the nanotowers were treated in a KI/I_2 solution. However, there are also smaller particles, typically 1-2 nm in diameter, that decorate the sidewalls of the nanowires [8, 9]. Some of this material remains alloyed to the Si and is protected from the KI/I_2 etch by the native oxide on the Si. To remove this source of Au, the SiO_2 needs to be removed first and then treated with KI/I_2. Figure 4.2 shows an example of this 2-step etch process, where HF solution was used to remove the SiO_2. Prior to etching (Figure 4.2a), the Au cap is observed as the lighter contrast material at the top of the

tower. The etching process removes the cap, but also leads to extensive porosity, both in the tower and on the Si substrate (see Figure 4.2b). This can be explained by the presence of embedded Au nanoparticles on both the substrate and tower sides that are attacked by the etchants. Thus, while the 2-step etching process is much more thorough at removing the Au, the resulting porosity precludes towers processed in this way from further mechanical analysis. Therefore, in the following sections, two sets of nanotowers are discussed: 1) batch A, with no etching (as shown in Figure 4.1a) and 2) batch B, with only a KI/I_2 etch (as shown in Figure 4.1b).

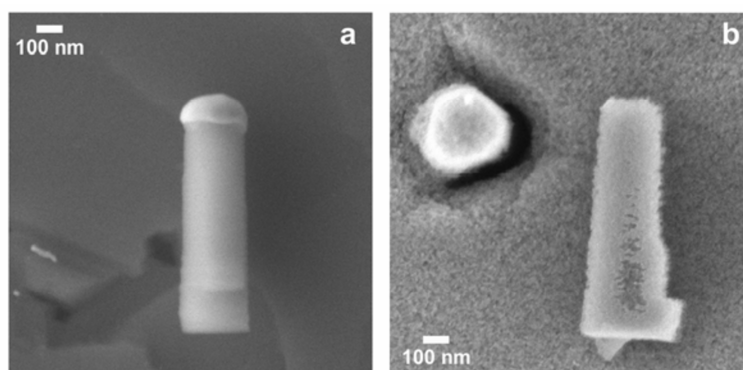

Figure 4.2 SEM micrograph of Si nanotowers from batch A a) as grown and b) after the 2-step etching process (HF, KI/I_2). In both images, the towers are lying horizontal on the Si substrate. Note that towers shown in a, b are not the same tower.

4.4 Deposition of SiC coatings on Si nanotowers with Au caps (batch A)

Deposition conditions (plasma power, vacuum level, flow rates, etc.) for the SiC coating process were the same as the thin films described in Chapter 3. The Si substrates with the nanotowers were clamped in the holder described in Section 2.2, with a nominal radial distance from the center streamline of 19 mm. The substrate

temperature was 450-550°C, as measured from a thermocouple in contact with the backside of the substrate. Deposition times were held constant at 10 min, with SiC film thicknesses ranging from 300-400 nm. Figure 4.3 shows an example of the batch A towers, before (a) and after (b) the deposition of the SiC coating.

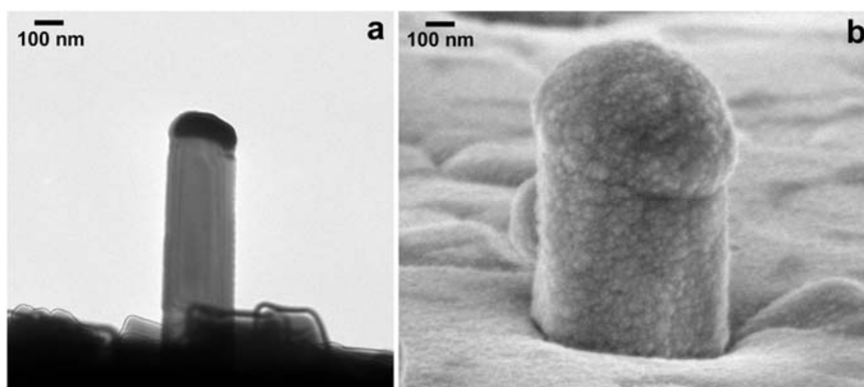

Figure 4.3 Examples of Si nanotowers from batch A a) before (TEM) and b) after deposition of the SiC coating (SEM, 30° tilt).

Cross sectional analysis of the composite structure was investigated through focused ion beam (FIB) milling of the towers. The details of the sample preparation are given in Chapter 2. Figures 4.4a,b show the FIB milled surface at a tilt of 30° (with plan view being 0°) at two different magnifications. The region marked with a dotted line in (a) is magnified in (b), with the contrast difference between the tower core and shell identified with white arrows. Note that the material surrounding the towers is the SiC film. Since it is unclear from the perspective in Figure 4.4 a,b whether the contrast is due to a difference in Z (composition) or height, the tower cross sections were imaged

in plan view at higher magnification and analyzed with energy dispersive x-ray spectroscopy (EDS) (see Figure 4.5).

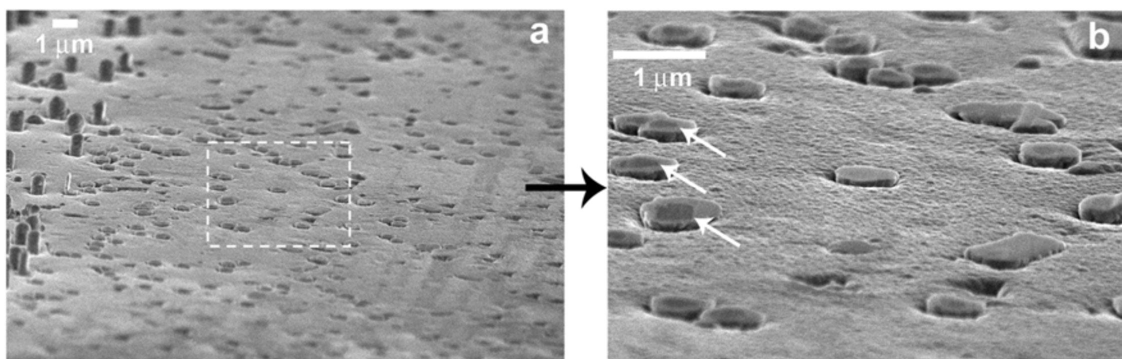

Figure 4.4 Milled surface at 30° tilt at two different magnifications for cross sectional analysis. The dotted line in (a) shows the region magnified in (b). The white arrows in (b) highlight examples of the core-shell contrast in the tower structure.

Figure 4.5 reveals a number of details regarding the structure of the composite tower. First, there is a distinct white outline of the Si core (labeled with a white arrow), highlighting the expected hexagonally faceted structure for VLS grown Si [9, 10]. While the contrast difference between the core and shell is not as distinct as in Fig. 4.4b, a compositional difference between a SiC shell to Si core is supported by the EDS line scan along the tower cross section. The line scan shows a carbon deficiency in the core, with the oxygen signal given as a reference. Figure 4.5c shows a cross section along the axial direction. Comparing the cross-sectioned images in (a) and (c), the white interfacial contrast is shown to extend along the length of the tower. While there were no additional peaks in the EDS spectrum corresponding to this region, it is likely gold

from the VLS growth process that does not produce enough signal to be identified by EDS. The role of gold in the composite structure is discussed in more detail below.

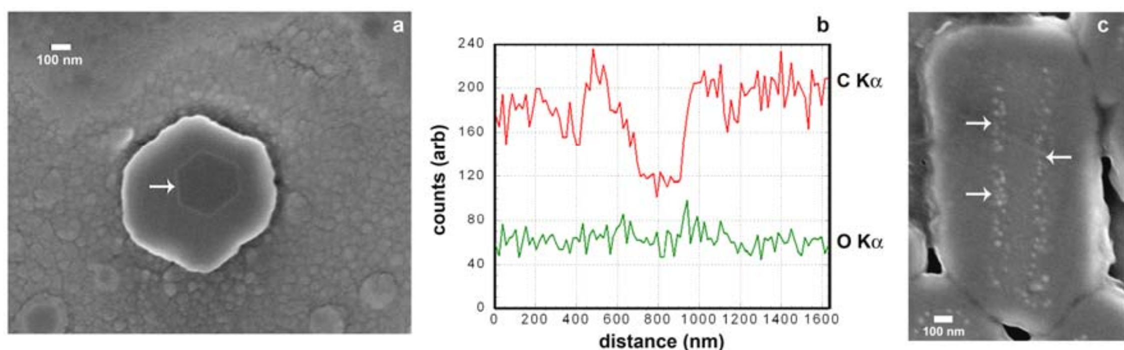

Figure 4.5 FIB cross-sectioned images of the composite tower structure in a) plan view with b) the accompanying EDS line scan across the tower showing the C Kα and O Kα intensities. Image (c) is a cross-section along the tower's long axis. The white arrows in a,c identify the interface between the shell and core.

Following the FIB cross sectioning, the composite tower samples were then RTA treated under identical conditions used for the thin films in Chapter 3. While the initial goal of this study was to measure the magnitude of the thermal residual stress on the Si core, the presence of contamination due to the Au catalyst became problematic. Figure 4.6 shows four representative towers annealed to between 900-1200°C (a-d, respectively) in their before (top) and after (bottom) condition. The only noticeable change to the tower annealed at 900°C (Fig. 4.6a) is a contraction of the tower, from a outer diameter of 908 to 826 nm, representing a strain of 9%. Beginning at 1000°C, white spots appear in the core region after the annealing process. As the annealing temperature is increased further, the tower core begins to show significant porosity. At

1200°C, in addition to a large void where the core used to be, there are small particles that cover both the tower and surrounding film.

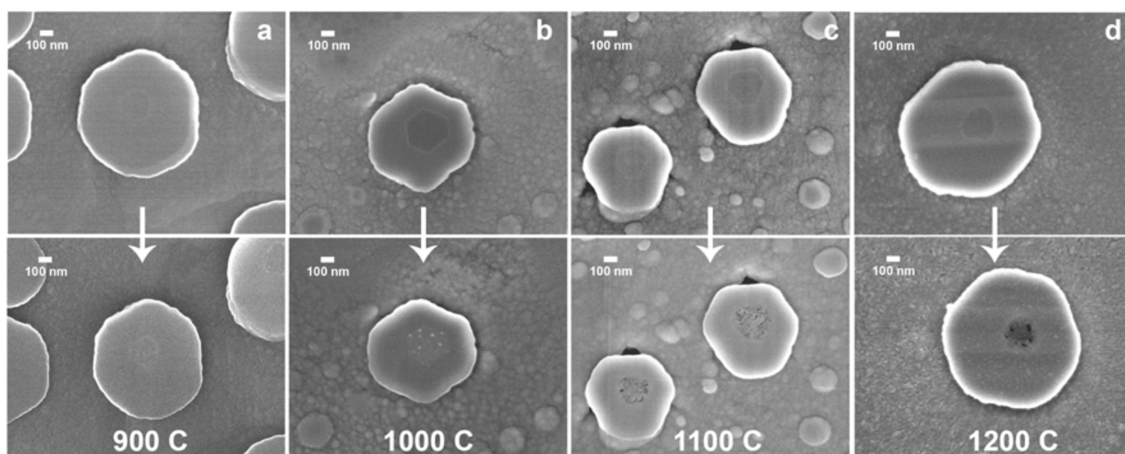

Figure 4.6 SEM imaging of representative batch A composite towers annealed to between 900 and 1200°C (a-d) in their before (top) and after (bottom) condition.

The same set of towers were also imaged with contact mode AFM to measure topographic changes, particularly in the height of the core, as shown in Fig. 4.7. Deflection images are shown to better highlight smaller features that are less visible in the height image. The height of the core above the shell is labeled at the top of the towers annealed at 900 and 1000°C. As the annealing temperature is increased from 900 to 1000°C, the height of the core above the shell more than triples. This can be explained through the compressive CTE mismatch stress and subsequent creep of the Si at high temperature. This phenomenon is discussed in more detail in later sections. At 1100°C, the raised core is replaced by voids, confirming the observation from SEM (Fig. 4.6c, after). At 1200°C, the loose particles covering the surface (as seen in Fig.

4.6d, after) caused too much noise in the AFM imaging and thus is excluded from Fig. 4.7. Of additional interest is a comparison of high contrast (white) features in SEM with their corresponding height data from AFM. First, the white ring at the core-shell interface that is seen quite clearly in Fig. 4.6b, before (and less so in Fig. 4.6a, c before), has no corresponding height feature in the AFM data. This suggests the SEM contrast is due to compositional differences rather than height. However, in comparing the white spots in the core that were observed Fig. 4.6b, after, each of the spots can be matched to a raised region in the AFM data, suggesting that SEM contrast is due at least in part to a height differential.

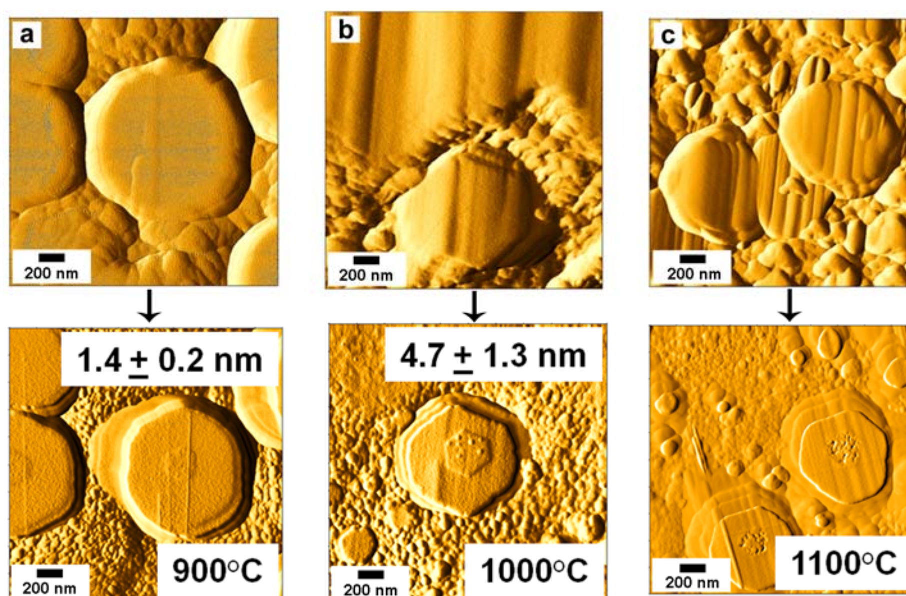

Figure 4.7 AFM deflection images of representative batch A composite towers annealed to between 900 and 1100°C (a-c) in their before (top) and after (bottom) condition. In the after images for 900 and 1000°C, the height of the core above the surrounding shell is indicated at the top of the figure. Note that the parallel vertical lines visible in a few of the images are scars from the FIB cutting process.

The changes in the tower microstructure due to annealing can be understood through the migration of Au in Si, both on the surface and in the bulk. As described earlier, there are two sources of Au in the Si towers: large catalyst droplets at the top of the tower and nanoparticles coating the tower walls. During the deposition of the SiC coating, the substrate temperature (~650°C) is high enough to enable rapid surface diffusion of the Au. Studies at similar temperatures have shown Ostwald ripening of catalyst droplets [128] and the agglomeration of Au nanoparticles on the walls of nanowires [129]. Thus, the core-shell interface after the deposition of SiC film is likely either coated with an Au thin film or agglomerated nanoparticles of Au. This would support the observation of the white ring at the core-shell interface in cross-sectional SEM imaging (see Figure 4.5a). It is unclear whether the catalyst droplet at the top of the tower remains in tact during the deposition. While these towers were too thick for TEM imaging, results in the following sections regarding batch B will show how dark field TEM was used to confirm the as-deposited structure in thinner towers.

The possible presence of Au in the bulk and its transport during annealing is more difficult to explain due to the low solubility of Au in Si [130]. Au impurities in VLS grown Si nanowires are generally thought to reside on the sides of the wires. However, recent scanning transmission electron microscopy (STEM) analysis has shown both substitutional and interstitial Au defects in Si nanowires [127, 131]. Au diffuses in Si via the kick-out mechanism, where Au atoms diffuse to interstitial sites in Si, followed by the interchange of Au and Si to substitutional sites, and then finally the kick-out of the self-interstitials [132]. In the case of defect free Si, the Si interstitials

diffuse to a free surface. In the present study, this leads to a net motion diagonally upward as Au diffuses into the Si core and then Si interstitials are kicked to the FIB-cut free surface. Considering the white/raised regions observed at 1000°C (Figures 4.6b, 4.7b, respectively) as a result of the Si interstitial kick-out, there should be an equivalent volume of Au embedded in the Si core. Approximating these features as spherical inclusions, a concentration of $4.2*10^{21}$ Au/cm^3 (or $4.2*10^{-2}$ Au atoms per Si atom) is found in the Si core. While this is four orders of magnitude larger than the equilibrium solubility limit at even the highest annealing temperature [130], the use of RTA treatments likely leads to highly nonequilibrium Au concentrations in the towers. In addition, supersaturated Au concentrations in Si nanowires have been estimated using STEM in the range of 10^{17}-10^{18} Au atoms/cm^3 for wires grown at 450°C and 10^{20} Au atoms/cm^3 for wires grown at 500°C [131]. Considering that the annealing temperatures in the current study are approximately two times higher, the estimated concentration of ~10^{21} Au/cm^3 is not unreasonable. As the RTA temperature is increased to 1100°C and 1200°C, the driving force for Si surface kick-out increases, likely causing the rapid diffusion outward of Si from the tower free surface and the formation of voids in the core region of the composite.

4.5 Indentation of batch A composite towers

The composite towers were indented both in the as deposited state and after the SiC caps were removed via FIB processing. The feedback response of the scanning probe imaging used by the Triboindenter is unable to trace a surface with large changes

in height. This makes locating the towers and aligning the indenter on an individual tower impossible. By FIB milling the surface as shown in Figure 4.4 such that the towers are in-plane with the surrounding film, the indenter can scan the relatively flat surface and locate individual towers. This process provides an additional benefit, in that it exposes the Si core and allows for probing of the confined Si core. This proved to be useful in studying crack propagation within the core-shell structure and pressure effects on the Si. The towers were also indented using *in situ* SEM indentation. The *in situ* indents related more directly to the core-shell composite response, especially with respect to fracture response and the role of compressive stresses within the Si core.

4.5.1 Elastic-plastic response of the FIB milled towers

Using a Hysitron Triboindenter with a cube corner tip (r = 120 nm), individual FIB milled towers were initially indented to shallow depths to avoid fracture. Indents were run in displacement control, with displacement rates of 2-5 nm/s that varied based on the total displacement. Holds (constant displacement) of 5 s were used after the peak displacement was reached and midway through the unloading to monitor drift. In each case, the indenter was aligned with the Si tower core. Figure 4.8a summarizes the measured hardness for the FIB milled towers as a function of tower diameter. In addition to the tower data, there are straight lines indicating the average hardness for both the SiC film (without towers) and Si(111) substrate (with no SiC film or towers). The depth of indentation was varied such that the contact area of the indenter was confined to the Si core. However, the plastic zone, as approximated by Eqn. 3.3, was

found to extend up to and beyond the tower diameter for given indents. Thus, the measured properties account for both the highly compressed Si core and the surrounding SiC shell. This is illustrated in Figure 4.8b, where the hardness is plotted as a function of the ratio of tower diameter to plastic zone diameter. For ratios up to ~0.5, the measured hardness is close to that of Si since the interaction volume of the indenter is likely confined to the Si core. As the ratio is increased to one, the hardness increases towards the value measured for the SiC film without towers. With further increases, the hardness drops off, likely due to additional yielding as the composite tower expands into the free space between the tower and the surrounding film (as shown in Figure 4.4, 4.6).

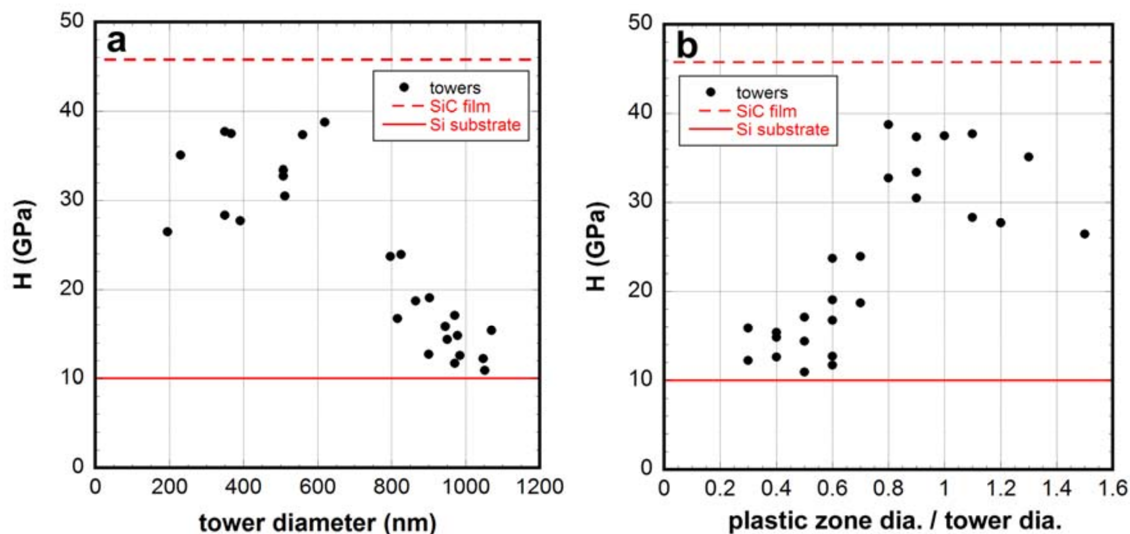

Figure 4.8 Hardness as a function of (a) tower diameter and (b) the ratio of plastic to tower diameters for FIB milled towers. The red lines indicate the average hardness for the SiC film (without towers) and the Si(111) substrate (without the SiC film or towers).

Similar to the hardness results, the elastic modulus for the larger diameter towers is quite close to the average values for Si substrate (see Figure 4.9a). For the smaller diameters, there is a gradual increase in the measured modulus. In addition to the contributions of the SiC shell, there is also a contribution from the compressive stress on the Si core. This can be described by a linear relationship developed by Murnaghan [133] that accounts for changes in elastic constants under a hydrostatic stress by knowing the zero pressure modulus and first pressure derivative of the elastic modulus. Mook et al. [45] determined a Murnaghan type relationship for the uniaxial compression of Si nanospheres as

$$E_{Si} = 160 + 6.67\bar{\sigma} \tag{4.7}$$

where E_{Si} is the zero pressure modulus of Si and $\bar{\sigma}$ is the average contact stress from indentation (both in units of GPa). Taking the average contact stress as the indentation hardness, Figure 4.9b shows the elastic modulus data for the composite towers along with Eqn. 4.7 given as a dashed line. While there is a positive slope to the tower data, a least squares fit (solid line) shows that tower data both underestimates the zero pressure modulus (137 GPa compared to 160 GPa) and the first pressure derivative (1.72 compared to 6.67). This can partially be explained due to a triaxial stress state (with significant shear components) in the Si core during indentation rather than a purely hydrostatic stress that Murnaghan assumes or uniaxial stress that Mook [45] assumes. In addition, there is likely the formation of a Si II phase, which has an elastic modulus that is ~66% smaller than diamond cubic Si [134] and could easily form at the measured contact stresses. Thus, while there is likely a pressure enhancement of the modulus, the

Murnaghan relationship cannot be applied directly. Evidence of a phase transformation is discussed in more detail in the following section.

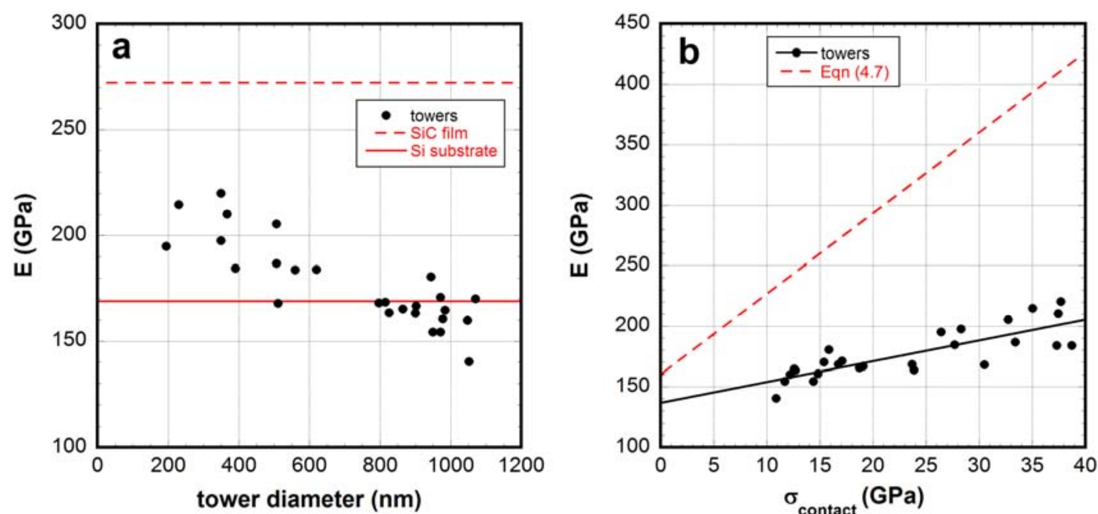

Figure 4.9 Elastic modulus as a function of (a) tower diameter and (b) the average contact stress for the FIB milled towers. The lines in (a) indicate the average modulus for the SiC film (without towers) and the Si(111) substrate (without the SiC film or towers). In (b), the dashed line is Eqn. 4.7 while the solid line is a least squares fit through the composite tower data.

4.5.2 Fracture and phase transformation of the FIB milled towers

Using the same procedure as the previous section, indents were made to deeper penetration depths to examine the fracture properties and phase transformations. Figure 4.10 shows a series of load-displacement data with their corresponding post indentation SEM image for displacement-controlled indents from 50 nm (Fig. 4.10a,b) to 175 nm (Fig. 4.10k,m). For the shallow penetration depths (50-100 nm, Fig. 4.10a-f), there are no signs of fracture, either in load-displacement data (signified by load drops) or cracking from the post indentation SEM images (originating from the indenter vertices).

Note that this criterion was used in the previous section to analyze the elastic-plastic properties in the absence of fracture. At these depths, however, there is substantial plastic yielding, as observed in the residual displacement between the loading and unloading curves. In addition, the white areas surrounding the indenter impression suggest considerable plastic pile-up. Figure 4.11 shows a contact mode AFM scan of the 75 nm indent from Fig. 4.10c,d along with a line trace over indenter impression and suspected pile-up region. This result confirms that the high contrast from the SEM data surrounding the indent is height related. Interestingly, the three-fold symmetry surrounding the indent is expected for slip along the {111} planes in Si(111) [135] depending on the indenter-substrate alignment. However, the extent of plasticity required to produce ~15 nm of pile-up is much larger than expected [136] and is discussed in terms of possible phase transformations later in this section. Finally, using the dotted ring from the Au in the SEM images as an indicator of the SiC shell-Si core interface, note that the pile up region in each of the indents shown in Fig. 4.10a-f is contained within the Si core.

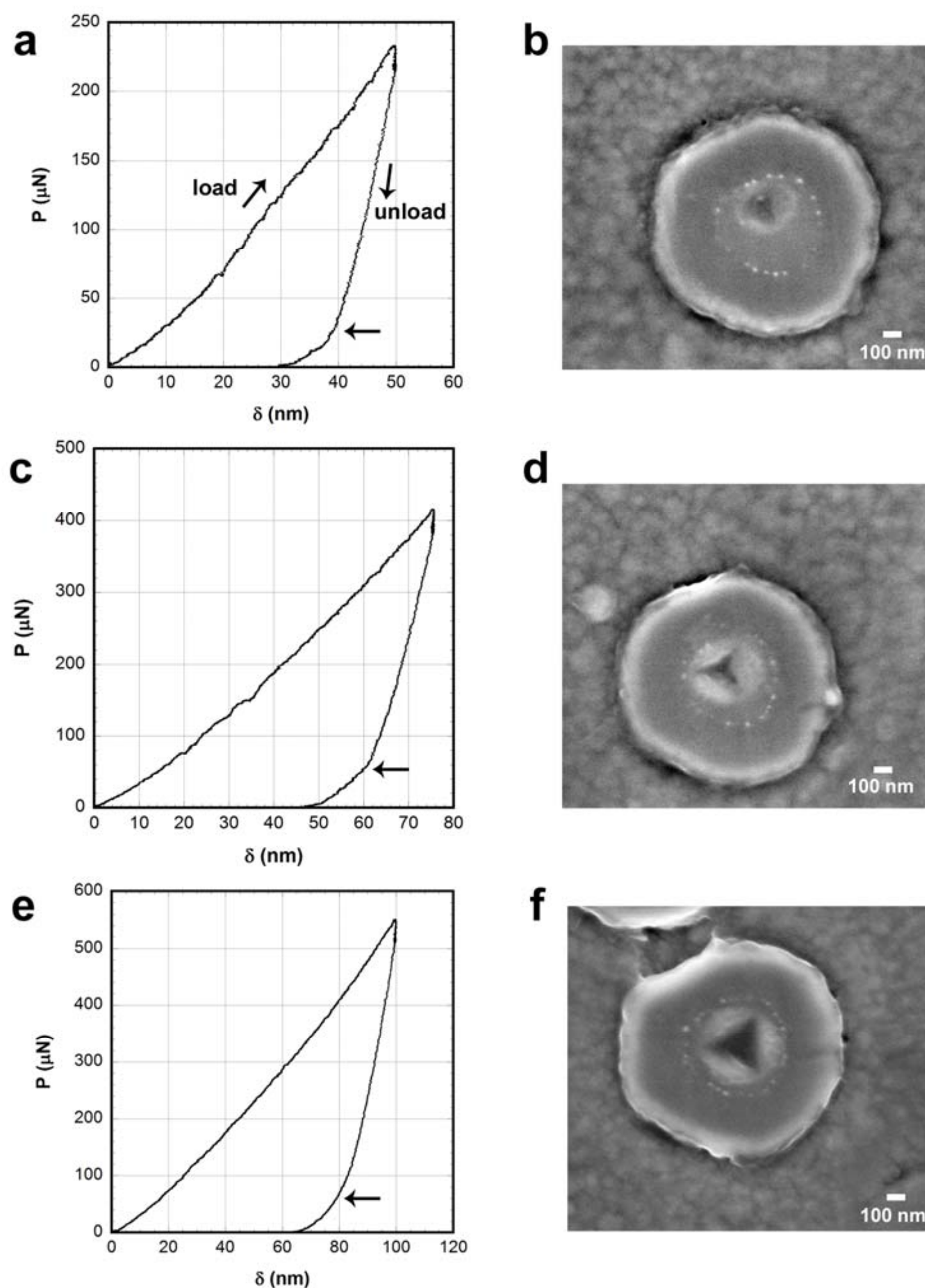

Figure 4.10 Load-displacement data (left column) and corresponding post indentation SEM images (right column) for displacement-controlled indents to 50 nm (a,b), 75 nm (c,d), 100 nm (e,f), 125 nm (g,h), 150 nm (i,j), and 175 nm (k,m). Vertical arrows identify load drops in the loading curves while horizontal arrows identify elbows in the unloading curves.

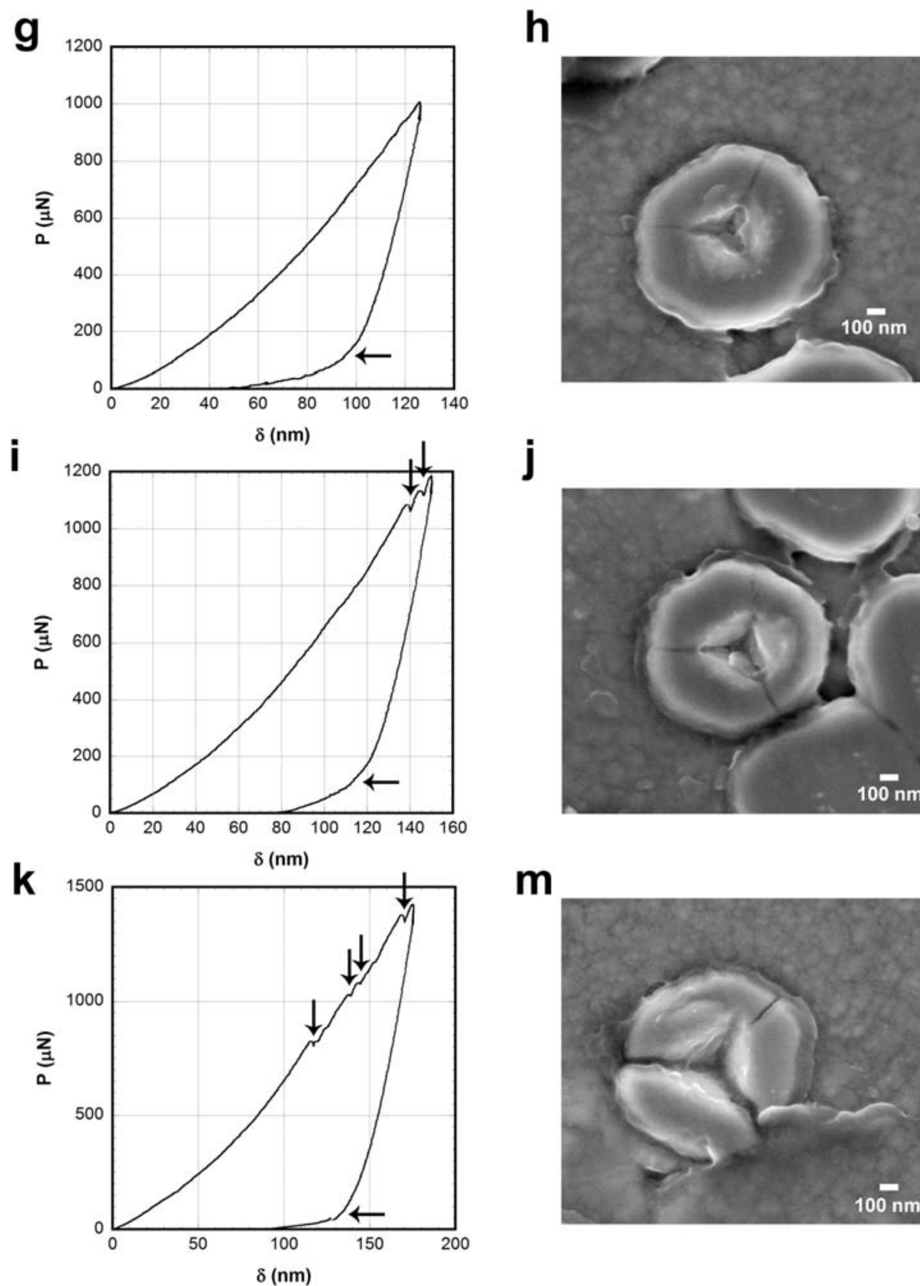

Figure 4.10, continued Load-displacement data (left column) and corresponding post indentation SEM images (right column) for displacement-controlled indents to 50 nm (a,b), 75 nm (c,d), 100 nm (e,f), 125 nm (g,h), 150 nm (i,j), and 175 nm (k,m). Vertical arrows identify load drops in the loading curves while horizontal arrows identify elbows in the unloading curves.

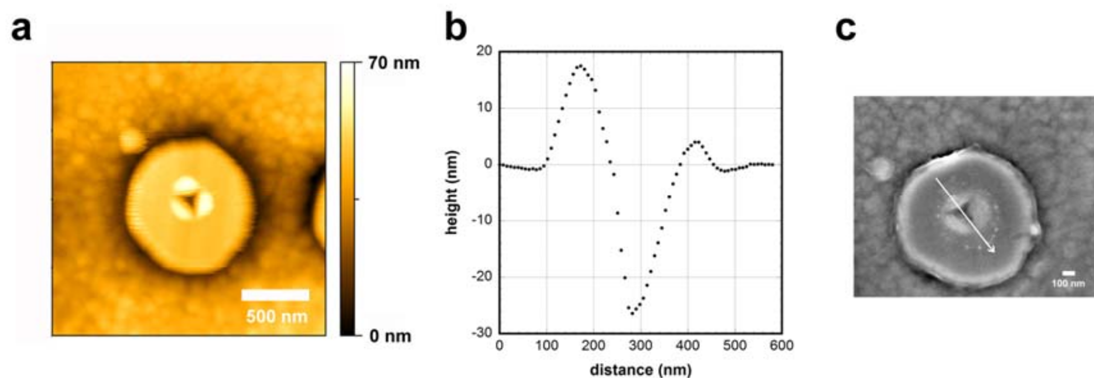

Figure 4.11 Contact mode AFM scan (a), AFM line scan (b), and SEM image showing the orientation of the line scan (c) for a 75 nm indent (same as Figure 4.10c,d).

At the deeper displacements (125-175 nm, Fig. 4.10g-m), there is visual evidence of fracture events in the post indentation SEM images. At 150 and 175 nm depths (Fig. 4.10i,k), there are also corresponding load drops that are highlighted with vertical arrows. It is important to note that in each of the examples, cracking consistently initiates in the SiC shell rather than the Si core, despite the fact that the Si core will experience the greatest stresses under load and should be much more brittle than the SiC shell. One explanation, that is discussed in more detail in Section 4.6, is the stress distribution in the composite tower established by the CTE mismatch. During the rapid cooling process following the deposition of the SiC film, the CTE mismatch between the SiC and Si will leave the Si core under compression and the SiC in tension. The compressive stress on the Si core will inhibit the growth of cracks within the Si. However, once the indentation driving stress at the Si-SiC interface is high enough, the residual tensile stress in the SiC shell will help the propagation of the crack through the

SiC. This is evident in Fig. 4.10g-m, where cracks are observed to always extend to the interface between the SiC shell and the surrounding film.

Figure 4.12a demonstrates that the fracture toughness depends on the composite tower size (using Eqn. 3.4). For the larger towers (diameters > 900 nm), the fracture toughness is relatively constant and is close to the toughness of the Si substrate. At smaller tower diameters, the fracture toughness increases to more than three times the toughness of Si. This is illustrated for various sized towers in Fig. 4.12b-d, with (b) d=925 nm, K_{Ic}=0.74 MPa*m$^{1/2}$, (c) d=763 nm, K_{Ic}=1.63 MPa*m$^{1/2}$, and (d) d=601 nm, K_{Ic}=2.51 MPa*m$^{1/2}$. One of the few studies [41] that has looked at the length scale dependence on the fracture toughness of Si nanotowers found a similar increase in toughness with decreasing tower diameter. Assuming that the Si core diameter is approximately half the total composite diameter (since the core-shell interface is not always obvious and the ½ factor agrees with the examples where the interface is clear), the measured toughness for the tower shown in Fig. 4.12d agrees relatively well with results from Ostlund et al. [41] that found a toughness of 2.9 MPa*m$^{1/2}$ for a 400 nm diameter Si tower. A proposed toughening mechanism that explains this increase is discussed in Chapter 5.

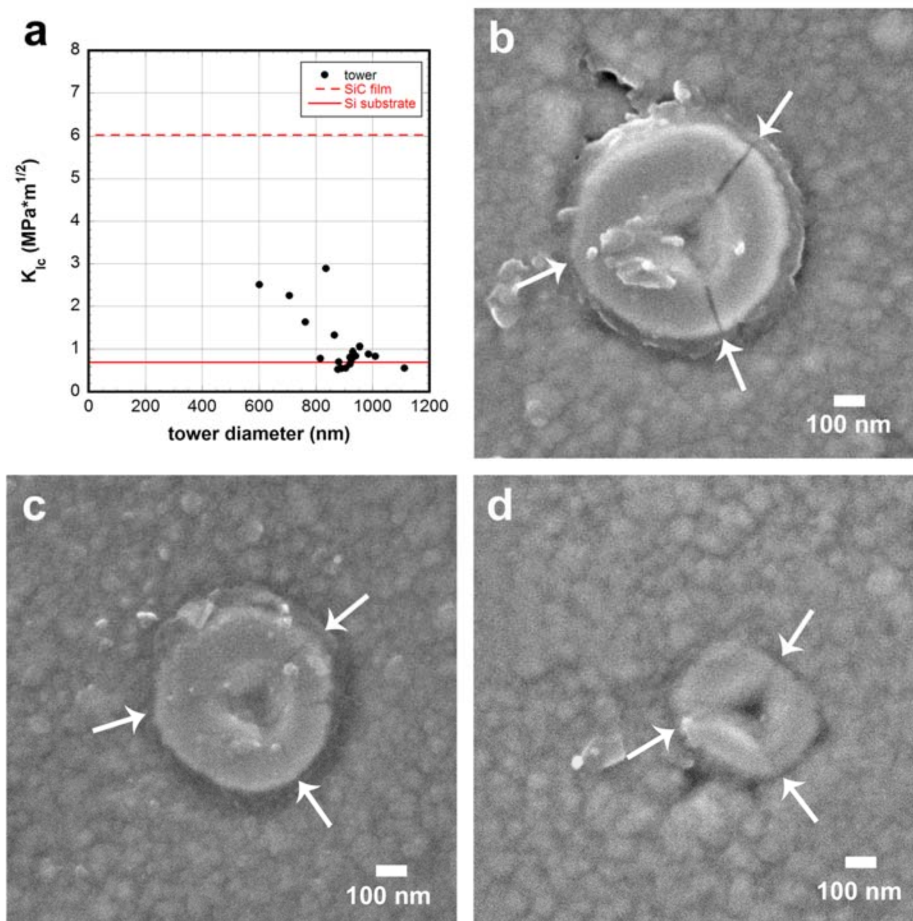

Figure 4.12 Fracture toughness measurements as a function of tower diameter (a) along with three examples (c-d) of residual impressions used in the toughness calculations. The red lines indicate the average fracture toughness for the SiC film (without towers) and the Si(111) substrate (without the SiC film or towers).

One final detail to take note of in the progression of indents shown in Fig. 4.10 is the elbow in the unloading curve. This is labeled with a horizontal arrow and is present in each of the six representative indents. Figure 4.13 shows the load-displacement curve for the tower shown in Fig. 4.10c,d replotted with a power law function fitted to the upper ~60% of the unloading curve (red line). As discussed in

Chapter 2, the unloading response for elastic-plastic indentation can be approximated by a power law function (see Eqn 2.7), which includes the residual depth of penetration and material constants [77]. In the present case, the slope of the unloading curve decreases abruptly near the end of the unloading, creating an elbow. The location of the elbow can be defined as the point where the unloading curve deviates from the power law fit. This type of feature is commonly seen during the indentation of silicon and has been attributed to the transformation of the high pressure β-Sn phase of Si to an amorphous phase (a-Si) [83, 93, 135].

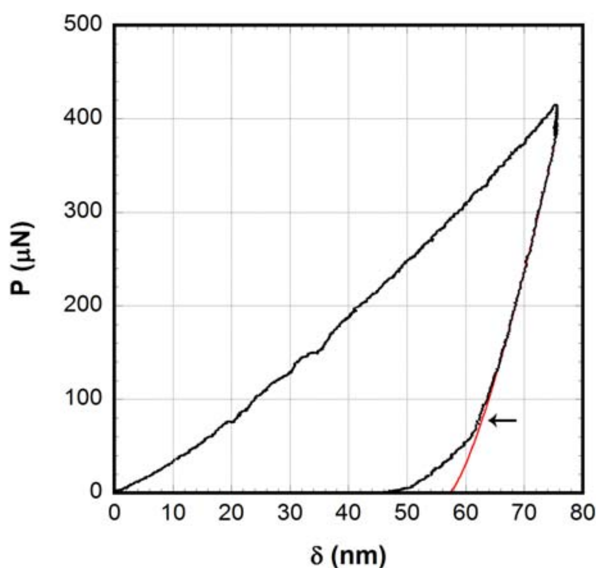

Figure 4.13 Load-displacement data from tower shown in Fig. 4.10d along with a power law fit to the unloading curve (shown in red). The elbow on unloading is indicated with a horizontal arrow.

The phase transformation of silicon has received much attention in the past twenty years by the indentation research community due to the presence of large stresses during nanoindentation which can trigger the transformation. However, unlike

conventional diamond anvil cell studies [137, 138] which load specimens hydrostatically, indentation involves large shear stresses at the edges of the indenter which can alter both the transition pressure and the resulting phase upon unloading. This transformation process under indentation loading has been studied with a range of complementary techniques, including confocal Raman microscopy (CRM) [92, 93, 135], TEM (both post indentation thin foils [82, 139] and *in situ* indentation [140]), electrical measurements [82, 83, 141], and molecular dynamics [142, 143]. Together, these studies have developed a commonly accepted progression of events during the indentation process. During loading, the diamond cubic Si (Si I) immediately beneath the center of the indenter transforms to metallic β-Sn (Si II) at hydrostatic pressures near 12 GPa for Si(100) and 8 GPa for Si(111) [135, 144]. As the load is increased, the Si II region under the indenter expands and can cause a pop-in event in the load-displacement due to the 22% volume decrease from Si I to Si II. This can also lead to the plastic flow (or extrusion) of material at the edges of the indent [136, 145], which after pressure relief reverts to a-Si. During the unloading process, either a pop-out or elbow is usually observed depending on the rate of unloading. Figure 4.14 gives examples of pop-outs and elbows in load-displacement data. This is a product of the Si II expanding during the transformation into a combination of rhombohedral (Si XII) and body centered cubic (Si III) after a pop-out or a-Si after an elbow [17, 21]. While Si XII and Si III are the thermodynamically preferred phases upon unloading, the presence of a-Si is attributed to kinetic entrapment during rapid unloading [83].

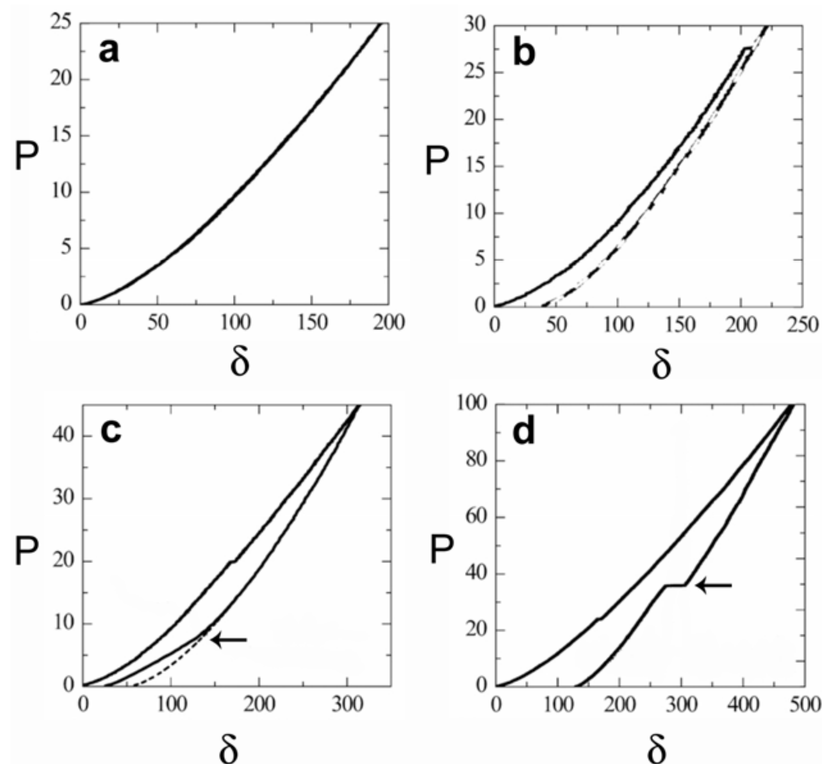

Figure 4.14 Load-displacement curves showing characteristic unloading curves for an elastic response (a), plastic response (b), elbow (c), and pop-out (d). Dash lines show the power law unloading fit in (b, c) while arrows indicate the location of the elbow and pop-out features in (c, d). Adapted from Gerbig et al. [135].

The present study is unique in that it involves both small volumes of Si and biaxial confinement from the SiC shell. In the tower load-displacement data that clearly shows an elbow on unloading, there is an average transition stress of 2.9 $\pm$ 1.2 GPa for a Si core diameter of 451.3 $\pm$ 48.2 nm. Literature discussing the size effect on the Si phase transformation process [24, 28, 30, 34] is much more limited (and inconclusive) than bulk studies. Diamond anvil cell compression experiments by Tolbert et al. [138] of Si nanocrystals (d=10-50 nm) found a Si I to Si II transition pressure of 22 GPa and

recovery to a-Si upon unloading. This result is surprising in that the transition pressure is two times larger than observed for bulk samples and the resulting phase is not crystalline (Si XII or Si III) despite slow unloading. The results of Tolbert et al. are in conflict with those of Ge et al. [146] and Minor et al. [140], who find that phase transformations cease to occur in Si wedges at plateau widths less than 350 nm and are replaced by dislocation plasticity. These studies [28, 34] involved TEM *in situ* nanoindentation of Si(110) wedges with plateau (top surface) widths ranging from 100-1600 nm. The discrepancy between Tolbert's and Ge's findings is due to a difference in the state of stress and is addressed in more detail in Chapter 5. Figure 4.15 shows data reproduced from Ge et al. for increasing wedge plateau widths (100-1600 nm) along with power law fittings added to the unloading curves. While the authors claim an absence of elbows in this data, the power law fittings show distinct elbows in each of the samples. To determine the stress at the elbow, the Thurn-Cook two-parameter area function [78] was used knowing the tip geometry (Berkovich) and radius of curvature (120 nm) as reported by Ge et al. The resulting transition pressures as a function of critical dimension are plotted in Figure 4.16. In the case of the wedges, the critical dimension is the plateau width. In addition, the average transition pressure found from the composite tower data reported earlier (Fig. 4.10) and the bulk transition pressure for Si(111) [135] are also shown. For the composite tower data, the critical dimension is the Si core diameter. For the bulk Si data, the critical dimension is the plastic zone diameter, as defined by Eqn. 3.3, where the applied load is taken as the load where elbows are first observed in bulk Si(111) indentations [135]. The yield strength is

approximated by the Tabor relation [114] using the hardness for Si(111) [147]. Note that while the wedge data is (110) oriented, bulk Si values are reported for Si(111) since the towers are (111) oriented and the elbow transitions for (111) and (110) Si are quite close ($\pm$ 0.1 GPa).

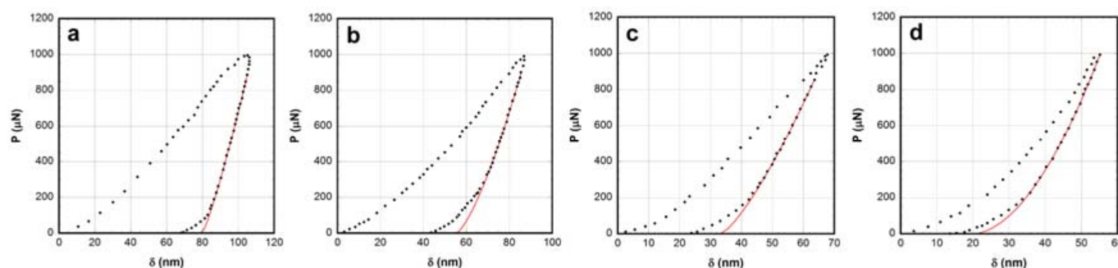

Figure 4.15 Load-displacement data from Ge et al. [146] along with a power law fit to the unloading curve (shown in red). All of the indents are load-controlled to 1 mN and are on Si wedges with plateau widths of a) 100, b) 200, c) 350, and d) 1600 nm.

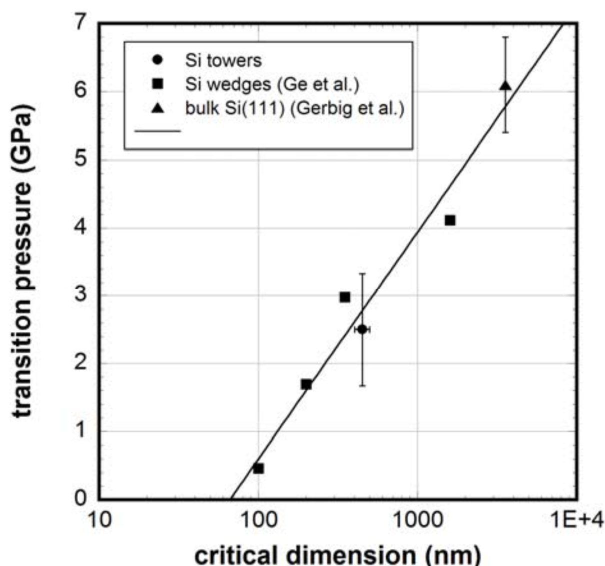

Figure 4.16 Transition pressure on unloading as a function of critical dimension for the Si towers (diameter) along with Si wedges (plateau width) [146] and bulk Si(111) [135]. A logarithmic fit is given as a guide to the eye.

The data in Figure 4.16 shows a decreasing transition pressure upon unloading for a decreasing critical dimension. This suggests increased stability (at lower pressures) of Si II at small scales, which is in agreement with theoretical studies of Si II nanocrystals that predict metastability due to the absence of defects [148]. It is less clear why the Si wedges and towers revert to Si I rather than a-Si (as found with the 50 nm nanocrystals [138]) if a phase transformation is truly involved. While a reversion to Si I has been found in MD simulations of the compression of 10 nm diameter Si spheres [142], it has not been seen experimentally in indentation experiments. In the case of the wedges, this could be a result of structural changes during TEM thin foil preparation for the larger wedges and e-beam enhancement effects [55] at an accelerating voltage of 300 kV for the smallest wedges deformed *in situ*. For the composite towers, post

indentation composition was measured using CRM. While these show no signs of an amorphous phase, a relatively small volume (and thus weak Raman response) of the a-Si may have been below the detection limit of the instrument. The combined effects of dislocation plasticity and phase transformation plasticity are discussed in more detail in Chapter 5.

4.5.3 *In situ* indentation of the as-deposited towers (batch A)

A second series of indentation experiments were run with the Si composite towers using SEM *in situ* indentation (Hysitron® SEM Picoindenter) at EMPA Swiss Federal Laboratories for Material Testing and Research in collaboration with W. Mook and J. Michler. The details of the technique are given in Chapter 2. These experiments were intended to determine the strength and fracture toughness of the composite towers as a function of tower diameter, FIB processing (presence/absence of SiC capping the Si core), and RTA treatment. However, due to a limited amount of equipment time and problems with both the experimental procedure and sample preparation, the results from the study were few and primarily qualitative in nature.

A series of 28 indents on 18 towers were run over the course of 2 days. The experiments were run in displacement control, with a loading rate of 0.5 nm/s. Maximum displacements were limited by the load capacity (P_{max} = 1.5 mN). Previous uniaxial compression experiments by Östlund et al. [41] on Si microtowers found cracking along the length of the tower using a flat-punch indenter. However, in the present case, due to the increased strength and toughness from the SiC shell, a sharp

(r = 65 nm) cube corner was needed to reach high enough stresses to initiate cracking. The first problem with indenting 2D structures with this tip geometry is tip-sample alignment. Figure 4.17 shows a representative tower indent where this is clearly illustrated. Figure 4.17a shows an image just before the indent as seen from the same perspective as during the experiment. From this 2D projection, the tip appears to be well aligned with the tower. However, sample rotation for additional vantage points is not possible due to the close proximity of the tip to the electron detectors (see Figure 2.16). Figures 4.17b,c show the tower base after the indent imaged at a) 75° tilt and b) 0° tilt (plan view). The arrows highlight the location of the base (black arrow) and the impression of the indenter (white arrow). Based on the offset between these two locations, the tip was likely aligned too far back on the tower. As the indent progressed, the indenter likely slid down the backside of the tower and eventually caused it to fail by a shearing motion. This is evident by the ledge at the front of the tower base in Fig. 4.17c.

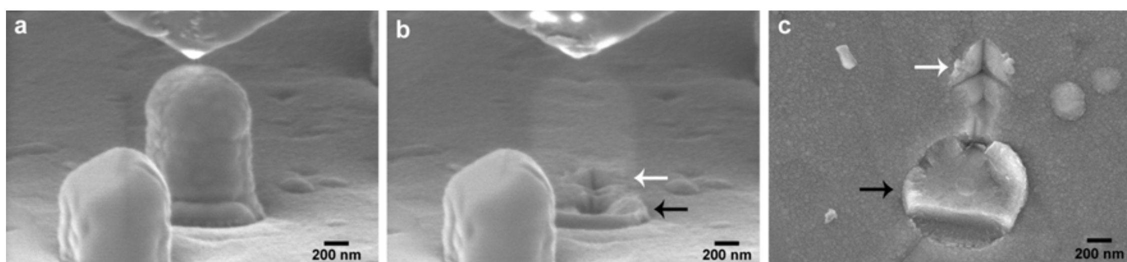

Figure 4.17 Example of tip-sample alignment problems during SEM *in situ* indentation. Images are of the tower before (a) and after (b,c) indentation taken at 75° tilt (a,b) and plan view (c). The arrows in (b,c) show the location of the tower base (black) and the indenter impression (white).

For well aligned indents, the second problem that was encountered was the formation and unstable growth of multiple cracks in the SiC shell. Figure 4.18 shows an example of a tower that failed catastrophically. As shown in load-displacement data (Fig. 4.18c), the tower is loaded smoothly without any observable discontinuities (fracture or plasticity) up to 1 mN. The inflection in the data just beyond this point (labeled with a black arrow) signifies the crack initiation. However, the crack growth and tower failure occur too quickly to stop the indentation and is even missed in the 30 fps video imaging. Fragments from the SiC shell are labeled in Fig. 4.18b,d with white arrows, suggesting separation of the Si core and SiC shell during failure.

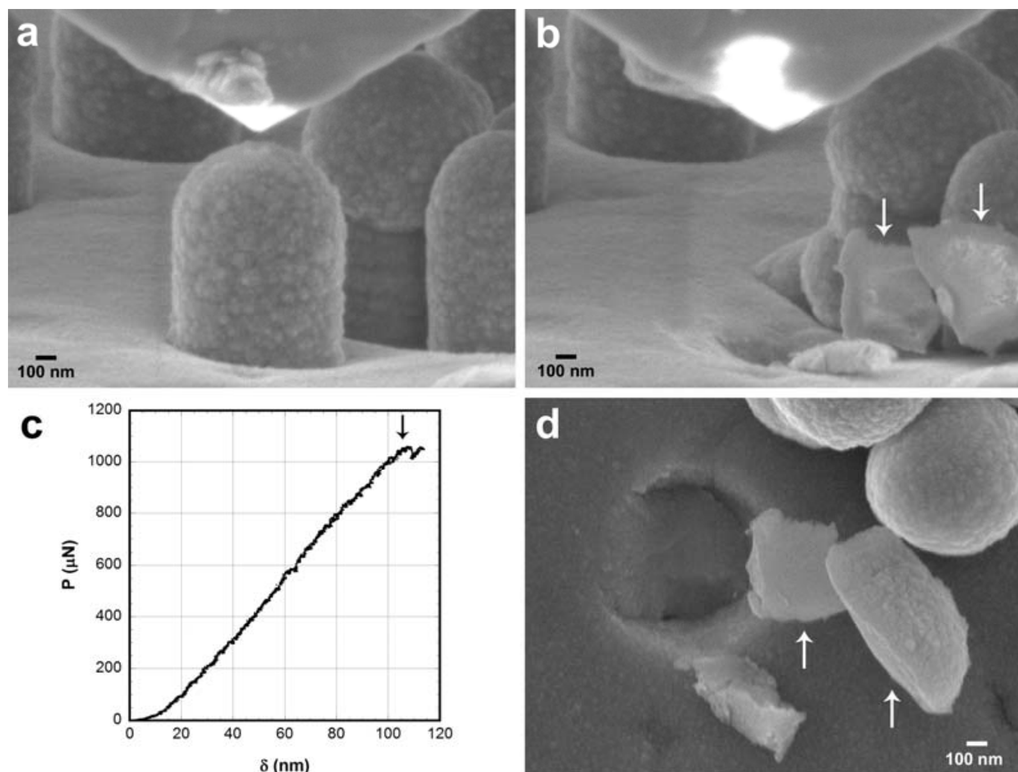

Figure 4.18 Example of unstable crack growth during SEM *in situ* indentation. Images are of the tower before (a) and after (b,d) indentation taken at 75° tilt (a,b) and plan view (d). The load-displacement data is shown in (c), with the inflection point labeled with an arrow. Arrows in (b,d) show fragments of the SiC shell.

Figure 4.19 shows an example of a tower that fractures, but where the crack arrests prior to the collapse of the tower after the indenter is withdrawn. The load-displacement curve again shows an inflection near the peak load. However, in this case, the indent was aborted and unloaded. Imaging of the tower in plan view (Fig. 4.19d) reveals distinct cracking, both in the SiC shell (vertical arrows) and in the surrounding SiC film (horizontal arrow). The fracture toughness of the tower cannot be found by the commonly applied method of Lawn and Marshall [149] for brittle solids due to the

curvature of the tower top. Rather, a Griffith-Irwin work per unit fracture area approach is used, by balancing released elastic strain energy with the creation of new surfaces. The new surface area is approximated as three sectors, using the measurements of the crack lengths in Fig. 4.19 b,d to determine the edge lengths. The fracture energy is the total applied energy (area under the loading curve) minus the recovered elastic energy (area under unloading). This energy divided by the total new surface area is the strain energy release rate, G_{Ic}. Using the elastic modulus for SiC and $G_{Ic} = K_{Ic}^2 / E$ (assuming plane stress), this approach gives a fracture toughness $K_{Ic} \sim 4.6$ MPa*m$^{1/2}$. This is likely an underestimate of the true fracture toughness, as crack growth along the curved tower top lacks the geometric constraint that is found in bulk measurements. Despite this, the result agrees well with the measurements for the SiC film and the FIB milled towers shown in Fig. 4.12, falling midway between the two results. Finally, this example also shows cracking in the SiC film surrounding the tower (Fig. 4.19d). This type of film cracking is also seen at the bottom edge of the tower in Fig. 4.17c. While it is unclear if these cracks are a result of the indent, the orientation matches the vertices of the indenter and suggests half-penny type cracking along the length of the tower into the film/substrate. This hypothesis agrees with the crack growth behavior observed in the FIB milled towers indented *ex situ*, where the cracks would extend all the way through the SiC once they were initiated due to the tensile residual stress in the SiC shell (Fig. 4.10g-m). For these indents, a similar mechanism would drive the crack down the length of the tower and into the film. When the tower fails, this would lead to fragmentation of the SiC shell, as observed in Fig. 4.18.

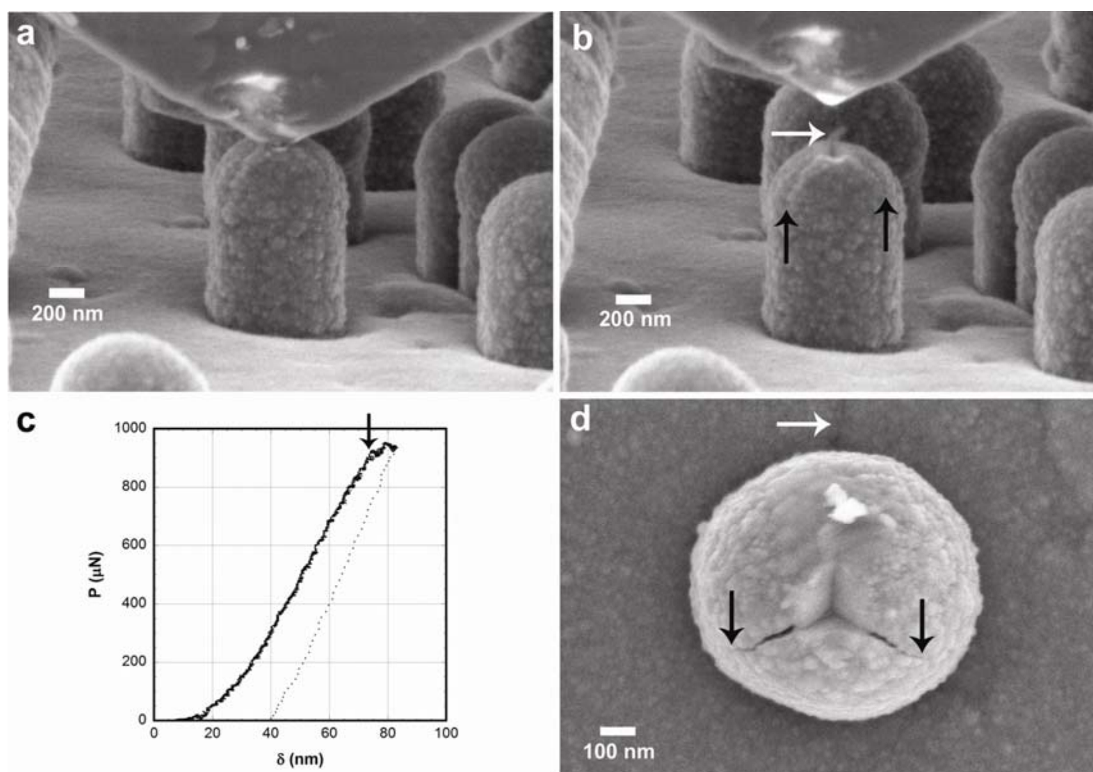

Figure 4.19 Example of stable crack growth during SEM *in situ* indentation that arrests before the tower collapses. Images are of the tower before (a) and after (b,d) indentation taken at 75° tilt (a,b) and plan view (d). The load-displacement data is shown in (c). Arrows in the (b) highlight extruded material from the top of the tower (white arrow) and cracks along the tower edge (black arrows). The arrow in (c) shows the inflection point. All of the arrows in (d) identify cracks.

In addition to the fracture, it is also worth noting the material that is protruding from the top of the tower in Fig. 4.19 (labeled with a white arrow). This nanowire was drawn out of the center of the tower during the tip withdraw. Of the materials that could be present (Si, SiC, Au), only Au or Si II would be expected to flow. While Si II may be formed under compression (as discussed in Section 4.5.2), it should revert to a much

more brittle phase when the compressive stress is released. The possibility of Au being drawn into a nanowire is much more plausible, as it has been shown to be present in composites after the deposition of the SiC shell (Section 4.4). This reinforces the Au contamination problems with this batch of composites.

In addition to indenting the as-deposited towers, indents were run on towers with the SiC cap removed with FIB milling. Figure 4.20 shows a representative tower, with the SEM images after the indent and the load-displacement curve. Note that the FIB milling height is much higher along the composite tower than used in the in-plane milling used for the *ex situ* indents. After loading the tower to ~1.5 mN, the plan view image (Fig. 4.20b) shows no signs of cracking at the edge of the indents. This is dissimilar to the towers indented *ex situ* (Fig. 4.10), that began to show severe cracking above 1 mN. However, the FIB milling in Fig. 4.20 may not have been far enough down the tower to remove the SiC cap and expose the Si core. This would explain the increased toughness (no cracks in Fig. 4.20b), as the SiC is tougher than the Si and the flat surface indenting should provide the geometric confinement that is lacking in as-deposited case (see Fig. 4.18, 19). This idea is also supported by the absence of an elbow on unloading (see Fig. 4.20c), which was commonly found in *ex situ* indents on Si.

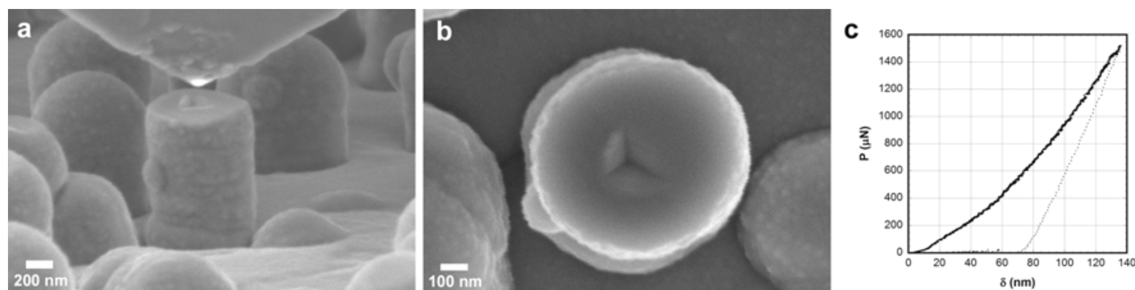

Figure 4.20 Example of a SEM *in situ* indentation into a FIB cut tower. Images are of the tower a) before and b) after indentation taken at 75° tilt (a) and plan view (b). The load-displacement curve is shown in (c).

The final set of indents were on towers that were RTA treated prior to indentation. Figure 4.21 shows an example of an indented tower after a 1200°C RTA. The two images are of the same region after the indentation, with Fig. 4.21b being tilted 40° and rotated 90° clockwise from Fig. 4.21a. The tower in the center of Fig. 4.21a was originally targeted for the indent. The tower failed in a similar shearing motion as shown in Fig. 4.17, however, here the failure occurred midway down the length of the tower. The indenter was also misaligned with the tower, as shown by impression of the indenter well beyond the tower (labeled with a black arrow) in Fig. 4.21. This caused the top vertex of the indenter to cross-section the tower in front of the one targeted, revealing a hollow core (~110 nm diameter). This is labeled with a white arrow in Fig. 4.21b, along with an example of a hole in the base where a tower previously stood. This is similar to what was observed with the annealed FIB cut tower (see Fig. 4.6d), where the 1200°C RTA treated tower showed a hollow core tower surrounded by particulate debris. This was attributed to the rapid diffusion of the Au from the Si-SiC interface followed by the diffusion of interstitial Si to the free surface. In the tower

shown in Fig. 4.21, it is unclear where Si core material diffuses to, as there is no free surface during the annealing process. However, it confirms the severity of the problem of the Au catalyst remaining in the composite tower and makes measurements of the core-shell residual thermal stresses problematic for composites where the Au caps remain (as in batch A).

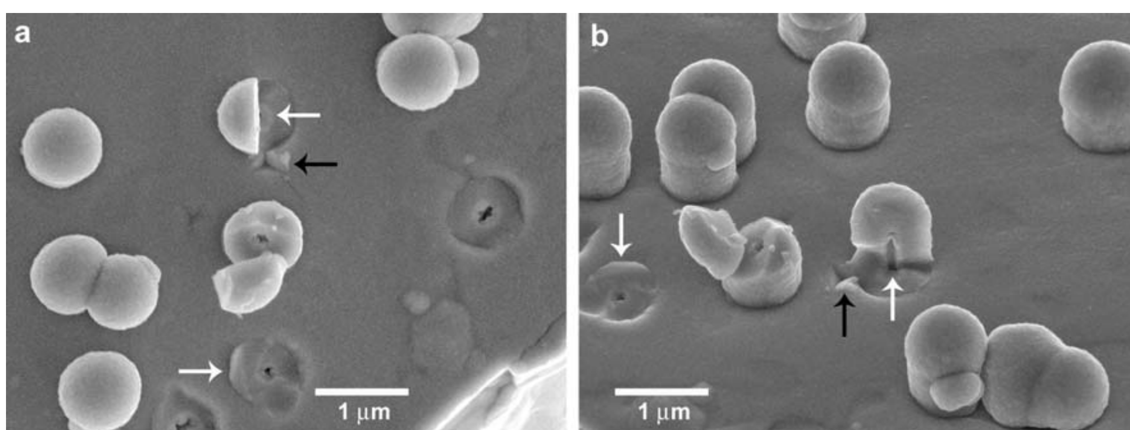

Figure 4.21 Structural changes to the composite towers after 1200°C RTA treatments. Images show the same region in a) plan view and b) at 40° tilt after rotating 90° clockwise. The black arrow shows the indent impression in the film. The white arrows highlight examples of hollow cores.

4.6 Confocal Raman microscopy on batch A composite towers

Confocal Raman microscopy (CRM) was used to determine the magnitude of the stress on the Si core. The experimental procedure is described in Section 2.5.6. The Raman experiments in this section were performed at EMPA through a collaboration with P. Brodard. The difference between the Si(111) spectrum in an unstressed state and the spectrum from the Si core in the composite tower can be related to the magnitude of

stress in the Si. By assuming the Si core is under a biaxial stress, Eqn. 2.17 was used to find the stress for the as-deposited sample and samples RTA treated at 900°C and 1200°C. Figure 4.22 gives the average stress for five measurements at each condition. While the data shows the expected trend from the as-deposited to the 900°C annealed sample, only the sample annealed at 900°C is close to the stress predicted by the elasticity argument presented in Section 4.2. The tensile stress in the as-deposited sample can be disregarded due to the large error associated with this result. The relaxation from 900°C to 1200°C is likely due to the increased contributions of the Au contamination and the resulting hollow core observed in Fig. 4.21. In addition to the problems with the Au contamination, there is likely also error due to axial variations in the stress. This is addressed in more detail in the following section.

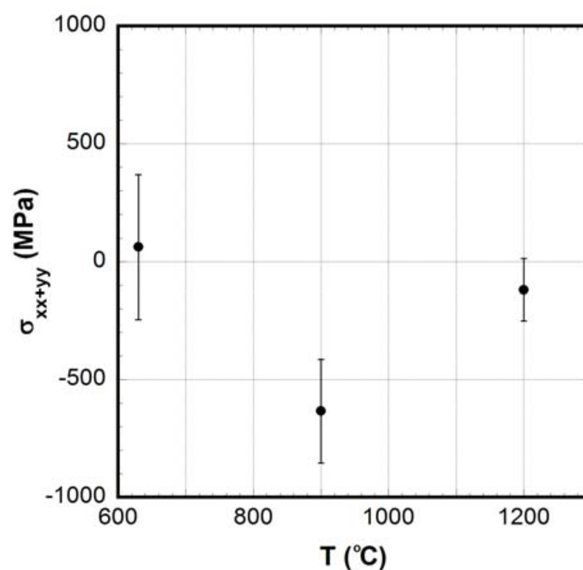

Figure 4.22 Biaxial stress as measured from the Raman shift for the as-deposited sample (630°C) and samples RTA treated at 900°C and 1200°C.

While most of the peak shifts (relative to the stress-free sample at ~521 cm^{-1}) were <2 cm^{-1}, there were a few instances of much larger shifts (10-15 cm^{-1}) or shoulders that were well below the expected range of shifts. Figure 4.23 shows two examples from the as-deposited towers and two from the annealed at 1200°C. If interpreted as a stress, these would represent up to 7 GPa of tensile stress in the Si core. However, this does not make physical sense. A second explanation is the presence of nanocrystalline Si. For Si with a grain size between 3 and 10 nm, there is a shift in the Raman peak from 512 to 520 cm^{-1} [150, 151]. As discussed in Chapter 3, there is a small (yet unknown) fraction of free Si in the nc-SiC due to incomplete carburization during the deposition. However, due to the high measured hardness and the decrease in toughness in the thin films with annealing, there is likely not enough nc-Si present to explain the observed Raman peaks. In addition, the distribution of Si grains would be included in the grain size measurement of 14.4 $\pm$ 5.1 nm, since it was measured by image processing of SEM micrographs. Grains of this size would have a much smaller (if any) shift than those observed and thus are not likely the cause of the shift.

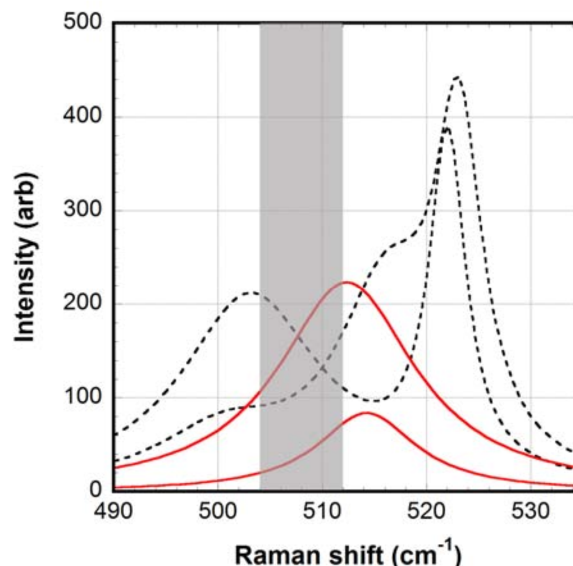

Figure 4.23 Raman spectra for as-deposited (black, dashed line) and 1200°C RTA treated (red, solid line). The characteristic signal for Si IV (508 $\pm$ 4 cm^{-1}) is shown in grey.

A third explanation for the additional peaks is due to a phase transformation in the Si. Of the 12 polymorphs of Si, there are only a few, including Si III and IV, that are stable at ambient conditions. Of these, only Si IV has a Raman line (508 $\pm$ 4 cm^{-1}) that is in the region of interest [152]. This region is shaded grey in Figure 4.23. Micro-Raman [92] and HRTEM [153] analysis of Vickers indentions into (100)Si have shown that Si IV can form during unloading from Si II under certain combinations of unloading rate and/or annealing [92]. This route is however unlikely in the current situation, since it would require the Si core to have experienced compressive stresses greater than 8 GPa to form Si II [144] and then revert to Si IV if this were pure Si at room temperature. However, Si IV has also been shown to be metastable in nanowires ranging from 20-100 nm in diameter due to high surface stresses [94, 95]. While the

data is too sparse to make a firm conclusion, a unique combination of sample geometry and loading conditions in the current system may lead to Si IV phase transformations.

4.7 Deposition of SiC coatings on Si nanotowers without Au caps (batch B)

The deposition of SiC coatings on batch B followed the same procedure as batch A, with the substrate temperature held between 450-550°C and deposition times of 10 min. However, the SiC film was not as thick, ranging from 100-200 nm. This difference in thickness despite similar deposition conditions with batch A is due to the strong radial dependence (with respect to the center of the nozzle) of the growth. Due to the experimental configuration, the radial alignment of the substrates is slightly different from deposition to deposition (see Fig. 2.2). Therefore, subsequent analysis used samples from approximately the same deposition with the same radial position. Figure 4.24 shows an example of the as-deposited structure, with (a) the Si prior to the deposition imaged in bright field (BF) TEM and (b) the SiC coated Si imaged in dark field (DF) TEM. Note that most of the Au has been removed from the Si (although there are likely still Au nanoparticles decorating the sidewalls). In Fig. 4.24b, the tower was imaged in DF mode to reveal the composite structure. The image shows the conformal nature of the coating, with little evidence of shadowing. Additionally, the sharp interface gives good evidence that appropriate adhesion has been achieved.

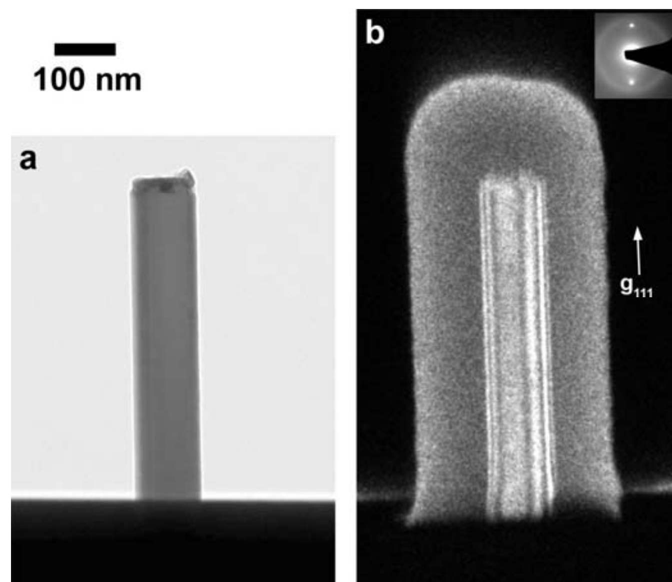

Figure 4.24 Examples of Si nanotowers from batch B a) before (BF TEM) and b) after deposition of the SiC coating (DF TEM). The parallel lines running down the length of the Si in (b) are from thickness fringes.

The towers were cross sectioned using the same FIB procedure described above for batch A and then RTA treated at 900-1200°C. Fig. 4.25 and 4.26 show the SEM and AFM imaging, respectively, of the cross sectioned towers after RTA treatment. In both figures, the top image is prior to the RTA treatment and the bottom image is afterwards. In the SEM micrographs, the height contrast between the core and shell becomes more pronounced with increasing RTA temperature, with 1200°C (Fig. 4.25d) giving the best example of the difference between the before-after images. The AFM scans confirm this interpretation of the SEM contrast, showing raised regions in the tower core following the RTA treatment. Of note also is the absence of the white dots and porous core with increasing RTA temperature that were associated with Au diffusion in batch A (see Fig.

4.6,7). This confirms the successful etching of most of the Au from the Si towers prior to SiC deposition.

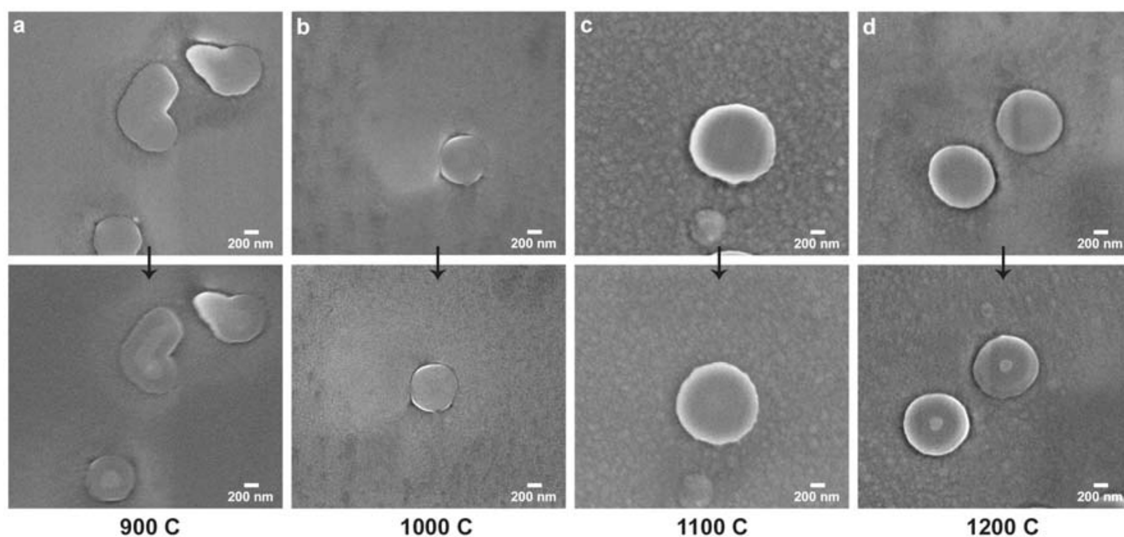

Figure 4.25 SEM imaging of representative batch B composite towers annealed to between 900 and 1200°C (a-d) in their before (top) and after (bottom) condition.

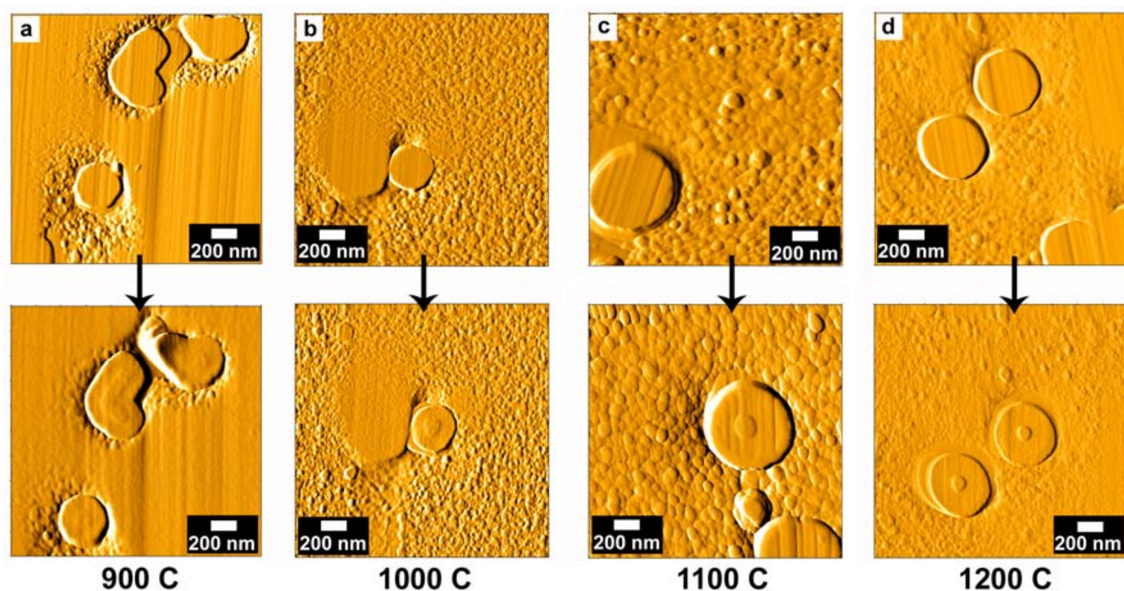

Figure 4.26 AFM deflection mode imaging of representative batch B composite towers annealed to between 900 and 1200°C (a-d) in their before (top) and after (bottom) condition.

The extrusion process with annealing can be quantified by measuring the height of the Si core above the surrounding SiC after annealing. Figure 4.27 gives an example of the AFM height data (a) and the corresponding line scan (b) for a 1200°C RTA treatment. Averaging these heights over a series of towers at each RTA condition gives a nearly linear increase in the extruded height with temperature, as shown in Fig. 4.27c. This agrees with a residual stress controlled extrusion process, as the CTE mismatch stress will vary linearly with temperature (see Eqn. 4.3). This leads to increasing deformation of the Si core and the plastic extrusion of material.

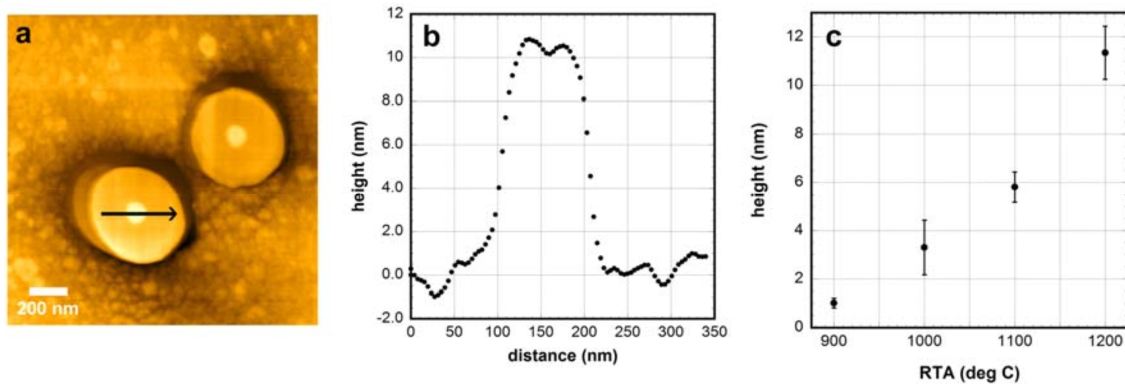

Figure 4.27 AFM contact mode imaging of a 1200°C RTA treated tower (a), along with a line scan over the extruded core (b) and the average height of the extruded core as a function of RTA treatment temperature (c).

The deformation in the Si core can be explained through creep processes. Creep rates in crystalline materials at high temperatures can be described by the following equation [154]:

$$\dot{\varepsilon} = A\left(\frac{DGb}{kT}\right)\left(\frac{b}{d}\right)^{p}\left(\frac{\sigma}{G}\right)^{n} \tag{4.8}$$

where $\dot{\varepsilon}$ is the creep rate, A is a dimensionless constant, D is the diffusion coefficient, G is the shear modulus, b is the Burgers vector, p is the inverse grain size exponent, σ is the applied stress, n is the stress exponent, k is Boltzmann's constant, T is the temperature, and d is the grain size. Plotting in the nondimensional form $\frac{\dot{\varepsilon} kT}{DGb}$ versus $\frac{\sigma}{G}$ can be used to determine n, p, and the activation energy, Q, of the system. In the present case, the applied stress can be measured by the CRM (discussed in Section 4.8) while an average strain rate can be approximated by the change in the Si core height after annealing divided by the time to cool to room temperature. Since the Si cores are single crystals, creep is controlled by a lattice mechanism and $p = 0$. Due to large change (more than six orders of magnitude) in the Si self-diffusion coefficient from 900-1200°C and the lack of an appropriate average temperature, the data was instead plotted as $\dot{\varepsilon}$ versus σ (see Figure 4.28). A power law fitting to the data gives $n = 1.96$. This is smaller than the expected stress exponent for sc-Si ($n = 3$) [155, 156], which follows a dislocation glide and climb type creep mechanism [157]. This deviation may be from contributions of T/D_{eff}, which was assumed in Fig. 4.28 to be constant with stress. In addition, there may be contributions from high impurity levels (10^{20} Au/cm^3) in the VLS grown Si nanowires [131]. While studies on doped Si (10^{20} phosporous/cm^3) have shown similar stress exponents compared to pure Si, creep studies at low strain rates ($\dot{\varepsilon} < 10^{-3}$) have been inconclusive in determining n due to inhomogeneous

deformation [158, 159]. This remains an open question that would be well suited for future TEM *in situ* indentation studies.

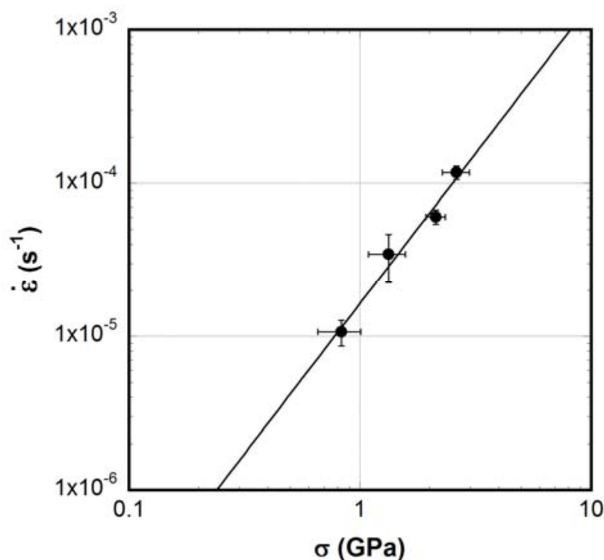

Figure 4.28 Strain rate versus stress for the tower data shown in Fig. 4.27c.The strain rate is an average strain rate over the cooling time during the RTA treatment. The applied stress is the biaxial stress on the Si core measured by CRM (discussed in Section 4.8). A power law fit is shown, with n = 1.96.

4.8 Residual stress analysis of batch B composite towers

While the increasing extrusion volume with temperature in the FIB cut towers suggests an increasing residual stress in the composite towers, a more direct way to quantify the magnitude of stress on the Si core is through confocal Raman microscopy (CRM). Note that unlike the Raman results discussed earlier for the batch A towers, the Raman data presented in this section was collected using a setup at the University of Minnesota's Characterization Facility. The experimental conditions were nominally the same as those for batch A, with a 514.5 nm Ar laser operated at ~0.7 mW and 2 min

sampling times. Using a 100x objective lens, the beam diameter was limited to 350 nm and thus could isolate Raman responses from individual towers. Spectral data was background corrected and fit to Lorentzian functions for analysis purposes. Figure 4.29 gives representative Raman spectra for a bare Si(111) wafer and those of the RTA treated (900-1200°C) composite towers. With increasing RTA temperature, the tower data shows a significant blue shift to higher wavenumbers. This trend is isolated to the tower response and not the underlying Si wafer, as can be shown by varying the focal height of the measurement. Figure 4.30 shows two examples of a 1200°C treated sample taken at the same *x-y* position but at different focal heights, with Fig. 4.30a collected 2.25 μm above (higher *z*) the data collected in Fig. 4.30b. Both spectra show overlapping peaks, with one at ~520.8 cm^{-1} (red curve) and the other at ~527.3 cm^{-1} (blue curve). At the higher focal height (Fig. 4.30a), the peak at ~527.3 cm^{-1} is larger due to a larger portion of the reflected signal coming from the tower. As the focal height is decreased, more of the signal is coming from the underlying Si wafer, making the peak at ~520.8 cm^{-1} dominant at lower *z* (Fig. 4.30b). For the results presented in Fig. 4.29 and the subsequent stress analysis of the towers, the focal height was adjusted to give a signal from the tower alone (single peak).

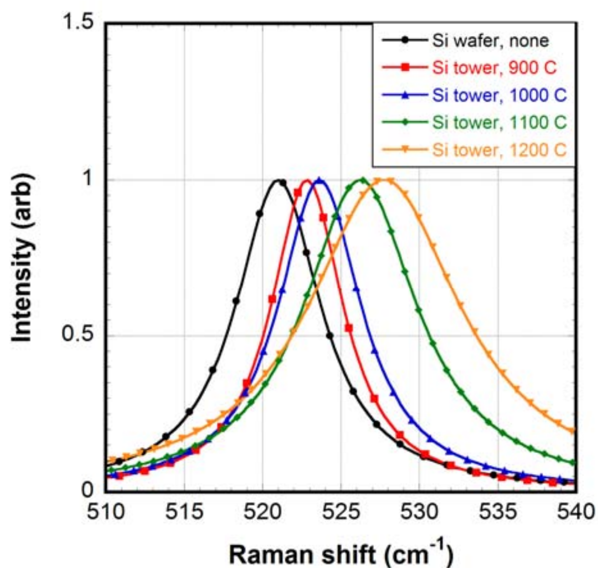

Figure 4.29 Representative Raman spectra (normalized, Lorentzian fittings) for a bare Si(111) wafer (black, circles) and RTA treated Si composite towers at 900°C (red, squares), 1000°C (blue, triangles), 1100°C (green, diamonds), and 1200°C (gold, inverted triangles).

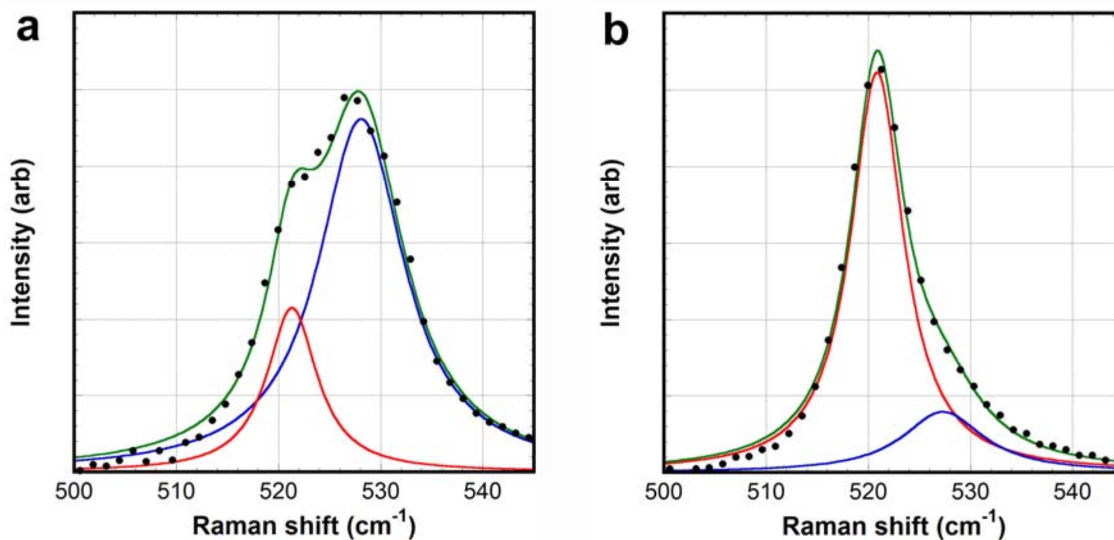

Figure 4.30 Examples of bimodal spectra at different focal heights, with (a) 2.25 μm above (b). The raw data is shown with black circles while the Lorentzian fittings are solid lines.

Figure 4.31 compares the Raman shifts for SiC coated Si wafers to the Si towers and bare Si(111) wafer as a function of RTA treatment temperature. The SiC coated Si wafer data in Fig. 4.31a all show a similar blue shift (until 1200°C) with respect to the bare Si measurement. The blue shift is consistent with the expected CTE mismatch stress in the Si substrate. The absence of a *T* dependence may be due to a combination of small stresses and the resolution limit of the instrument (0.05 cm^{-1} at best). The Si towers, however, show a much larger blue shift from the bare Si that increases linearly with RTA temperature (see Fig. 4.31b). Assuming the towers are under a biaxial stress from the CTE mismatch with the SiC coating, this blue shift represents a compressive stress of 0.8-2.8 GPa (see Fig. 4.32). This linearly increasing compressive stress agrees with the trends of both the prediction from elasticity (Eqn. 4.3) and extruded volume measurements on the FIB cut towers (see Fig. 4.27). However, the magnitude is 3-5 times larger than even the upper bound estimate assuming elastically deformed concentric spheres (see Table 4.2). This discrepancy will be addressed in future work (see Chapter 6).

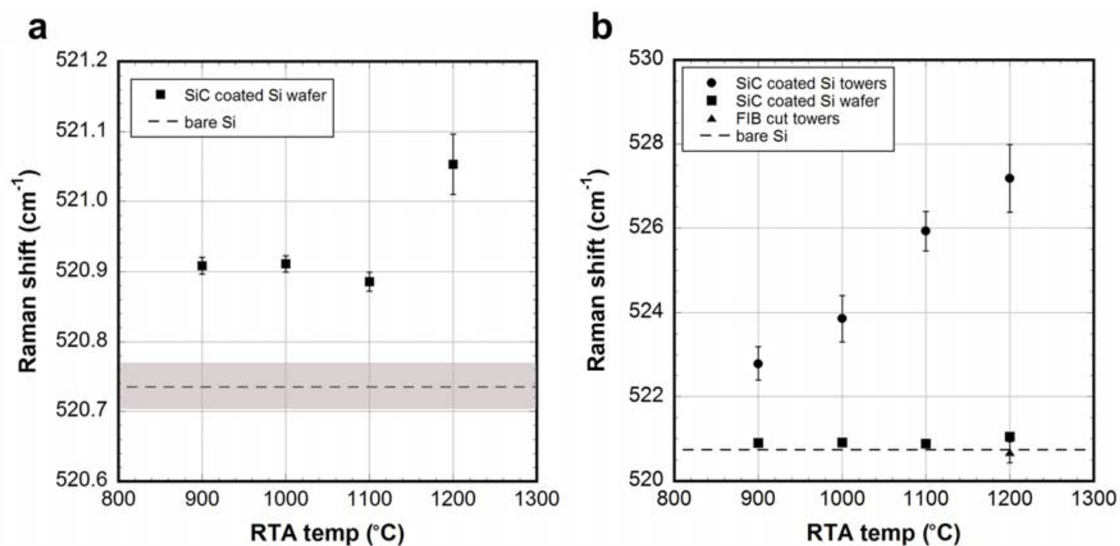

Figure 4.31 Average Raman shifts for the SiC coated Si, Si composite towers, and the bare Si(111) as a function of RTA treatment temperature. Error bars represent the standard deviation. For the bare Si, a shaded band is used instead.

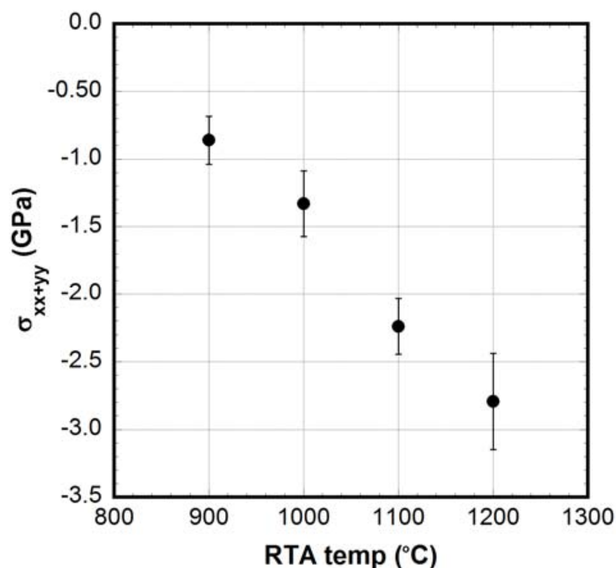

Figure 4.32 Biaxial stress in the Si towers as a function of RTA treatment temperature.

An alternative explanation for the blue shift is from carbon diffusion into the Si core from the SiC shell during RTA treatments and the formation of $Si_{1-x}C_x$ alloys [160-163]. The dependence of the Raman peak position for Si on the presence of carbon in substitutional locations was found to vary as:

$$\Delta\omega_{Si}\left(x\right)=\left(95\pm 20\right)x_C \qquad 4.8$$

where $\Delta\omega$ is the position change in the Si Raman shift in cm^{-1} and x_C is the atomic concentration of carbon [162]. Considering the Si tower data that was RTA treated to 1200°C, the blue shift of ~6.5 cm^{-1} (see Fig. 4.31b) would correspond to a 6.8% total carbon concentration. In addition to the blue shift, C impurities contribute two additional peaks to the Si spectrum, with one due to the local mode of C in Si at 604 cm^{-1} and a broad peak at 475 cm^{-1} [161]. Figure 4.33 shows the Raman spectra for a tower RTA treated to 1200°C. Since the relative intensity of the C-local mode peak is 1/10 of the Si peak at the estimated C concentration [161], the collection time was increased to 10 min (from 2 min in previous data). Note that sampling periods longer than 10 min are unreliable due to piezo drift in the Raman positioning stage. Using 10 min sampling, the silicon signal saturates the detector, as evidenced by the flat top of the peak in Fig. 4.33a. The data around the C-local mode (604 cm^{-1}) is magnified in Fig 4.33b and shows no evidence of an additional peak. To confirm that C diffusion into the Si core is not leading to the blue shift, spectra were collected on FIB cut towers that were RTA treated to 1200°C. These towers should be in a relaxed state, since any compressive stress from the RTA treatment would have been relieved through extrusion of the Si core. This set of data is shown in Fig. 4.31b (triangle) to lie at approximately

the same position as the bare Si wafer. If the blue shift was due to the presence of C in the Si core, it should be present after the RTA treatment regardless of whether the cap is present (FIB cut) or not. Since no shift is observed, this result strengthens the hypothesis that the observed blue shift in the capped towers is a result of a large compressive stress.

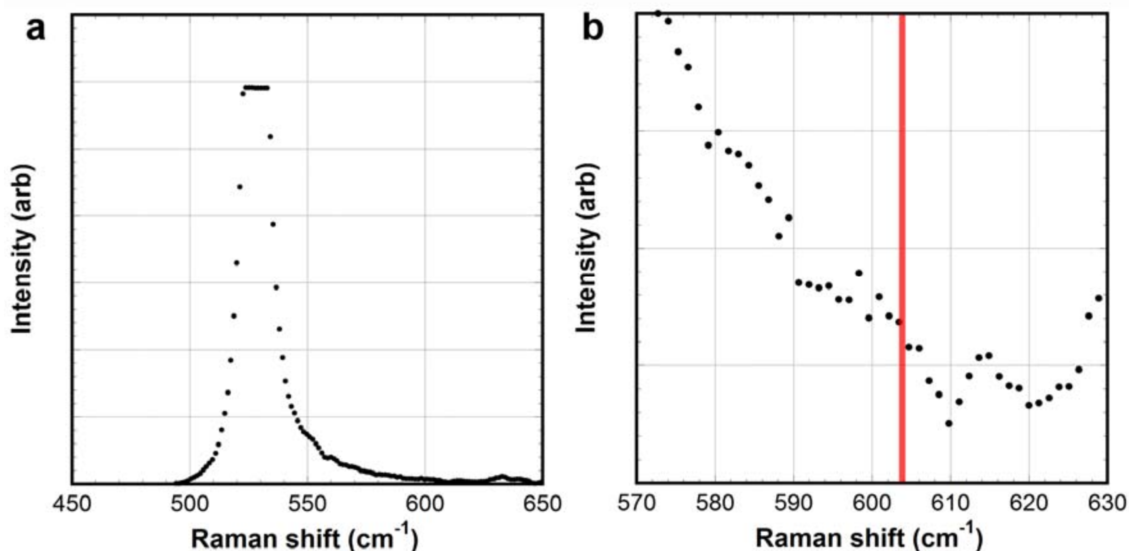

Figure 4.33 Raman spectra for a 1200°C RTA treated Si tower with a 10 min sampling time. The region where the C-local mode is located (labeled with a red line) is magnified in (b).

Additional evidence of a compressive residual stress can be found in DF TEM imaging. Fig. 4.34a shows an example of a nanotower from batch B in the as-deposited condition (no RTA treatment) and attached to the original VLS growth substrate. Oscillations in contrast originate from the base of the tower and show axial symmetry. In this case, the contrast is likely due to strain fields within the Si nanotower since thickness fringe effects would result in contrast lines parallel along the length of the

tower (as shown in Fig. 4.24) and there is no physical reason to expect bending in the free standing tower. Fig. 4.34b shows an example of strain contrast from Angelini et al. [164] for SiC whisker reinforced Al_2O_3, where the SiC whisker imaged at 600°C (top image) shows fewer contrast fringes than at 25°C (bottom image). Angelini showed that the spacing of contrast oscillations were proportional to the test temperature during *in situ* heating and thus were strain induced from the CTE mismatch between the whisker and matrix materials. A strain explanation in Fig. 4.34a would also be consistent with the Raman measurements, which showed strain within the tower and relaxation below the surface of the tower (see Fig. 4.30). Note that the appearance of strain contrast in this case and thickness contrast in Fig. 4.24 is likely due to a difference in the orientation of the diffraction vector, *g*, and the electron beam with respect to the tower.

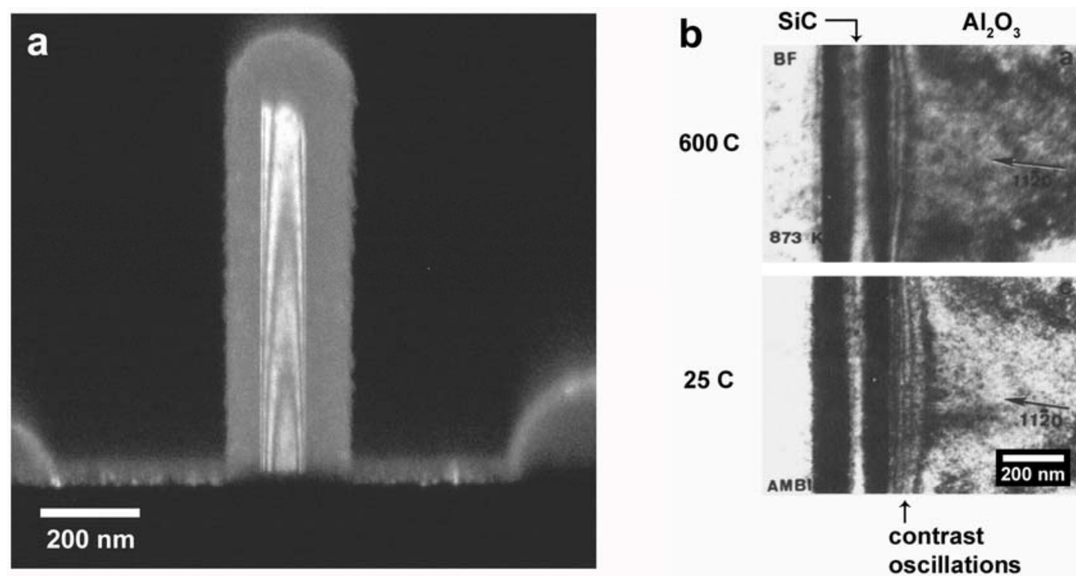

Figure 4.34 Two examples of strain contrast in TEM imaging. (a) From the current work, a DF TEM image of a composite tower from batch B, where the tower was imaged in the as deposited state (no RTA treatment) and is attached to the substrate. (b) BF TEM of SiC whiskers embedded in Al_2O_3 (adapted from Angelini et al. [164]), where the top image was taken at 600°C and the bottom at 25°C, showing strain relief (fewer fringes) as the temperature approaches the deposition temperature (1850°C).

4.9 Summary

This chapter focused on the role of thermal residual stresses in Si-SiC core-shell composites. These composites were created by depositing SiC films on VLS grown Si nanotowers. In composites where the Au catalyst was not etched off (batch A), FIB milled cross sections showed Au agglomerates at the Si/SiC interface and their subsequent diffusion towards the center of the Si nanotower during RTA heat treatments. At RTA temperatures of 1100 and 1200°C, porous regions were identified in the Si core and attributed to diffusion of Si interstitials to the FIB cut surface. While this problem of Au contamination in the batch A samples precluded any further stress

analysis with RTA treatments, *ex situ* indentation into the tower cross sections revealed a length scale dependent Si II→I phase transformation on unloading that agreed with transformations found in Si wedges [146] and bulk Si(111) wafers [135]. The SEM *in situ* indentation on batch A confirmed additional results from *ex situ* indentation showing rapid crack growth in the SiC shell due to the tensile residual stress. In the composites where the Au catalyst was etched away (batch B), three independent techniques (AFM height measurements of extruded Si, CRM stress measurements, and DF TEM) showed that the Si core was under a compressive residual stress due to the CTE mismatch with the SiC shell. While CRM measurements suggest that the compressive stress reached approximately 2.8 GPa after a 1200°C RTA treatment, the magnitude of this stress was greater than five times thermoelastic estimates and was not confirmed by an independent technique. If the magnitude of the CRM measured stresses are accurate, this result in conjunction with the increasing stability of the Si II phase found during indentation suggests that Si II can be held in a metastable state in the core-shell composites. This result is discussed in more detail in Chapters 5 and 6, along with its implications on toughening in Si-SiC composites.

Chapter 5: Uniaxial compression of Si nanospheres and towers

5.1 Overview

This chapter discusses the deformation of silicon nanospheres and nanotowers through TEM *in situ* nanoindentation experiments. These consisted of a series of uniaxial compressions of HPPD synthesized single crystal Si nanospheres (*d*=63-349 nm) on Al_2O_3 substrates and VLS grown Si(111) nanotowers (*d*=231-415 nm) from batch A (see Chapter 4 for details). Observations on the size dependence of strength and fracture toughness are adapted from 2010 publications in Scripta Mater. [165] and Philos. Mag. [166], respectively. The final section discusses the transition from phase transformation plasticity to dislocation plasticity dominated deformation at small length scales. The experiments in this chapter were in collaboration with O. Ugurlu (Characterization Facility, UMN) and J. Deneen (Hysitron Inc.), who operated the TEM.

5.2 Strength

Initial indentations of the Si nanospheres were run using Si(100) wedges as substrates. These substrates are similar to those used by Ge et al. [146] (Section 4.5.2), with a plateau width of 1 μm. The advantage of these substrates is that the nanospheres can more easily be imaged by tilting the stage without substrate interference. However, as will be shown, the substrates proved to be inadequate for Si nanosphere compression

due to yielding of the substrate prior to the sphere. Figure 5.1 gives an example of a 104 nm diameter Si nanosphere compression experiment on a 1 μm Si wedge. The initially defect-free sphere (Fig. 5.1a) was loaded smoothly up to the first arrow in Fig. 5.1c and then sunk into the substrate. The image after the indent (Fig. 5.1b) shows a darker contrast region below the sphere, which could be due to both strain in the Si substrate and a thickness effect from the newly imbedded Si nanosphere. Assuming a sphere of this size has a yield strength that is approximately two times larger than bulk Si [44], the majority of the deformation will be in the substrate rather than the Si nanosphere. Thus, the Si nanosphere can be considered a hard sphere indenting a flat surface and a Hertzian contact area (Eqn. 2.12, with an included factor of two since the equation was derived for a sphere being deformed between two plates) can be used to determine a contact stress of 9.0 GPa at the first arrow in Fig. 5.1c. This is within ~10% of what would be expected for the hardness of a Si(100) wafer [167] and confirms that a majority of the deformation is in the substrate rather than the particle. The deviation in the measured contact stress is likely due to the wedge geometry, as large shear stresses will develop at the plateau edges, leading to enhanced dislocation plasticity [140] and a decreased yield strength.

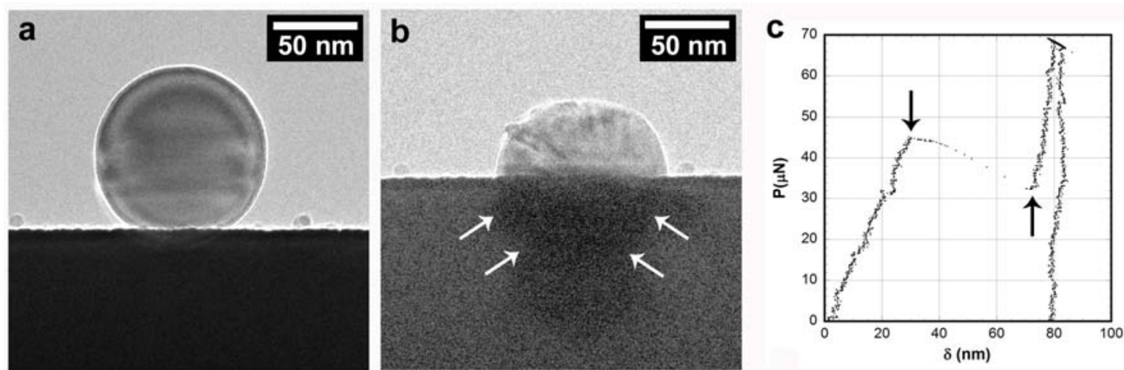

Figure 5.1 Si nanosphere (*d*=104 nm) indentation on a 1 μm Si wedge substrate, with TEM bright field (BF) images of the sphere before (a) and after (b) the indentation and the load-displacement data (c). Arrows in (b) indicate the darker contrast in the Si substrate while the arrows in (c) show the point during loading where the sphere sinks into the substrate (downward arrow) and where it begins reloading (upward arrow).

To avoid these complications from yielding in the Si substrates, the remainder of the Si nanosphere indentations were run on sapphire substrates (as discussed in Section 2.5.2.3). Spheres with diameters ranging from 63 to 349 nm were indented in displacement control, with 10 nm/s loading and unloading rates and a 5 sec hold at the peak load. Figure 5.2 gives images of a 173 nm sphere loaded five times (consecutively), with the corresponding load-displacement data in Figure 5.3. Following the first indent, there is little evidence of plastic deformation in the sphere, with the exception of a hemispherical region near the substrate (labeled with an arrow in Fig. 5.2b). Given the load-displacement curve (Fig. 5.3b) shows ~50 nm of residual displacement, this suggests a relaxation of the sphere and considerable reverse plasticity, which has been proposed previously for *ex situ* compressions of Si nanospheres [168]. In subsequent indents, there is significantly more deformation, as

evidenced by the darker contrast regions in Fig. 5.2 and the load drops in Fig. 5.3c-e. For indents (c, e, f), the nanosphere slides along the substrate, as shown by the abrupt increase in the load-displacement data after the initial contact (downward pointing arrows in Fig 5.3). Excluding the displacement due to sliding and using a geometric contact area (Eqn. 2.13), the flow stress increases from 7.7 GPa in (b) to 14.1 GPa in (d).

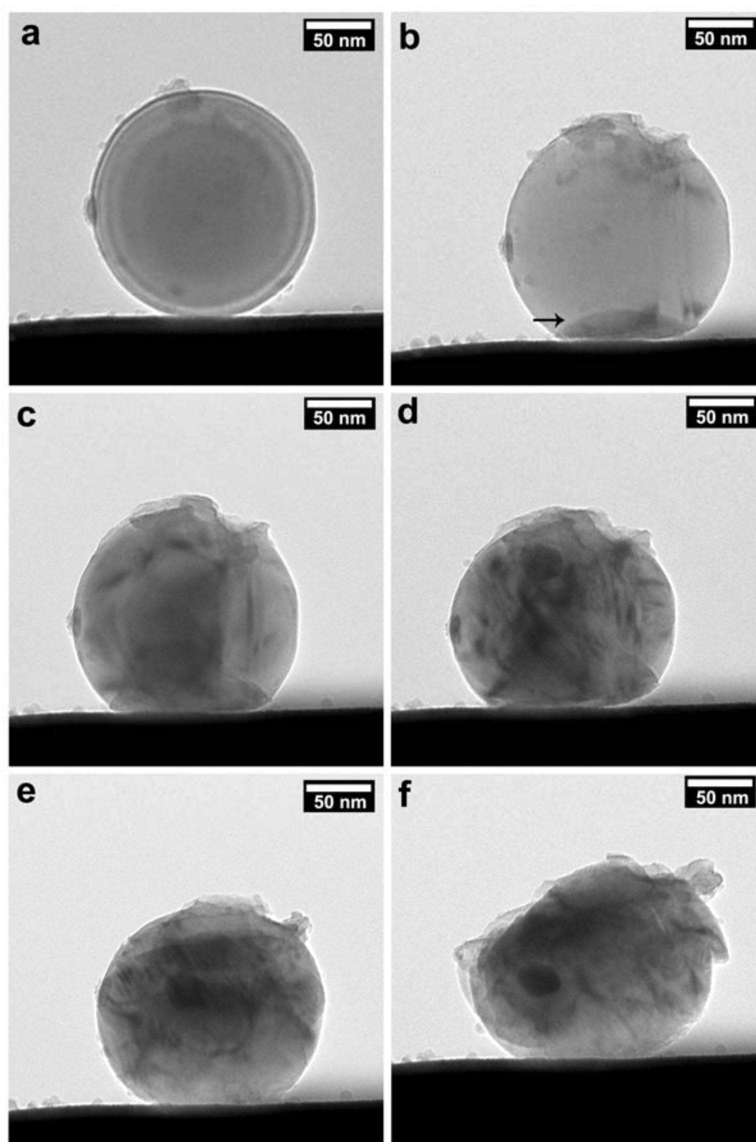

Figure 5.2 BF TEM images of a 173 nm diameter Si nanosphere before (a) and after (b-f) each of five consecutive indentations.

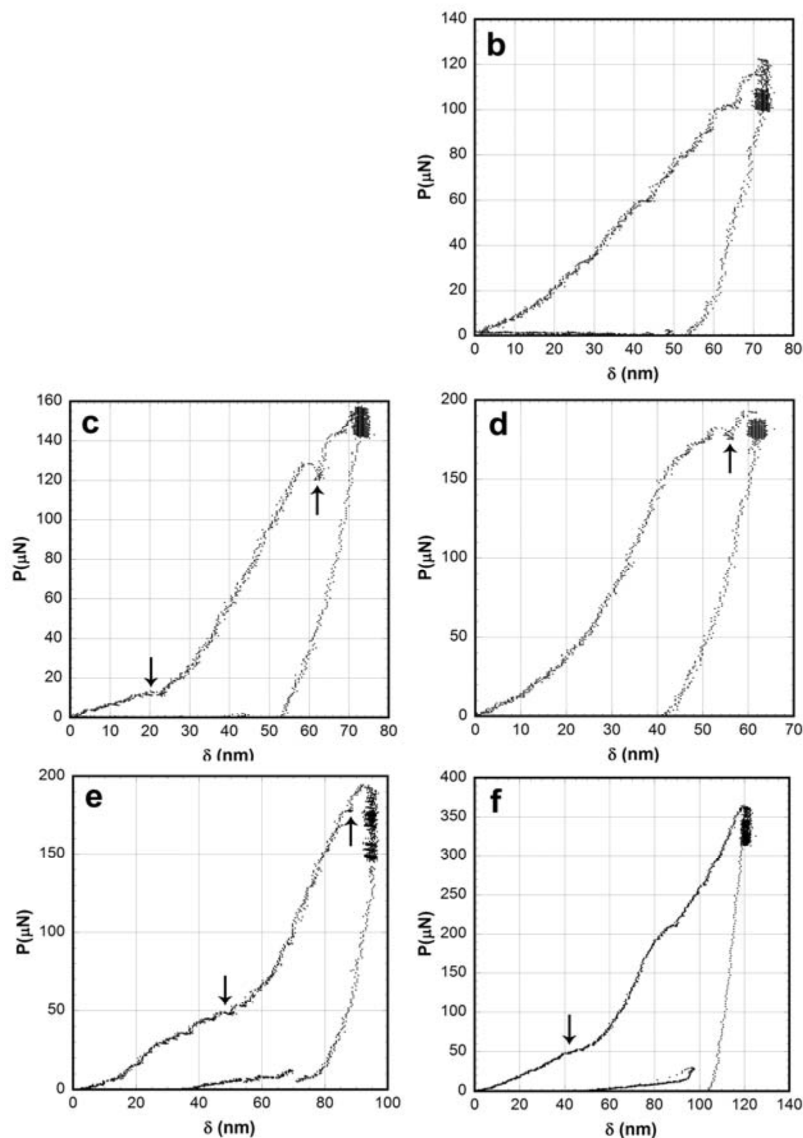

Figure 5.3 Load-displacement data for the 173 nm diameter Si nanosphere shown in Fig. 5.2. Vertical arrows indicate the position where the nanosphere stops sliding while the vertical arrow shows load drops in (c, d, e). Note there is no (a) so that the lettering matches Fig. 5.2.

This hardening effect can be explained by dislocation interactions or pile-up within the sphere internally and/or at the oxide shell. In thin films, oxide layers have

been shown to increase the critically resolved shear stress for dislocation nucleation [169]. In the nanospheres, the oxide prevents the release of dislocations and leads to the formation of a back stress due to dislocation pile-up. The applied shear stress, τ, needed to nucleate additional dislocations is thus increased and can be described by an Eshelby dislocation pile-up mechanism [170] as

$$\tau = \frac{\mu b N}{\pi (1-\nu) d} \tag{5.1}$$

where μ is the shear modulus, b is the Burgers vector, N is the number of dislocations, ν is Poisson's ratio, and d is the sphere diameter. Figure 5.4 shows the average flow stress as a function of diameter for nanospheres found using a geometric contact area (Eqn. 2.13). In addition, *ex situ* indentations of Si nanospheres are included from Mook et al. [45], where the flow stress was calculated based on an average between a geometric contact (Eqn. 2.13) and cylindrical contact (Eqn. 2.14). Assuming $\sigma_{flow} = 2\tau$ and using μ_{Si} = 60.5 GPa , b_{Si} = 0.235 nm, and ν_{Si} = 0.218 [171], a least squares fit of Eqn. 5.1 gives ~60 dislocations (see Fig. 5.4). Future work with *in situ* TEM will more explicitly give the number of slip planes and their back stress.

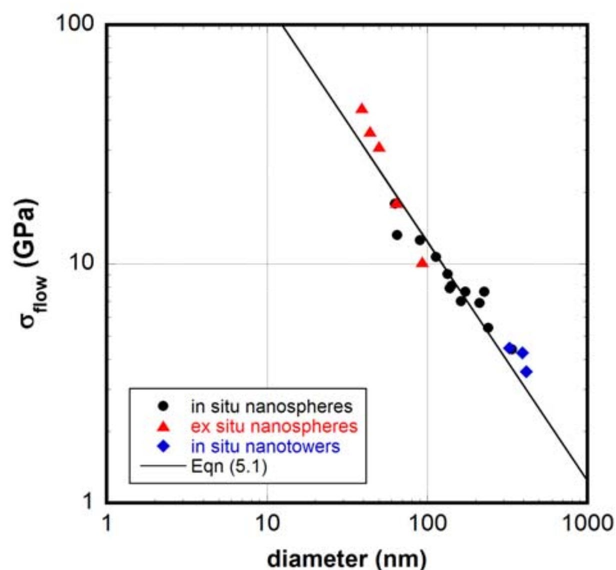

Figure 5.4 Flow stress, σ_{flow}, as a function of diameter for *in situ* compression of Si nanospheres and nanotowers in the current study and *ex situ* compression of Si nanospheres from Mook et al. [45].

Along with the Si nanospheres, a few *in situ* compression experiments were run on Si(111) nanotowers. These towers are the same towers described in Chapter 4 and referred to as batch A. Figure 5.5 shows before and after images of a representative Si nanotower indentation, with the indenter moving from top to bottom. As with the nanospheres, these experiments were run in displacement control with 10 nm/s loading and unloading and a 5 sec hold at the peak load. In this case, the 392 nm diameter tower was loaded up to ~500 μN (upward arrow in Fig 5.5c) and then fractured. Assuming a contact diameter equal to the tower diameter, this corresponds to a fracture stress of 4.3 GPa. This point and two additional towers are shown as blue diamonds in Fig. 5.4, falling closely along the d^{-1} strength dependence.

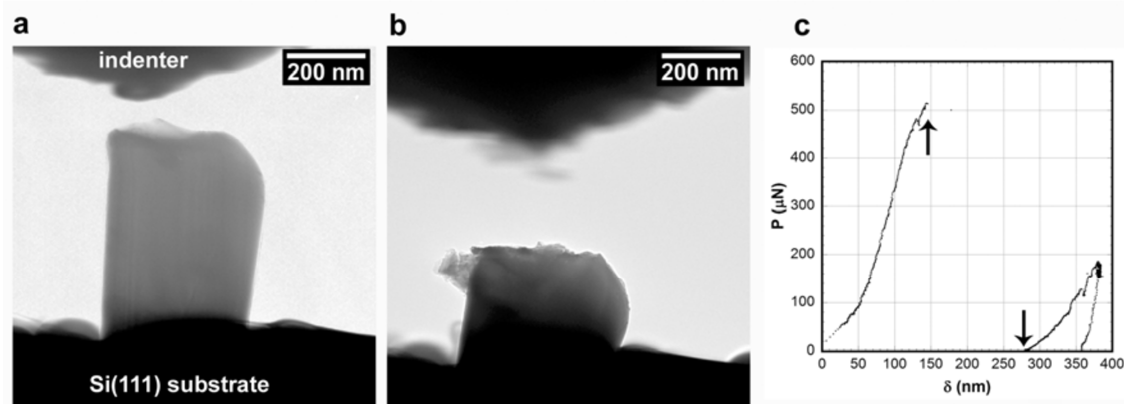

Figure 5.5 *In situ* compression of a 392 nm diameter Si(111) nanotower, showing the before (a) and after (b) images, along with the load-displacement data (c). The arrows in (c) indicate the point where the tower fractures (upward arrow) and the point where it is reloaded (downward arrow).

While the load-displacement data for the tower in Fig. 5.5 suggests a purely brittle fracture with negligible plasticity, further examination of the loading sequence reveals dislocation activity prior to failure. Figure 5.6 shows six frames (a-f) from the video capture of the compression, with 0.17 sec spacing separating the frames. The video was captured in bright field mode, with the contrast inverted in Fig. 5.6 to better reveal features within the tower. An arrow indicates the position of a white contrast band moving from the top of the tower downward from Fig. 5.6a-f. In Fig. 5.6e, a second contrast band appears and is indicated by a second arrow. As mentioned in the discussion of the Si-SiC composite towers (see Section 4.8), three possible explanations for the contrast during TEM imaging of the Si could be due to thickness, bending, or strain. Thickness effects can be immediately discarded since the thickness should only

vary along the diameter, not the tower length. Considering bending, the critical load for buckling in a fixed-free column from linear elasticity is given as [172]

$$P_{cr} = \frac{\pi^2 E I_z}{4L^2} \tag{5.2}$$

where E is the elastic modulus, I_z is the second area moment in z and is given as $I_z = \frac{\pi d^4}{32}$, L is the tower length, and d is the tower diameter. Using the known dimensions and $E_{Si}^{111} = 187\,GPa$ [88], the critical buckling load is ~3.7 mN. Since the tower failed at less than 1/7 the buckling load, failure by buckling (or even bending prior to failure) is unlikely. To evaluate whether strain is causing the contrast, the average downward velocity of the contrast band was measured. This was accomplished by measuring the change in position of the band with time from a fixed point. The average velocity of the first band shown in Fig. 5.6 was found to be 138 ± 110 nm/s. The large amount of uncertainty in this average is from the oscillation behavior of the indenter. Due to inadequate feedback controls and electrical noise in the transducer, the indenter has a sinusoidal motion superimposed over the prescribed indentation motion which creates a large spread in the measured contrast band velocity. Despite this large error, the measured velocity is much larger than the displacement rate of 10 nm/s. Elastic strain is proportional to the applied strain (displacement rate) and thus is unlikely the cause of the contrast.

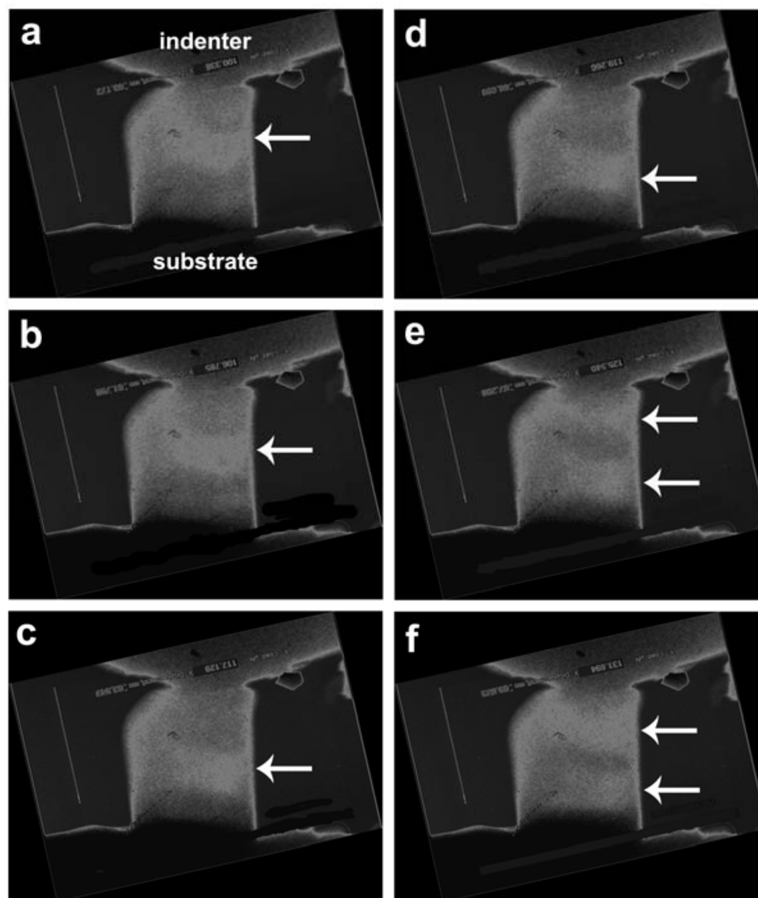

Figure 5.6 Video frames (0.17 sec spacing between each) showing the indentation of the tower from Fig. 5.5. The contrast is inverted and arrows have been added to highlight the motion of the bands from the top of the tower to the bottom. In images (e,f), a second arrow is added to identify a second contrast band.

Another possibility is dislocation motion. While room temperature dislocation plasticity in Si is generally thought to be minimal due to a high Peierl's barrier in Si [156], TEM analysis of indentation impressions showing plastically deformed regions [139, 173] and *in situ* observations of dislocation motion [140] have suggested that dislocation plasticity contributes to the deformation process, particularly in nanoscale objects with a high surface to volume ratio. In the present case, the appearance of a

broad band rather than a sharp line (as expected for dislocation contrast [174]) indicates that the observed motion is likely from a group of dislocations (rather than a single dislocation) possibly traveling in a Lüders band [156]. Further analysis of this observation, including an estimation of the activation energy and dislocation velocity, requires higher resolution TEM results and detailed crystallography, both of which are beyond the scope of this thesis. The importance of this finding, though, is that the towers show dislocation plasticity prior to fracture and that their size dependent strengthening may also be described by the previously mentioned dislocation pile-up mechanism used in Eqn. 5.1.

5.3 Toughness

Previous fracture studies with Si nanospheres by Mook et al. [45] and Deneen et al. [175] found an inverse length scale dependence on the nanosphere fracture toughness, with the toughness increasing for decreasing nanosphere diameters. However, both of these experiments were limited, in that Mook et al. needed to make indirect assumptions about the fracture event using *ex situ* scanning probe imaging techniques while the *in situ* compression experiments of Deneen et al. lacked load-displacement data to quantify the applied stress. In current work, Si nanospheres and nanotowers were fractured *in situ* with a quantitative measurement of the fracture stress. Indents were run in displacement control, with 10 nm/s loading and unloading rates and a 5 sec hold at the peak load. Five spheres (d=113-349 nm) and three towers (d=231-415 nm) showed signs of fracture at failure. Figure 5.7 gives a representative example

of the fracture of a 349 nm diameter Si nanosphere on an Al_2O_3 substrate. In addition to the before (a) and after (b) imaging of the particle, Fig. 5.7c shows a frame capture from the video immediately after the fracture. As expected, the crack growth process is much too rapid to capture on video (30 fps), with the frame prior to fracture showing no signs of crack initiation. Note in the load-displacement data, the fracture event (indicated with a vertical arrow in Fig 5.7d) occurs before the target displacement, leading to further loading by the indenter after the fracture (horizontal arrow in Fig 5.7d).

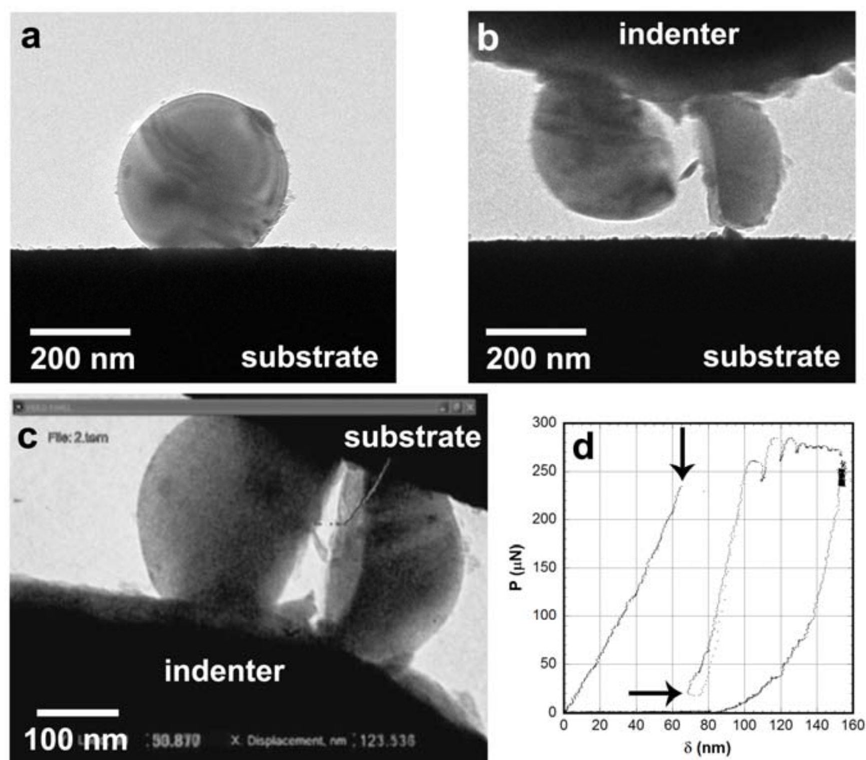

Figure 5.7 *In situ* fracturing of a 349 nm diameter Si nanosphere on an Al_2O_3 substrate. (a) and (b) show the nanoparticle before and after the indentation, respectively. A frame from the video capture immediately after the fracture event is shown in (c) while (d) is the load-displacement data. The vertical arrow indicates the point where the sphere fractures and the horizontal arrow shows where the fractured sphere was reloaded.

The previously mentioned nanosphere compression work [45, 176] assumed an initial crack length equal to the oxide thickness (typically 1-2 nm) to estimate the nanosphere fracture toughness. In the current work, a work per unit fracture area method was used since it accounts for dislocation plasticity and closely matches finite element modeling of the fracture toughness in Si nanotowers [41]. Figure 5.8 shows schematic representations of this concept, with the volume of material deformed and the new surface area created during the fracture process (indicated with hash marks).

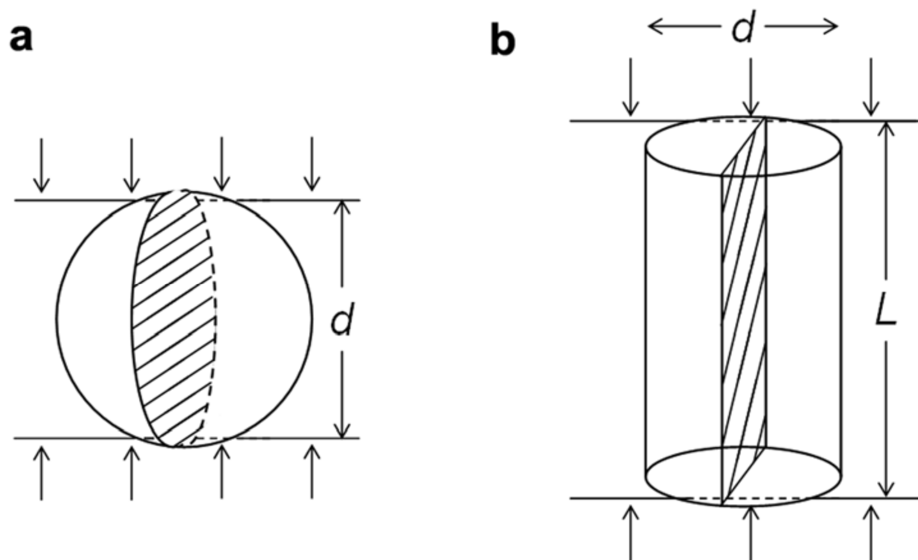

Figure 5.8 Work per unit fracture area schematics for spheres of diameter *d* (a) and towers of height *L* and diameter *d*. The hashed region represents the fracture area, *A*.

The work, *W*, applied to cause yielding in each case can be represented as the volume of deformed material, *V*, times the strain energy density:

$$W = V \cdot \int \sigma d\varepsilon \quad . \tag{5.3}$$

Assuming minimal plasticity prior to fracture, the stress (σ) and strain (ε) in the strain energy density can be defined as

$$\sigma_{ys} = \frac{k}{d} \tag{5.4}$$

$$\varepsilon = \frac{\sigma_{ys}}{E} \tag{5.5}$$

where Eqn. 5.4 is a simplified form of Eqn. 5.1, with material constants combined in a constant k, σ_{ys} is the yield stress, and E is the elastic modulus. Combining Eqns. (5.3-5), the work to deform the material is given as

$$W = V \cdot \frac{k^2}{d^2 E} \quad . \tag{5.6}$$

In the case of the nanosphere, Eqn. 5.6 becomes

$$W = \frac{4}{3}\pi\left(\frac{d}{2}\right)^3 \cdot \frac{k^2}{d^2 E} = \frac{2\pi d k^2}{3E} \quad . \tag{5.7}$$

Using the area indicated in Fig. 5.8a and assuming plane stress (no Poisson's ratio effect), this gives a strain energy release rate, G_{Ic}, and fracture toughness, K_{Ic}, of

$$G_{Ic} = \frac{W}{A} = \frac{8k^2}{3dE} \tag{5.8}$$

$$K_{Ic} = k\left(\frac{8}{3d}\right)^{1/2} \tag{5.9}$$

Similarly, for the nanotower, Eqn. 5.6 becomes

$$W = \frac{\pi d^2}{4} L = \pi d^3 \tag{5.10}$$

where the length of the tower is assumed to equal 4*d* to avoid buckling. Again, using the area indicated in Fig. 5.8b, this gives a strain energy release rate and fracture toughness of

$$G_{Ic} = \frac{W}{A} = \frac{k^2 \pi}{4dE} \tag{5.11}$$

$$K_{Ic} = k\left(\frac{\pi}{4d}\right)^{1/2} \quad . \tag{5.12}$$

Note that both Eqns. 5.9 and 5.12 give an inverse square root dependence on the diameter. Figure 5.9 summarizes the fracture toughness for the nanospheres and nanotowers as calculated from the Eqns. 5.9 and 5.12, along with *ex situ* nanosphere results from Mook et al. [45].

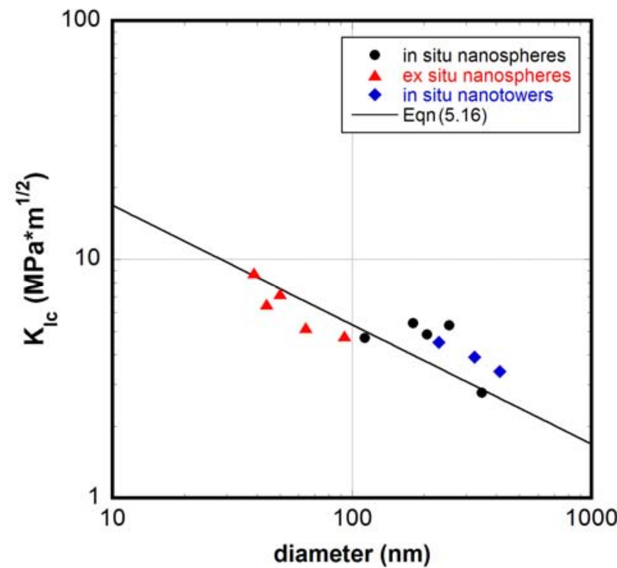

Figure 5.9 Fracture toughness, K_{Ic}, as a function of diameter for *in situ* compression of Si nanospheres and nanotowers in the current study and *ex situ* compression of Si nanospheres from Mook et al. [45].

While the work per unit fracture area method is based on linear elasticity, a similar length scale dependence can be shown using a dislocation shielding argument [171, 177]. Assuming limited plasticity, the crack extension force, G_{IIc}, can be equated to the dislocation resistive force, F_R. Under mode II loading, the strain energy release rate is

$$G_{IIc} = \left(1-\nu^2\right)\frac{K_{IIc}^2}{E} \tag{5.13}$$

where K_{IIc} is the mode II fracture toughness. The dislocation resistive force is given in terms of the dislocation line tension as [178]

$$F_R = N\tau b \tag{5.14}$$

where N is the number of dislocations prior to crack extension, τ is the resolved shear stress, and b is the Burgers vector. Combining Eqn. 5.13 and 5.14 and using $K_{Ic} \approx \left(\frac{2}{\sqrt{3}}\right)K_{IIc}$ [179] gives

$$K_{Ic} = \frac{10}{9}\left(\frac{N\mu\sigma_{ys}b}{1-\nu}\right)^{1/2} \tag{5.15}$$

where σ_{ys} is the yield strength and ν is Poisson's ratio. Eqn. 5.1 can then be used to relate Eqn. 5.15 to the sample diameter. With ν_{Si}=0.218 and taking yield strength as the maximum value from Fig. 5.4, Eqn. 5.15 becomes

$$K_{Ic} = \frac{10}{9}\mu N b d^{-1/2} \quad . \tag{5.16}$$

Eqn. 5.16 is shown in Fig. 5.9 as a solid line, with the same number of dislocations (N=60) as determined in Fig. 5.4. As with the strengthening argument proposed earlier,

this result suggests that dislocations trapped in small volumes generate large back stresses and increase the yield strength. In addition, the piled up dislocations will act to shield the crack tip and inhibit crack growth, thus increasing the material toughness.

5.3 Phase transformations

As was the case for the *ex situ* indentations of the FIB milled Si/SiC towers (Section 4.5.2), the *in situ* indentation of Si nanospheres occasionally showed elbows during unloading. Figure 5.10 shows an example of this response for a 212 nm diameter sphere, where a power law fitting is included in the unloading data (red line, Fig. 5.10c) to highlight the deviation from a purely elastic-plastic response. Figure 5.11 summarizes the elbow transition pressures for nanospheres ranging from 134 to 227 nm as a function of the critical dimension (in this case, diameter), along with the data from Fig. 4.16. The nanosphere data corroborates the logarithmic decay in the transition pressure as a function of critical dimension found for the Si nanotowers (confined in a Si/SiC composite), wedges [146], and bulk Si [135]. In addition, it also gives more credibility to the trend at smaller dimensions, suggesting that as the critical dimension approaches ~100 nm, the reverse phase transformation on unloading (Si II → a/III/I) is no longer observed. None of the spheres that were close to or below this dimension showed an elbow on unloading, including those spheres indented *in situ* as part of this study (*d*=63, 65, 90, and 104) or those indented *ex situ* by Mook et al. [45, 180] (*d*=39-93 nm).

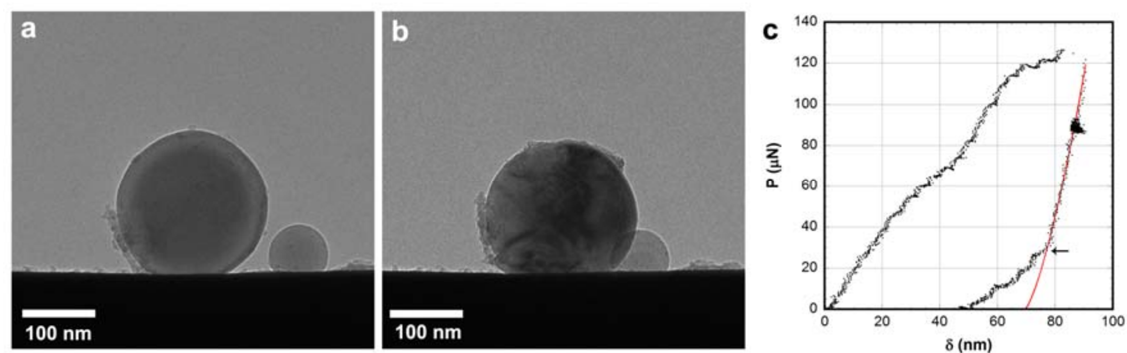

Figure 5.10 *In situ* compression of a 212 nm diameter Si nanosphere, showing BF TEM images before and after the indentation images (a,b) and the load-displacement curve with a power law fitting to the unloading curve (red line).

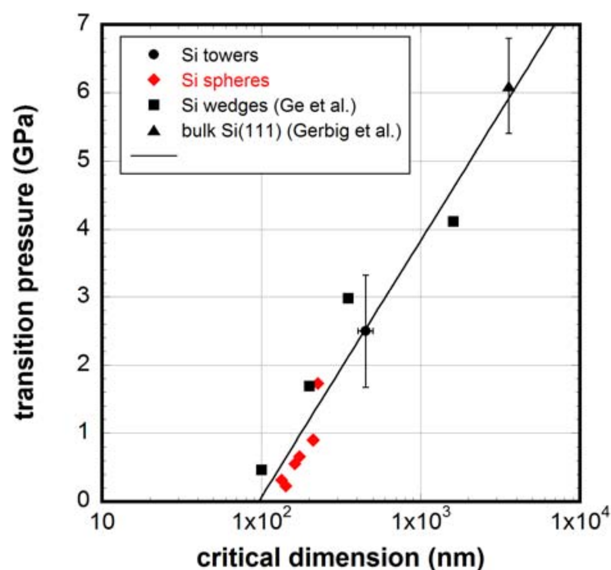

Figure 5.11 Transition pressure on unloading as a function of critical dimension. *In situ* results from the Si nanospheres (diameter) are added to data from Fig. 4.16, which included Si towers (diameter), Si wedges (plateau width) [146], and bulk Si(111) [135]. A logarithmic fit is given as a guide to the eye.

Two possible explanations for the absence of a phase transformation at critical dimensions less than 100 nm are either that the transformed Si II remains in a metastable state under atmospheric conditions or there is an absence of the Si I→II transformation on loading, thus precluding any reverse transformation. While Si II has been observed at relatively low hydrostatic pressures (~1.5 GPa) under low temperatures (100 K) [181], there is no evidence in the literature showing stable Si II at ambient conditions. The direct identification of the presence/absence of a Si I→II transition on loading was not possible in the current data, since there were no distinct pop-in events during indentation loading and the technique of multiple partial unloading [182], which is used to more conclusively identify phase transformations during loading, was not employed. However, the absence of the transition is plausible given the combined effects of dislocation plasticity and phase transformation plasticity during loading. As was shown earlier, the shear stress required to nucleate dislocations increases in small volumes due to a dislocation pile-up mechanism. In addition, there is also a length scale effect associated with the phase transformation. This is most clearly demonstrated, independent of dislocation plasticity effects, under quasi-hydrostatic loading conditions in diamond anvil cell experiments. Tolbert et al. [138] found the Si I→II transition for sc-Si nanospheres (d =10-50 nm) to be at a hydrostatic pressure of 22 GPa. This is approximately twice the pressure (11.3-12.5 GPa) found for the bulk transformation of Si under hydrostatic conditions [137]. Based on Eqn. 5.1 (as fitted to the data in Fig. 5.4), a 30 nm diameter sphere would have a flow stress of approximately 41 GPa. Thus, the nanospheres studied by Tolbert were likely loaded

nearly elastically before transforming to Si II at 22 GPa. Unfortunately, the size dependent phase transformation during hydrostatic loading at length scales between Tolbert's study and bulk samples has not been studied.

During indentation or uniaxial compression, in addition to dilatational stresses, there will be significant deviatoric contributions to the loading [111], leading to enhanced dislocation nucleation [183] and a decreased threshold for phase transformation [144, 184]. Page et al. [173] recognized that the deformation response of Si under indentation is governed by the magnitude of the hydrostatic and deviatoric components of the stress tensor relative to critical stresses for densification and dislocation plasticity, respectively. For shallow indents into Si(001) wafers, high hydrostatic pressures (10-20 GPa) immediately below the indenter are sufficient to trigger a phase transformation. At these depths, the resolved shear stress is below its critical value, resulting in minimal dislocation plasticity and a phase transformation dominated response. For the data given in Fig. 5.11, the sample geometries and loading conditions lead to enhanced contributions of the deviatoric stress components over the dilatational stresses. The wedge samples [146], particularly at the larger widths (350, 1600 nm), behave similarly to bulk Si, with large hydrostatic stresses beneath the tip leading to a phase transformation dominated response at small depths. At smaller widths, while the characteristic elbow suggests a phase transformation is still occurring, there is an increasing contribution from the shear stresses at the plateau edges [140]. In the uniaxial nanosphere compressions, the deformation will be controlled by the nucleation of dislocation loops at the sphere-indenter contact points due to high local

shear strains [44]. This interpretation is in conflict with MD simulations that suggest a phase transformation occurs in the center of Si nanospheres (*d*=20 nm) under unaxial loading [142]. However, this may be an artifact of the interatomic potential (Tersoff), which has limited success in predicting dislocation plasticity [185]. Finally, in the uniaxial compression of the SiC confined Si towers, dislocation plasticity will be dominant due to the superposed CTE mismatch shear stresses (Eqn. 4.5) at the center of the tower disrupting what would be expected to be a largely hydrostatic indentation stress. Therefore, while phase transformation plasticity may occur at dimensions smaller than 100 nm for purely hydrostatic loading, the increasing importance of local shear strains during the anisotropic loading of small sample geometries (particularly with low angle interfaces) for decreasing diameters can cause dislocation plasticity to dominant the deformation response.

5.4 Summary

A series of TEM *in situ* indentation experiments were run on Si nanospheres and nanotowers to probe the deformation of Si at small scales. Both the flow stress and fracture toughness of Si were shown to increase with decreasing sample diameter, with $\sigma_{flow} \propto d^{-1}$ and $K_{Ic} \propto d^{-1/2}$. These were described theoretically using a dislocation pile-up mechanism in the case of the flow stress and dislocation shielding for the fracture toughness. Finally, the importance of the entire stress tensor, not just the hydrostatic components, in the phase transformation from Si I→II was demonstrated by selecting

geometries and loading conditions that promoted the formation of high shear strains. While not conclusive, this result suggests a fundamental change in the deformation mechanism of Si to a dislocation plasticity dominated response for critical dimensions less than ~100 nm.

Chapter 6: Conclusions and future direction

6.1 Summary

The focus of this dissertation has been on the development of materials with a high wear resistance. This goal was refined in Chapter 1 as making more ductile ceramics that demonstrated both high yield strength and fracture toughness. In the chapters that followed, experimental work investigated the role of thermal residual stresses and nanoscale confinement on fracture. This included the development of a hybrid deposition mechanism for SiC film deposition (Chapter 2) and the deposition and fracture analysis of SiC based nanocomposites (Chapter 3, 4). The length scale dependent strengthening and toughening of Si nanostructures was studied using TEM *in situ* measurements (Chapter 5), along with a proposal for a transition in the deformation of Si under anistropic loading below a critical size (Chapter 4, 5). This work is described in more detail below.

An important development early in this dissertation research that helped facilitate much of the subsequent work was an understanding of a hybrid growth mechanism during hypersonic plasma particle deposition (HPPD). HPPD was originally developed as high rate deposition technique for nanocrystalline films that relied on the nucleation and ballistic impaction of aerosolized nanoparticles. By recognizing spatial variations in the coating morphology, growth orientation, and indentation hardness, a hybrid growth mechanism was proposed that incorporated chemical vapor deposition (CVD) to nanoparticle ballistic impaction. This suggested that a stagnation layer

containing reactant vapor at the substrate provides a uniform source for CVD growth while the concentration of impacted nanoparticles decays radially outward from the substrate center due to the impaction cut-size [66]. Near the center of the deposition, particle impaction dominates the growth, leading to high growth rates (~2 μm/min). However, these regions show high porosity and roughness (RMS roughness ~100's of nm) due to inefficient packing of nanoparticles into a cohesive film. At positions further away from the center, the extent of CVD growth increased, giving a slower growth rate (~30 nm/min) yet a more dense and smooth film (RMS roughness ~3 nm). This allowed for the deposition of dense, uniform coatings for multilayer structures (Chapter 3) and core-shell nanotowers (Chapter 4).

Using HPPD SiC coatings, the role of thermal residual stress in thin films and core-shell composites was studied during fracture events. Multilayer films consisting of SiC and Ti-based layers showed enhanced ductility in the SiC layers due to the presence of Ti inclusions. These inclusions were identified through cross sectional EDS imaging and were attributed to interlayer diffusion during the deposition due to high substrate temperatures (900-1000°C). During indentation, cracks initiated at the vertices of the indenter consistently tended toward and arrested in these Ti inclusions, demonstrating both a ductile phase bridging interface [26] and a residual stress induced hoop tension in the SiC. Consequently, the SiC layers showed improved wear resistance during scratch testing compared to monolithic SiC and an improved wear resistance ratio (H^3/E^{*2}) compared to superhard nanocomposites. However, indentations penetrating multiple layers of the film suffered from interlayer delamination and crack penetration into

neighboring layers depending on the state of stress at the interface. This suggests the multilayer structure as a whole faces significant limitations. Further analysis of interlayer residual stress was performed on SiC thin films on Si(100) substrates. Due to the coefficient of thermal expansion (CTE) mismatch of SiC/Si, tensile residual stresses were generated in the SiC films and were shown to be linearly dependent on rapid thermal annealing (RTA) heat treatment temperatures through enhanced crack growth.

A cylindrical or spherical core-shell structure avoids the adverse effects of planar stresses within the thin films by localizing the residual stress. In Chapter 4, SiC coatings were deposited on vapor-liquid-solid (VLS) grown Si(111) nanotowers to form core-shell composites. The CTE mismatch between the SiC shell and Si core leads to a compressive stress on the Si core, as evidenced by AFM height measurements of extruded Si, confocal Raman microscopy (CRM) stress measurements, and dark field (DF) TEM strain contours. CRM measurements suggest that the compressive stress reaches approximately 2.8 GPa after a 1200°C RTA treatment. However, this measurement was not confirmed by an independent technique and is much larger than what is predicted by thermoelastic theory (~300-500 MPa). Using SEM *in situ* indentation, unstable crack growth and fragmentation of the SiC shell was observed, suggesting high tensile stresses within the coating.

The final part of the dissertation considered the length scale dependent deformation of Si nanostructures in Chapter 5. Both HPPD synthesized Si nanospheres and VLS grown Si(111) nanotowers were compressed uniaxially inside the TEM. Using estimates of contact area proposed by Mook et al. [45], the flow stress was found to

increase as $\sigma_{flow} \propto d^{-1}$. This trend agrees with data from *ex situ* indentation experiments on Si nanospheres [45] and can be explained based on an Eshelby dislocation pile-up mechanism [170]. The fracture toughness of the nanospheres and nanotowers was evaluated using a work per unit fracture area approach, with an increasing toughness at smaller diameters ($K_{Ic} \propto d^{-1/2}$). This increase in toughness also agreed with previous *ex situ* measurements [45] and is consistent with dislocation shielding at the crack tip [171]. Finally, the role of phase transformations during the deformation of Si was found to change below a critical dimension of ~100 nm. This was first observed for *ex situ* indents into cross sectioned Si-SiC composite towers in Chapter 4. These indents showed an increased stability of Si II at smaller contact stresses than observed for bulk Si(111) based on deviations from elastic-plastic unloading. Together with data for Si wedges [146] and bulk Si(111) wafers [135], this result (Fig. 4.16) showed for the first time a length scale dependent Si II→I phase transformation. This trend was shown more convincingly with the addition of data from *in situ* compression data for Si nanospheres (Fig. 5.11). In addition to showing an increase in the stability of Si II at lower stresses, this result also suggests the disappearance of the Si I→II at a critical dimension of ~100 nm. The reason for this transition is the increasing role of shear stresses during indentation for the small sample geometries compared to bulk samples. This is essentially the counterpart to the indentation pressure effect proposed by Mook et al. [45], which focused on the role of hydrostatic pressure during indentation. In the nanospheres and wedges [146], the deviatoric components of the stress tensor exceed the critically resolved shear stress prior to a hydrostatic stress needed for densification.

Thus, the deformation of small volumes of Si is dominated by dislocation plasticity rather than phase transformation plasticity.

Considering the increased stability of Si II (Chapter 5) together with the high compressive stresses found in the Si–SiC core–shell composites (Chapter 4), a new toughening mechanism for Si–SiC nanocomposites is proposed as follows and shown schematically in Fig. 6.1. First, Si I nanospheres with diameters in the range of 100-1000 nm are dispersed in a SiC matrix and heat treated to 1100-1200°C (Fig 6.1a). Based on Fig. 4.31, this will leave the Si nanospheres under a compressive stress of close to 3 GPa. The composite is then loaded to a stress exceeding the critical stress needed for the Si I→II transition (~8-10 GPa). This can be done either under service conditions or by pre-stressing the composite. Upon unloading, the nanospheres will remain as Si II based on Fig. 5.11. When a crack forms in the composite (Fig. 6.1c), the tensile stress at the crack tip will destabilize the Si II and cause a transformation back to Si I. The volume expansion during this transformation will then act as a compressive stress to close the approaching crack (Fig. 6.1d), in same way transformations in PSZ have been shown to cause crack closure [28, 29]. If the tensile stress at the crack tip does not transform the Si II, the Si II nanospheres will act as either ductile inclusions for crack pinning or form voids due to the Si I→II contraction that will serve as crack arrest points (Fig. 6.1e). Thus, by controlling the length scale of the Si nanospheres, Si–SiC nanocomposites can be toughened by a combination of phase transformation and ductile phase reinforcement mechanisms.

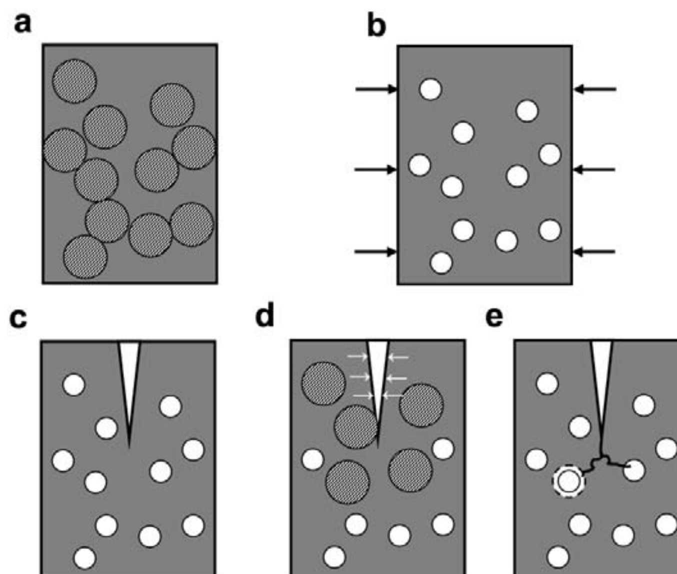

Figure 6.1 Schematic representation of a proposed toughening mechanism for Si embedded SiC. (a) Si I nanoparticles (hashed circles) are dispersed in a SiC matrix (grey), (b) Si I→II phase transformation (and volumetric contraction) during loading conditions in service, (c) crack formation, (d) Si II→I phase transformation (and expansion) from the tensile stress at the crack tip and subsequent compressive stress on crack tip due to phase transformation, and (e) the crack arrests in voids from particle contraction or ductile pinning in Si II particles. Arrows in (b,d) indicate a compressive stress.

6.2 Future work

In the short term, experiments are needed to validate the magnitude of the compressive stress on the Si core using techniques such as quantitative strain contrast measurements in DF TEM. A follow-up experiment would then be to determine if the Si II under biaxial compression is stable following indentation, either by CRM (as described in Chapter 4) or selected area diffraction (SAD) in the TEM. The following experiment could test the effectiveness of the proposed phase transformation

toughening mechanism. First, RTA treat the composite tower to induce a compressive stress ~2-3 GPa (Fig. 6.2a), then load the tower uniaxially to a hydrostatic stress greater than the critical stress for densification (Fig. 6.2b), and finally pre-crack the SiC coating using the focused ion beam (FIB) and reload the tower to induce mode I fracture (Fig. 6.2c). While this experiment could be performed in either the SEM or TEM *in situ* indenters, a TEM based experiment would be have the added benefit of imaging any dislocation activity in the Si core (ideally to confirm any crack tip shielding) and also to monitor the Si phase using SAD.

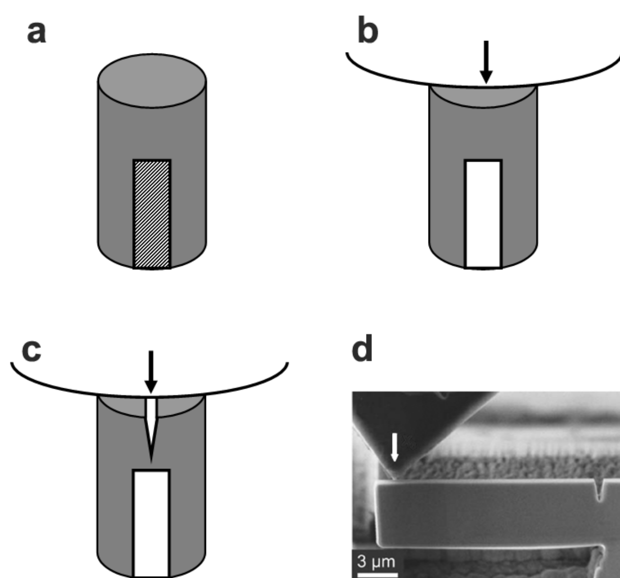

Figure 6.2 Schematic of the proposed experiment to test the phase transformation toughening mechanism, showing (a) the composite tower after a RTA treatment with Si I (marked with diagonal hashes) in the core, (b) the Si I→II (in white) phase transformation under indentation loading, (c) the same tower reloaded with a FIB pre-crack notch, and (d) an example of a FIB pre-crack notch ($r_{notch\ tip}$~100 nm) used in a indentation bending fracture experiment with Mo [38].

The next step in the development of ductile ceramics would be to take the concept of localized residual stress as demonstrated in the Si-SiC core-shell composite and scale it up to a coating. Two sets of experiments were initiated with this goal in mind using the HPPD system. In the first set of experiments, the goal was to simultaneously grow VLS Si nanotowers and the surrounding SiC matrix in the HPPD system. First, hexagonal arrays of Au nanoclusters were deposited on Si(111) substrates [186] by a collaborator, M. Bechelany, at EMPA (Swiss Federal Laboratories for Material Testing & Research, Thun, Switzerland). Using the same experimental conditions discussed in Chapter 2 for SiC deposition, films were deposited on the Au patterned Si(111). An example of one of the patterned substrates and deposited films is shown in Fig. 6.3a,b. By tilting the film to 45°, the hexagonal structure is observed in the film, with raised regions (topographical) where the Au clusters would be expected. However, subsequent analysis was unable to confirm the composite structure of the film, particularly whether it was composed of Si towers embedded in a SiC matrix. Further experiments using only $SiCl_4$ (no CH_4) were unable to demonstrate preferred VLS growth at the Au clusters. This is likely due to the strong temperature dependence on VLS growth [53] and Au surface migration during the deposition process [128].

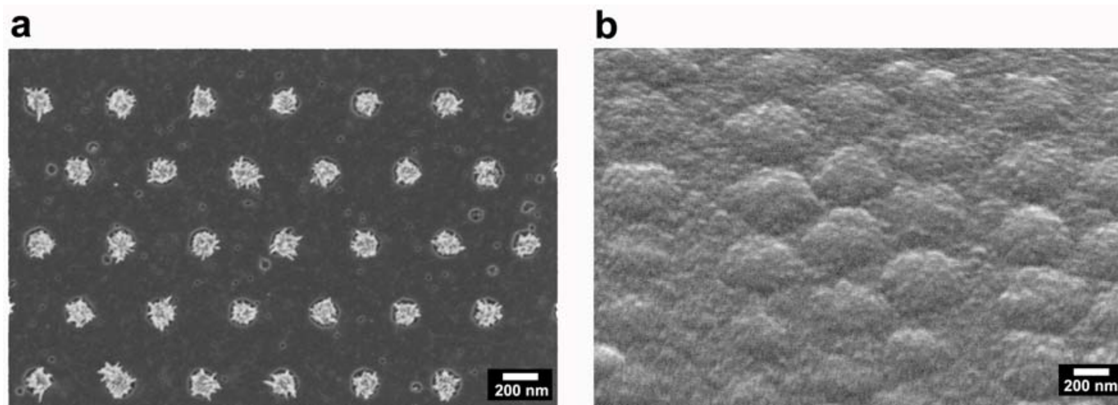

Figure 6.3 Si-SiC composite growth from Au patterned Si(111) substrates, with (a) showing the hexagonally arranged Au clusters and (b) showing the film following Si/C deposition (45° tilt).

The second set of experiments attempted to move from a core-shell composite to an embedded particle composite. This involved the development of a dual nozzle deposition system shown in Fig. 6.4a. Using the same inner contour design as the single nozzle (Chapter 2), a second nozzle was added and the plasma jet was split at a Y-junction just downstream of the anode. By splitting the flow, two independent sets of reactants could be injected in each nozzle and deposited simultaneously. Figure 6.4b shows preliminary results of a film deposited on a Mo substrate. The top region was deposited from a nozzle with $SiCl_4$ and CH_4 while the bottom region was from the second nozzle with $TiCl_4$. The clear separation of the two coatings suggests that there was relatively little mixing of the gas streams during the deposition. However, Fig. 6.5 shows an example of nanowire growth on the Ti-based side of the deposition. These structures are similar to those observed previously in HPPD grown Si nanowires and may be due to catalyzed growth from $TiSi_2$ as suggested by Hafiz et al. [71]. While this

suggests some degree of mixing (either in the gas phase or on the surface), future experiments could study the impact of substrate rotation in forming a well-mixed 2-phase composite structure. One drawback with the dual design, though, is erosion of the boron nitride (BN) nozzle due to high temperatures at the stagnation point where the flow is split (Y-junction). This could lead to contamination from BN debris in the films.

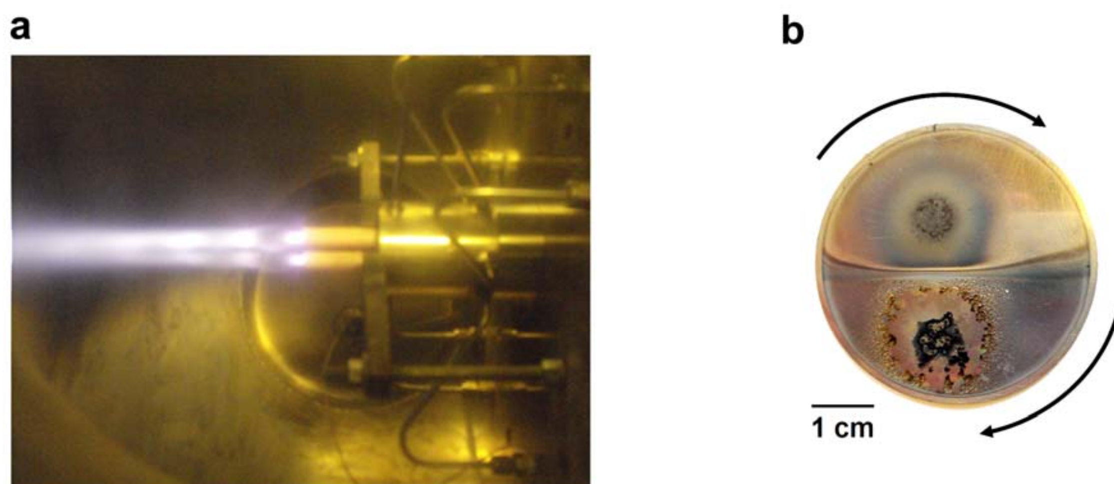

Figure 6.4 Codeposition of two independent reactant species using a dual nozzle design. (a) Dual nozzle setup running with 30 slm Ar and ~9 kW (no reactants) and (b) deposition of SiC (top) and Ti (bottom) on a Mo substrate. Arrows suggest the potential for phase mixing by rotating the substrate during the deposition.

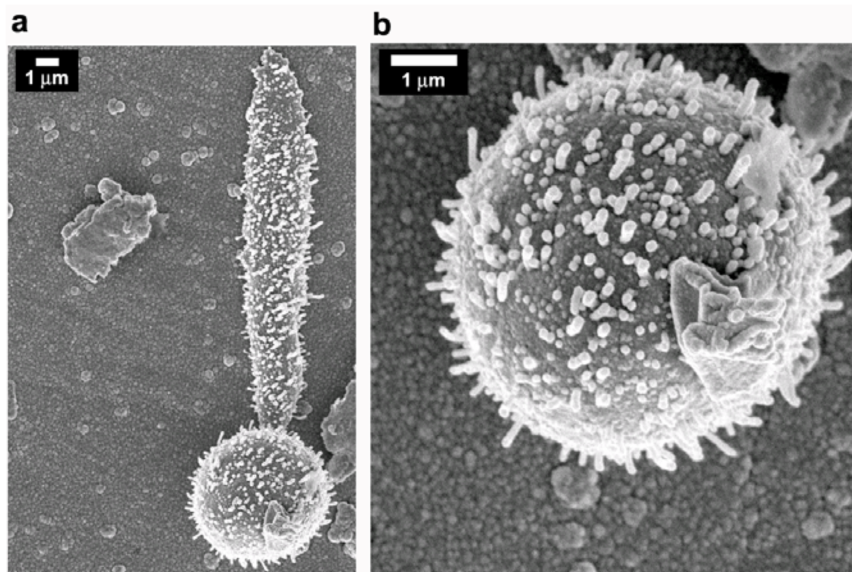

Figure 6.5 Nanowire growth during the codeposition process shown in Fig. 6.4. Image (b) is a magnified shot of the sphere in image (a).

In addition to experiments based on the HPPD system, there are unique technological capabilities in the High Temperature and Plasma Lab at the University of Minnesota that could be applied to the deposition of novel ceramic nanocomposites. One of these is a dual plasma codeposition system developed in the Kortshagen group that is used to deposit mixed-phase thin films [187]. While it is currently being used to deposit nc-Si embedded in a-Si for solar applications, this could easily be retrofitted to support other material combinations, such as ZnO nanoparticles embedded in a nc-Si matrix. However, this is a non-thermal plasma system, which would make the possibility of synthesizing ceramics such as SiC or Al_2O_3 unlikely due to the low temperatures. Another system of interest is the photoinduced CVD coating of nanoparticles developed in the Girshick group [188]. Recent work with SiO_2 coated Ag nanoparticles has shown the ability to control coating thickness and the prevention of Ag particle agglomeration

due to the SiO_2 coating. This technique could be used to study the compressive stress effects on core-shell nanoparticles. Coated particles from this type of system could also be incorporated into a film generated by secondary source, with the coating acting as a possible diffusion barrier between the particle and film during film growth.

References

1. P.J. Blau, website: http://www.ms.ornl.gov/researchgroups/SPM/methods/Tribology/Tribology.htm accessed 1/10/2010.

2. A. Matthews, K. Holmberg, Coatings Tribology: Properties, Mechanisms, Techniques, and Applications in Surface Engineering, Elsevier, Amsterdam, 2009.

3. B. Bhushan, B.K. Gupta, Handbook of Tribology - Materials, Coatings, and Surface Treatments, McGraw Hill, New York, 1991.

4. M. Bruno, S. Bugliosi, R. Chiara, J. Eng. Mater. Technol. 110 (1988) 274.

5. V.V. Lyubimov, A.A. Voevodin, A.L. Yerokhin, Y.S. Timofeev, I.K. Arkhipov, Surf. Coat. Technol. 52 (1992) 145.

6. K.J. Bozic, S.M. Kurtz, E. Lau, K. Ong, T.P. Vail, D.J. Berry, J. Bone Joint Surg.-Am. Vol. 91A (2009) 128.

7. M.H. Huo, N.F. Gilbert, J. Bone Joint Surg.-Am. Vol. 87A (2005) 2133.

8. M.H. Huo, N.F. Gilbert, J. Parvizi, J. Bone Joint Surg.-Am. Vol. 89A (2007) 1874.

9. D. Hannouche, C. Nich, P. Bizot, A. Meunier, R.M. Nizard, L. Sedel, Clin. Orthop. Rel. Res. (2003) 19.

10. G. Willmann, Clin. Orthop. Rel. Res. (2000) 22.

11. M.N. Rahaman, A. Yao, B.S. Bal, J.P. Garino, M.D. Ries, J. Am. Ceram. Soc. 90 (2007) 1965.

12. R.D. Crowninshield, A.G. Rosenberg, S.M. Sporer, Clin. Orthop. Rel. Res. 443 (2006) 266.

13. K.H. Zum Gahr, Microstructure and Wear of Materials, Elsevier, Amsterdam, 1987.

14. E. Hornbogen, International Conference on Wear of Materials, American Society of Mechanical Engineers, 1977, p. 477.

15. T.Y. Tsui, G.M. Pharr, W.C. Oliver, C.S. Bhatia, R.L. White, S. Anders, A. Anders, I.G. Brown, Materials Research Society, Pittsburgh, PA, USA, San Francisco, CA, USA, 1995, p. 447.

16. A. Leyland, A. Matthews, Wear 246 (2000) 1.

17. A.G. Evans, T.R. Wilshaw, Acta Metall. 24 (1976) 939.

18. J. Musil, M. Jirout, Surf. Coat. Technol. 201 (2007) 5148.

19. S. Veprek, A.S. Argon, J. Vac. Sci. Technol., B 20 (2002) 650.

20. J. Musil, Surf. Coat. Technol. 125 (2000) 322.

21. P.H. Mayrhofer, C. Mitterer, L. Hultman, H. Clemens, Prog. Mater Sci. 51 (2006) 1032.

22. S. Veprek, P. Nesladek, A. Niederhofer, F. Glatz, M. Jilek, M. Sima, Surf. Coat. Technol. 108-109 (1998) 138.

23. A.A. Voevodin, J.S. Zabinski, J. Mater. Sci. 33 (1998) 319.

24. A.G. Evans, J. Am. Ceram. Soc. 73 (1990) 187.

25. B.R. Lawn, N.P. Padture, H. Cait, F. Guiberteau, Science 263 (1994) 1114.

26. B.R. Lawn, Fracture of brittle solids, Cambridge University Press, New York, 1993.

27. P.F. Becher, J. Am. Ceram. Soc. 74 (1991) 255.

28. D.J. Green, R.H.J. Hannink, M.V. Swain, Transformation toughening of ceramics, CRC Press, Boca Raton, 1989.

29. R.H.J. Hannink, P.M. Kelly, B.C. Muddle, J. Am. Ceram. Soc. 83 (2000) 461.

30. G.-D. Zhan, J.D. Kuntz, J. Wan, A.K. Mukherjee, Nat. Mater. 2 (2003) 38.

31. K. Niihara, J. Ceram. Soc. Jpn. 99 (1991) 974.

32. M.D. Drory, J.W. Ager, T. Suski, I. Grzegory, S. Porowski, Appl. Phys. Lett. 69 (1996) 4044.

33. M.D. Uchic, D.M. Dimiduk, J.N. Florando, W.D. Nix, Science 305 (2004) 986.

34. H. Bei, S. Shim, G.M. Pharr, E.P. George, Acta Mater. 56 (2008) 4762.

35. J.R. Greer, W.C. Oliver, W.D. Nix, Acta Mater. 53 (2005) 1821.

36. D. Kiener, C. Motz, G. Dehm, Mater. Sci. Eng., A 505 (2009) 79.

37. M.D. Uchic, P.A. Shade, D.M. Dimiduk, Ann. Rev. Mater. Res. 39 (2009) 361.

38. D. Kiener, C. Motz, G. Dehm, R. Pippan, Int. J. Mater. Res. 100 (2009) 1074.

39. M. Legras, D.S. Gianola, C. Motz, MRS Bull. 35 354.

40. B. Moser, K. Wasmer, L. Barbieri, J. Michler, J. Mater. Res. 22 (2007) 1004.

41. F. Östlund, K. Rzepiejewska-Malyska, K. Leifer, L.M. Hale, Y. Tang, R. Ballarini, W.W. Gerberich, J. Michler, Adv. Funct. Mater. 19 (2009) 2439.

42. K. Wasmer, T. Wermelinger, A. Bidiville, R. Spolenak, J. Michler, J. Mater. Res. 23 (2008) 3040.

43. W.W. Gerberich, J. Michler, W.M. Mook, R. Ghisleni, F. Östlund, D.D. Stauffer, R. Ballarini, J. Mater. Res. 24 (2009) 898.

44. W.W. Gerberich, W.M. Mook, C.R. Perrey, C.B. Carter, M.I. Baskes, R. Mukherjee, A. Gidwani, J. Heberlein, P.H. McMurry, S.L. Girshick, J. Mech. Phys. Solids 51 (2003) 979.

45. W.M. Mook, J.D. Nowak, C.R. Perrey, C.B. Carter, R. Mukherjee, S.L. Girshick, P.H. McMurry, W.W. Gerberich, Phys. Rev. B 75 (2007) 214112.

46. A. Dubach, R. Raghavan, J.F. Loffler, J. Michler, U. Ramamurty, Scripta Mater. 60 (2009) 567.

47. D.C. Jang, J.R. Greer, Nat. Mater. 9 (2010) 215.

48. C.Q. Chen, Y.T. Pei, J.T.M. De Hosson, Philos. Mag. Lett. 89 (2009) 633.

49. S. Nakao, T. Ando, M. Shikida, K. Sato, J. Micromech. Microeng. 18 (2008).

50. T. Namazu, Y. Isono, T. Tanaka, J Microelectromech S 9 (2000) 450.

51. X. Han, K. Zheng, Y. Zhang, X. Zhang, Z. Zhang, Z.L. Wang, Adv. Mater. 19 (2007) 2112.

52. D. Kiener, C. Motz, M. Rester, M. Jenko, G. Dehm, Mater. Sci. Eng., A 459 (2007) 262.

53. V. Sivakov, G. Andrä, U. Gösele, S. Christiansen, physica status solidi (a) 203 (2006) 3692.

54. Y. Zhu, F. Xu, Q. Qin, W.Y. Fung, W. Lu, Nano Lett. 9 (2009) 3934.

55. M. Werner, E.R. Weber, M. Bartsch, U. Messerschmidt, Physica Status Solidi (a) 150 (1995) 337.

56. G. Stan, S. Krylyuk, A.V. Davydov, R.F. Cook, Nano Lett. 10 (2010) 2031.

57. K. Kang, W. Cai, Philos. Mag. A 87 (2007) 2169

58. N.P. Rao, H.J. Lee, M. Kelkar, D.J. Hansen, J.V.R. Heberlein, P.H. McMurry, S.L. Girshick, Nanostruct. Mater. 9 (1997) 129.

59. N. Rao, S. Girshick, P. McMurry, J. Heberlein Patent No. 5,874,134, 1999.

60. J. Hafiz, Mechanical Engineering, University of Minnesota, Minneapolis, MN, 2006.

61. Q. Wei, Mechanical Engineering, University of Minnesota, Minneapolis, MN, 1994.

62. M. Hatch, Mechanical Engineering, University of Minnesota, Minneapolis, MN, 1993.

63. N. Rao, B. Micheel, D. Hansen, C. Fandrey, M. Bench, S. Girshick, J. Heberlein, P. McMurry, J. Mater. Res. 10 (1995) 2073.

64. N. Rao, S. Girshick, J. Heberlein, P. McMurry, S. Jones, D. Hansen, B. Micheel, Plasma Chem. Plasma Process. 15 (1995) 581.

65. N.P. Rao, N. Tymiak, J. Blum, A. Neuman, H.J. Lee, S.L. Girshick, P.H. McMurry, J. Heberlein, J. Aerosol Sci 29 (1998) 707.

66. A. Gidwani, Mechanical Engineering, University of Minnesota, Minneapolis, MN, 2003.

67. A. Neuman, Mechanical Engineering, University of Minnesota, Minneapolis, MN, 2000.

68. A.R. Beaber, L.J. Qi, J. Hafiz, P.H. McMurry, J.V.R. Heberlein, W.W. Gerberich, S.L. Girshick, Surf. Coat. Technol. 202 (2007) 871.

69. J. Hafiz, R. Mukherjee, X. Wang, J.V.R. Heberlein, P.H. McMurry, S.L. Girshick, Thin Solid Films 515 (2006) 1147.

70. X. Wang, J. Hafiz, R. Mukherjee, T. Renault, J. Heberlein, S.L. Girshick, P.H. McMurry, Plasma Chem. Plasma Process. 25 (2005) 439.

71. J. Hafiz, R. Mukherjee, X. Wang, M. Cullinan, J.V.R. Heberlein, P.H. McMurry, S.L. Girshick, J. Nanopart. Res. 8 (2006) 995.

72. J. Hafiz, R. Mukherjee, X. Wang, P.H. McMurry, J.V.R. Heberlein, S.L. Girshick, J. Therm. Spray Technol. 15 (2006) 822.

73. H.S. Kim, D.J. Choi, J. Am. Ceram. Soc. 82 (1999) 331.

74. H. Hertz, J. Reine Angew. Math. 92 (1881) 15.

75. I.N. Sneddon, International Journal of Engineering Science 3 (1965) 47.

76. M.F. Doerner, W.D. Nix, J. Mater. Res. 1 (1986) 601.

77. W.C. Oliver, G.M. Pharr, J. Mater. Res. 7 (1992) 1564.

78. J. Thurn, R.F. Cook, J. Mater. Res. 17 (2002) 1143.

79. X. Wang, Mechanical Engineering, University of Minnesota, Minneapolis, MN, 2006.

80. HysitronInc., TriboIndenter Users Manual, Minneapolis, MN, 2001.

81. W.C. Oliver, J.B. Pethica, U.S. Patent No. 4,848,141, 1989.

82. S. Ruffell, J.E. Bradby, J.S. Williams, P. Munroe, J. Appl. Phys. 102 (2007) 8.

83. J.E. Bradby, J.S. Williams, M.V. Swain, Phys. Rev. B 67 (2003) 9.

84. M.J. Pelletier (Ed.), Analytical applications of Raman Spectroscopy, Blackwell Science, Ann Arbor, MI, 1999.

85. E. Anastassakis, A. Pinczuk, E. Burstein, F.H. Pollak, M. Cardona, Solid State Commun. 8 (1970) 133.

86. W. Trzeciakowski, J. Strzeszewski, G. Wojciech, J.-M. Thebaud, physica status solidi (b) 245 (2008) 28.

87. S. Timoshenko, Strength of materials: Part II, Advanced Theory and Problems, D. Van Nostrand, Princeton, NJ, 1930.

88. W.A. Brantley, J. Appl. Phys. 44 (1973) 534.

89. I. De Wolf, Semicond. Sci. Technol. 11 (1996) 139.

90. S. Piscanec, M. Cantoro, A.C. Ferrari, J.A. Zapien, Y. Lifshitz, S.T. Lee, S. Hofmann, J. Robertson, Phys. Rev. B 68 (2003) 241312.

91. K.W. Adu, H.R. Gutiérrez, U.J. Kim, P.C. Eklund, Phys. Rev. B 73 (2006) 155333.

92. A. Kailer, Y.G. Gogotsi, K.G. Nickel, J. Appl. Phys. 81 (1997) 3057.

93. V. Domnich, Y. Gogotsi, S. Dub, Appl. Phys. Lett. 76 (2000) 2214.

94. A. Fontcuberta i Morral, J. Arbiol, J.D. Prades, A. Cirera, J.R. Morante, Adv. Mater. 19 (2007) 1347.

95. J.D. Prades, J. Arbiol, A. Cirera, J.R. Morante, A. Fontcuberta i Morral, Appl. Phys. Lett. 91 (2007) 123107.

96. A.R. Beaber, J. Hafiz, J.V.R. Heberlein, W.W. Gerberich, S.L. Girshick, Surf. Coat. Technol. 203 (2008) 771.

97. A.R. Beaber, Z.B. Gay, W.W. Gerberich, S.L. Girshick, in: A. von Keudell, J. Winter, M. Böke, V. Schulz-von der Gathen (Eds.), ISPC 19, Bochum, Germany, 2009.

98. C.B. Carter, M.G. Norton, Ceramic Materials: Science and Engineering, Springer Science, New York, 2007.

99. O. Madelung, Semiconductors: Data Handbook, Springer, Berlin, 2004.

100. B. Cockeram, Metall. Mater. Trans. A 33 (2002) 3685.

101. ASM Handbooks, ASM International, Materials Park, OH, 1991.

102. I. Sabirov, R.Z. Valiev, I.P. Semenova, R. Pippan, Metall. Mater. Trans. A 41 (2010) 727.

103. C. Maerky, M.O. Guillou, J.L. Henshall, R.M. Hooper, Mater. Sci. Eng., A 209 (1996) 329.

104. O. Zywitzki, T. Modes, H. Sahm, P. Frach, K. Goedicke, D. Glöß, Surf. Coat. Technol. 180-181 (2004) 538.

105. C.R. Perrey, C.B. Carter, J. Mater. Sci. 41 (2006) 2711.

106. T. Chudoba, P. Schwaller, R. Rabe, J.M. Breguet, J. Michler, Philos. Mag. A 86 (2006) 5265.

107. L.S. Sigl, P.A. Mataga, B.J. Dalgleish, R.M. McMeeking, A.G. Evans, Acta Metall. 36 (1988) 945.

108. L.S. Sigl, H.E. Exner, Metall. Mater. Trans. A 18 A (1987) 1299.

109. J.A. Thornton, D.W. Hoffman, Thin Solid Films 171 (1989) 5.

110. H. Ming Yuan, A.G. Evans, J.W. Hutchinson, International Journal of Solids and Structures 31 (1994) 3443.

111. K.L. Johnson, Contact Mechanics, Cambridge University Press, Cambridge, 1985.

112. P.H.M. C. Mitterer, M. Beschliesser, P. Losbichler, P. Warbichler, F. Hofer, P.N. Gibson, W. Gissler, H. Hruby´, J. Musil, J. Vloek, ICMCTF'99, San Diego, CA, 1999.

113. B. Bhushan, G. Wei, J. Am. Ceram. Soc. 89 (2006) 2542.

114. D. Tabor, The Hardness of Metals, Oxford Clarendon Press, New York, 1951.

115. B.R. Lawn, A.G. Evans, D.B. Marshall, J. Am. Ceram. Soc. 63 (1980) 574.

116. G.M. Pharr, Mater. Sci. Eng., A A253 (1998) 151.

117. A.E. Martinelli, R.A.L. Drew, R. Berriche, J. Mater. Sci. Lett. 15 (1996) 307.

118. H.J. Frost, M.F. Ashby, Deformation-mechanism maps: The Plasticity and Creep of Metals and Ceramics, Pergamon Press, Oxford, 1982.

119. Perspectives in Creep Fracture, Pergamon Press, Oxford, 1983.

120. Y. Tree, A. Venkateswaran, D.P.H. Hasselman, J. Mater. Sci. 18 (1983) 2135.

121. D.P.H. Hasselman, J. Am. Ceram. Soc. 52 (1969) 600.

122. D.J. Green, R. Tandon, V.M. Sglavo, Science 283 (1999) 1295.

123. M. Ferrari, L. Lutterotti, J. Eng. Mech-ASCE 118 (1992) 1928.

124. R.S. Wagner, T. Am. I. Min. Met. Eng. 233 (1965) 1053.

125. W. Gerlach, B. Goel, Solid-State Electronics 10 (1967) 589.

126. S. Krylyuk, A.V. Davydov, I. Levin, A. Motayed, M.D. Vaudin, Appl. Phys. Lett. 94 (2009) 3.

127. J.E. Allen, E.R. Hemesath, D.E. Perea, J.L. Lensch-Falk, LiZ.Y, F. Yin, M.H. Gass, P. Wang, A.L. Bleloch, R.E. Palmer, L.J. Lauhon, Nat Nano 3 (2008) 168.

128. J.B. Hannon, S. Kodambaka, F.M. Ross, R.M. Tromp, Nature 440 (2006) 69.

129. V.A. Sivakov, R. Scholz, F. Syrowatka, F. Falk, U. Gosele, S.H. Christiansen, Nanotechnology (2009) 405607.

130. N.A. Stolwijk, B. Schuster, J. Hölzl, H. Mehrer, W. Frank, Physica B+C 116 (1983) 335.

131. S.H. Oh, M. Legros, D. Kiener, G. Dehm, Nat. Mater. 8 (2009) 95.

132. W. Lerch, N.A. Stolwijk, J. Appl. Phys. 83 (1998) 1312.

133. F.D. Murnaghan, Proc. Natl. Acad. Sci. USA 30 (1944) 244.

134. R. Pandey, M. Causa, N.M. Harrison, M. Seel, J. Phys.: Condens. Matter 8 (1996) 3993.

135. Y.B. Gerbig, S.J. Stranick, D.J. Morris, M.D. Vaudin, R.F. Cook, J. Mater. Res. 24 (2009) 1172.

136. G.M. Pharr, W.C. Oliver, D.S. Harding, J. Mater. Res. 6 (1991) 1129.

137. J.Z. Hu, L.D. Merkle, C.S. Menoni, I.L. Spain, Phys. Rev. B 34 (1986) 4679.

138. S.H. Tolbert, A.B. Herhold, L.E. Brus, A.P. Alivisatos, Phys. Rev. Lett. 76 (1996) 4384.

139. H. Saka, A. Shimatani, M. Suganuma, Suprijadi, Philos. Mag. A 82 (2002) 1971.

140. A.M. Minor, E.T. Lilleodden, M. Jin, E.A. Stach, D.C. Chrzan, J.W. Morris, Philos. Mag. A 85 (2005) 323.

141. A.B. Mann, D. van Heerden, J.B. Pethica, T.P. Weihs, J. Mater. Res. 15 (2000) 1754.

142. P. Valentini, W.W. Gerberich, T. Dumitrica, Phys. Rev. Lett. (2007).

143. D.E. Kim, S.I. Oh, Nanotechnology 17 (2006) 2259.

144. M.C. Gupta, A.L. Ruoff, J. Appl. Phys. 51 (1980) 1072.

145. D.L. Callahan, J.C. Morris, J. Mater. Res. 7 (1992) 1614.

146. D. Ge, A.M. Minor, E.A. Stach, J.W. Morris, Philos. Mag. A 86 (2006) 4069.

147. B.R. Lawn, D.B. Marshall, P. Chantikul, J. Mater. Sci. 16 (1981) 1769.

148. L.E. Brus, J.A.W. Harkless, F.H. Stillinger, J. Am. Chem. Soc. 118 (1996) 4834.

149. G.R. Anstis, P. Chantikul, B.R. Lawn, D.B. Marshall, J. Am. Ceram. Soc. 64 (1981) 533.

150. S. Veprek, F.A. Sarott, Z. Iqbal, Phys. Rev. B 36 (1987) 3344.

151. C.C. Yang, S. Li, J. Phys. Chem. B 112 (2008) 14193.

152. G. Weill, J.L. Mansot, G. Sagon, C. Carlone, J.M. Besson, UK, 1989, p. 280.

153. P. Pirouz, R. Chaim, U. Dahmen, K.H. Westmacott, Acta. Metall. Mater. 38 (1990) 313.

154. A.H. Chokshi, T.G. Langdon, Mater. Sci. Technol. 7 (1991) 577.

155. B. Reppich, P. Haasen, B. Ilschner, Acta Metall. 12 (1964) 1283.

156. P. Haasen, H. Alexander, Solid State Phys. 22 (1968) 27.

157. J. Weertman, J. Appl. Phys. 28 (1957) 1185.

158. H. Siethoff, P. Haasen, in: R.R. Hasiguti (Ed.), Lattice defects in semiconductors, University of Tokyo Press, Tokyo, 1968.

159. M.G. Mil'vidskii, V.B. Osvenskii, O.G. Stolyarov, Neorg. Mater. 2 (1966) 585.

160. S.S. Iyer, K. Eberl, M.S. Goorsky, F.K. Legoues, J.C. Tsang, F. Cardone, Appl. Phys. Lett. 60 (1992) 356.

161. J.C. Tsang, K. Eberl, S. Zollner, S.S. Iyer, Appl. Phys. Lett. 61 (1992) 961.

162. M. Meléndez-Lira, J. Menéndez, W. Windl, O.F. Sankey, G.S. Spencer, S. Sego, R.B. Culbertson, A.E. Bair, T.L. Alford, Phys. Rev. B 54 (1996) 12866.

163. M. MelendezLira, J. Menendez, K.M. Kramer, M.O. Thompson, N. Cave, R. Liu, J.W. Christiansen, N.D. Theodore, J.J. Candelaria, J. Appl. Phys. 82 (1997) 4246.

164. P. Angelini, W. Mader, P.F. Becher, Mater. Res. Soc. Symp. P. 78 (1987) 241.

165. J.D. Nowak, A.R. Beaber, O. Ugurlu, S.L. Girshick, W.W. Gerberich, Scripta Mater. 62 (2010) 819.

166. A.R. Beaber, J.D. Nowak, O. Ugurlu, W.M. Mook, S.L. Girshick, R. Ballarini, W.W. Gerberich, Philos. Mag. A (in press).

167. R. Cook, J. Mater. Sci. 41 (2006) 841.

168. W.W. Gerberich, W.M. Mook, M.J. Cordill, C.B. Carter, C.R. Perrey, J.V.R. Heberlein, S.L. Girshick, Int. J. Plast. 21 (2005) 2391.

169. W.W. Gerberich, S.K. Venkataraman, H. Huang, S.E. Harvey, D.L. Kohlstedt, Acta. Metall. Mater. 43 (1995) 1569.

170. J.D. Eshelby, F.C. Frank, H.H. Wills, F.R.N. Nabarro, Philos. Mag. A 42 (1951) 351.

171. W.W. Gerberich, W.M. Mook, C.B. Carter, R. Ballarini, Int. J. Fracture 148 (2007) 109.

172. R.G. Budynas, Advanced strength and applied stress analysis, McGraw-Hill, Boston, 1997.

173. T.F. Page, W.C. Oliver, C.J. McHargue, J. Mater. Res. 7 (1992) 450.

174. D.B. Williams, C.B. Carter, Transmission electron microscopy: A textbook for materials science, Springer Science, New York, 1996.

175. J. Deneen, W. Mook, A. Minor, W. Gerberich, C. Barry Carter, J. Mater. Sci. 41 (2006) 4477.

176. J.D. Nowak, W.M. Mook, A.M. Minor, W.W. Gerberich, C.B. Carter, Philos. Mag. A 87 (2007) 29.

177. H. Huang, W.W. Gerberich, Acta Metall. Mater. 40 (1992) 2873.

178. J. Weertman, J.R. Weertman, Elementary dislocation theory, Oxford University Press, New York, 1992.

179. D. Broek, Elementary Engineering Fracture Mechanics, Kluwer Academic, London, 1991.

180. W.M. Mook, Chemical Engineering and Material Science, University of Minnesota, Minneapolis, MN, 2008.

181. M. Imai, K. Yaoita, Y. Katayama, J.-Q. Chen, K. Tsuji, J. Non-Cryst. Solids 150 (1992) 49.

182. J.S. Field, M.V. Swain, J. Mater. Res. 8 (1993) 297.

183. T.F. Page, L. Riester, S.V. Hainsworth, MRS, Warrendale, PA, USA, San Francisco, CA, USA, 1998, p. 113.

184. J.J. Gilman, Philos. Mag. B 67 (1993) 207.

185. J. Godet, et al., J. Phys.: Condens. Matter 15 (2003) 6943.

186. M. Bechelany, X. Maeder, J. Riesterer, J. Hankache, D. Lerose, S. Christiansen, J. Michler, L. Philippe, Crystal Growth & Design 10 (2010) 587.

187. Y. Adjallah, C. Anderson, U. Kortshagen, J. Kakalios, J. Appl. Phys. 107 (2010) 10.

188. A.M. Boies, J.T. Roberts, S.L. Girshick, B. Zhang, T. Nakamura, A. Mochizuki, Nanotechnology 20 (2009) 8.